MECHANIK

FORSCHUNGSBERICHT

Avoidance of brake squeal by a separation of the brake disc's eigenfrequencies: A structural optimization problem

Andreas Wagner

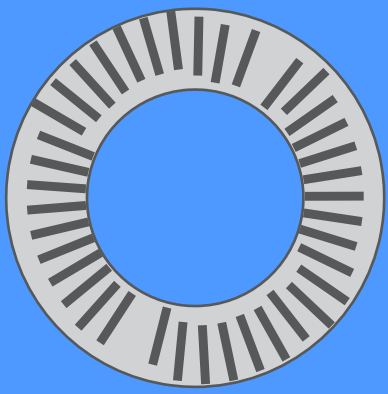

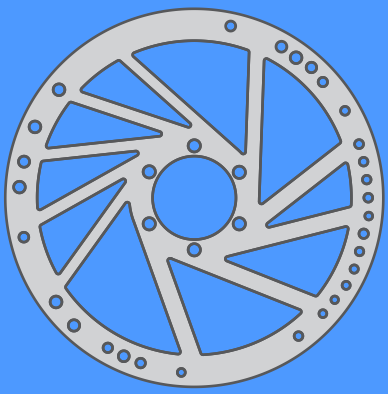

$$\max_{p_n} \min_{k} |f_{k+1} - f_k|$$

TECHNISCHE UNIVERSITÄT DARMSTADT

Band 31

Avoidance of brake squeal by a separation of the brake disc's eigenfrequencies: A structural optimization problem

Vom Fachbereich Maschinenbau
an der Technischen Universität Darmstadt
zur
Erlangung des Grades eines Doktor-Ingenieurs (Dr.-Ing.)
genehmigte

Dissertation

vorgelegt von

Dipl.-Ing. Andreas Wagner

aus Lichtenfels

Berichterstatter:	Prof. Dr. Peter Hagedorn
1. Mitberichterstatter:	Prof. Dr.-Ing. Wilfried Becker
2. Mitberichterstatter:	Prof. Dr.-Ing. Bernhard Schweizer
Tag der Einreichung:	15. August 2013
Tag der mündlichen Prüfung:	16. Oktober 2013

Darmstadt 2013

D 17

Wagner, Andreas

Avoidance of brake squeal by a separation of the brake disc's eigenfrequencies: A structural optimization problem

Forschungsberichte des Instituts für Mechanik der Technischen Universität Darmstadt
Band 31

Herausgeber:

Studienbereich Mechanik
Technische Universität Darmstadt
Hochschulstr. 1
D-64289 Darmstadt
Germany

ISBN 978-3-935868-31-0

Vorwort

Die vorliegende Arbeit beschäftigt sich mit der Vermeidung von Bremsenquietschen durch eine gezielt in die Bremsscheibe eingebrachte Asymmetrie. Sie entstand während meiner Tätigkeit als wissenschaftlicher Mitarbeiter in der Arbeitsgruppe Dynamik und Schwingungen an der TU Darmstadt, die von Herrn Prof. Peter Hagedorn geleitet wird. Diese war vom Beginn meiner Promotionszeit an bis Juli 2012 am Fachgebiet Systemzuverlässigkeit und Maschinenakustik von Herrn Prof. Holger Hanselka im Fachbereich Maschinenbau angesiedelt und seitdem am Fachgebiet Numerische Berechnungsverfahren im Maschinenbau von Herrn Prof. Michael Schäfer.

Ich möchte an dieser Stelle all denjenigen herzlich danken, die zum Gelingen dieser Arbeit beigetragen haben. Allen voran gebührt mein besonderer Dank meinem Doktorvater, Herrn Prof. Peter Hagedorn, der mich in meiner mehrjährigen Tätigkeit stets unterstützt und gefördert hat und von dem ich sehr viel lernen konnte. Ich danke ihm auch dafür, dass er mich immer wieder ermuntert hat, über meinen Tellerrand zu blicken und meinen Horizont u.a. durch Auslandsaufenthalte zu erweitern. Ich möchte mich auch bei den Herren Prof. Wilfried Becker und Prof. Bernhard Schweizer für die bereitwillige und wohlwollende Übernahme der Koreferate sowie für ihre vielen Anregungen bedanken.

Mein Dank gilt auch der Adam Opel AG, die dieses Projekt finanziell unterstützt hat. Ich bin Herrn Martin Schönecker sehr verbunden, der während der gesamten Projektlaufzeit als wertvoller Ansprechpartner zur Verfügung stand. Weiterhin danke ich den Herren Prof. Lothar Harzheim, Markus Bauer, Michael Kochem, Thorsten Kreich, Christian Lankes, Ralph Stenger, Janko Wuchatsch und Alexander Zopp für die Unterstützung und Herrn Dietmar Jennewein, der dieses Projekt in seiner Zeit bei Opel angestoßen hat.

Meinem ehemaligen Kollegen Gottfried Spelsberg-Korspeter, von dem ich viel gelernt und mit dem ich sehr gerne zusammen gearbeitet habe, möchte ich herzlich danken. Von ihm stammen auch wichtige theoretische Arbeiten, die eine wesentliche Grundlage für die vorliegende Dissertation bilden. Auch bin ich ihm für viele interessante Diskussionen und Anregungen dankbar.

Auch meinen derzeitigen und ehemaligen Kollegen danke ich sehr für eine wirklich schöne Zeit und ihre große Hilfsbereitschaft. Mein Dank gilt Andres Arrieta-Diaz, Manuel Eckstein, Eduard Heffel, Matthias Heymanns, Henning Spiegelberg und Steffen Wiendl. Ich möchte mich auch bei Maria Rauck und Renate Schreiber bedanken, die mir mit Rat und Tat zur Seite gestanden haben. Für seine Unterstützung bin ich auch Tim Klaus sehr dankbar.

Ich bin Herrn Prof. Ilanko von der University of Waikato in Hamilton, Neuseeland, sehr verbunden dafür, dass er mich für einen kurzen Forschungsaufenthalt an seinem Institut aufgenommen hat. Mein Dank gilt ihm auch für wertvolle Anregungen zum Thema Modellierung mit negativen Massen und Steifigkeiten.

Zum Gelingen der Arbeit haben auch Maximilian Jüngst, Satish Kumar Panda und Manuel Becher viel beigetragen, deren Bachelor- bzw. Masterarbeiten ich betreut habe. Vielen Dank dafür. Ich möchte auch denjenigen studentischen Mitarbeitern danken, die unter meiner Betreuung ein ADP oder Forschungsseminar bearbeitet oder als Hilfswissenschaftler für mich gearbeitet haben.

Mein besonderer Dank gilt auch meinen Eltern für ihre stetige Unterstützung. Ohne sie wäre diese Dissertation nicht möglich gewesen.

Darmstadt, im Dezember 2013 Andreas Wagner

Abstract

Brake squeal is a high-pitched noise in the frequency range between 1 kHz and 16 kHz originating from self-excited vibrations caused by the frictional contact between brake pads and brake disc. Since some decades, it has intensively been studied and many countermeasures have been proposed, including active and passive methods. It is known from experiments and has also been proved mathematically that splitting the eigenfrequencies of the brake rotor has a stabilizing effect and avoids brake squeal. In this thesis, this knowledge is used to derive design goals for asymmetric, squeal-free discs. It is necessary to split all eigenfrequencies of the brake disc in a pre-definable frequency band to guarantee stability, inhibit the onset of self-excited vibrations and thus avoid squeal completely. In order to achieve this goal, a structural optimization of automotive as well as bicycle brake discs is conducted. Using a novel, efficient modeling technique, large changes in the geometry can be covered leading to a successful optimization in all cases studied. Optimized automotive and bicycle brake discs have been manufactured and tested on appropriate brake test rigs to assess their squeal affinity, and it is shown that the optimized discs have a greatly improved squeal behavior. This validates the mathematical theory behind the presented approach and demonstrates that splitting eigenfrequencies of the brake rotor is a passive, low-cost and effective squeal countermeasure applicable to a variety of brake systems.

Kurzfassung

Bremsenquietschen stellt ein hochfrequentes Geräusch im Frequenzbereich von etwa 1 kHz bis 16 kHz dar. Es entsteht durch selbsterregte Schwingungen, die durch den Reibkontakt zwischen Bremsbelägen und Bremsscheibe ausgelöst werden. Seit einigen Jahrzehnten wird dieses Phänomen intensiv untersucht und es wurden viele passive und aktive Maßnahmen vorgeschlagen, es zu mindern. Aus Experimenten ist bekannt, dass das Aufspalten der Eigenfrequenzen des Bremsenrotors einen stabilisierenden Effekt hat und sich damit Bremsenquietschen vermeiden lässt. Vor kurzem erfolgte auch der mathematische Nachweis. Diese Vorkenntnisse werden in der vorliegenden Dissertation dazu genutzt, Ziele für die Gestaltung asymmetrischer, quietschfreier Bremsscheiben abzuleiten. Es ist notwendig, alle Eigenfrequenzen der Bremsscheibe in einem vorher abschätzbaren Frequenzbereich zu spalten, um Stabilität sicherzustellen. Damit können selbsterregte Schwingungen verhindert und Quietschen unterbunden werden. Dies führt auf eine Strukturoptimierung von Automobil- und Fahrradbremsscheiben. Die Verwendung einer neuen, effizienten Modellierungstechnik erlaubt es, große Geometrieänderungen zu berücksichtigen, um die Optimierung bei allen untersuchten Fällen erfolgreich abzuschließen. Die optimierten Automobil- und Fahrradbremsscheiben wurden gefertigt, auf geeigneten Bremsenprüfständen getestet und ihre Quietschneigung untersucht. Dabei zeigt sich, dass die Optimierung das Quietschverhalten stark verbessert hat. Dadurch wird die Praktikabilität des vorgestellten Ansatzes belegt. Zudem weisen diese Tests nach, dass das Aufspalten der Eigenfrequenzen des Bremsrotors eine passive, kostengünstige und effektive Maßnahme gegen Quietschen darstellt, die sich auf eine Vielzahl von Bremssystemen übertragen lässt.

Contents

1 Introduction

The technical progress in the automotive, transport and aircraft industry over the last decades, increasing safety standards and customer demands have led to the development of sophisticated, high-performing and comfortable brake systems. Despite this rapid progress, some problems of brake systems remain or have even been increased due to the requirement for lightweight and cost-effective construction. One of those is brake squeal, which is a noise phenomenon studied at least since the 1930s, as KINKAID et al. report [60]. There is no precise definition of brake squeal available in the literature, still, most authors agree that squeal is a high-pitched, friction-induced sound with frequencies ranging from 1 kHz to approximately 16 kHz for brakes used in the automotive and motorcycle industry [2, 21, 60, 92] and 100 Hz to 1000 Hz for aircraft brakes [2]. The frequently made distinction between low frequency squeal and high frequency squeal [26], however, is not adopted in this thesis. It is characteristic for most squeal events that the generated noise is dominated by one distinct frequency independent of the rotational speed. Furthermore, brake squeal is indicated by amplitudes of the vibrations of the brake disc in the micrometer range and the created sound pressure level (SPL) can reach over 100 dB [60, 92]. In most cases, brake squeal is a pure comfort problem leading to passenger complaints and high warranty cost reaching over 100 Million Dollar each year regarding the automotive industry in particular [27]. It does not affect the main function of friction brakes to reduce vehicle speed by a conversion of kinetic to thermal energy. Squeal can also be highly safety relevant if squealing brake systems are connected to lightweight rims used especially for high-performance motorcycles and bicycles, since the friction induced vibrations can lead to fatigue and material failure of spokes [44, 79].

Brake squeal can occur for all types of friction-based brake systems, for disc brakes used in the aircraft, automotive, transport and motorcycle industry,

drum brakes used in the automotive and motorcycle industry as well as for block brakes of trains. In this work, the focus will lie on disc brakes, of which the general set-up is shown in Fig. 1.1. There are different types of

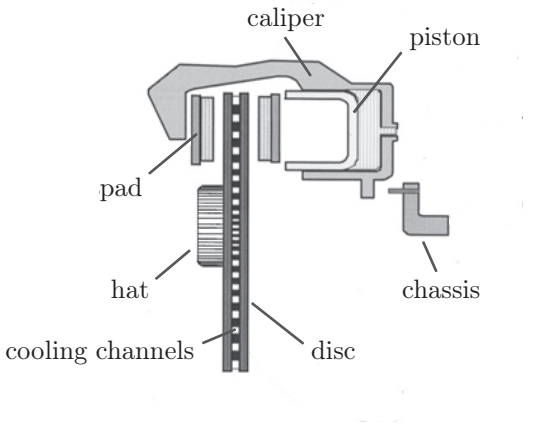

Figure 1.1: Disc brake assembly. Picture adopted in a modified form from [2].

disc brakes, still, they share the basic working principle: With an application of brake pressure to the brake piston, the brake pads enter into frictional contact with the brake disc rotating at an angular velocity determined by the vehicle speed. The brake disc is mounted to the axle of the vehicle by a hat-like structure, while the caliper is fixed to the chassis. The frictional contact leads to a resulting braking torque decelerating the vehicle under generation of heat in the brake rotor. The hat of the brake disc is intended to inhibit the heat flow from the rotor to the axle, where it could damage bearings or other important components. In many automotive brake systems, cooling channels can be found between the two friction rings of the rotor, which are the plates in direct contact to the brake pads. The cooling channels defined by cooling ribs are indicated in the figure. Disc brakes for motorcycles and bicycles are similar systems, however, the shape and design of the rotor is quite different.

While friction is essential for the function of the brake, the frictional contact can lead to unwanted effects, of which one of the most annoying is brake squeal, amongst others like judder or chattering, which shall not be discussed

in this thesis. All researchers and engineers working in the field of brake squeal agree that the frictional contact between brake pads and disc is the origin of self-excited vibrations audible as squeal, still, the specific excitation mechanism is a matter of intense discussion.

1.1 Excitation mechanism of brake squeal

Self-excited vibrations caused by the frictional contact between bodies are a very broad field of research. A rather general overview can be gained from the works of Ibrahim [48,49] and Akay [2]. Specifically for brake squeal, there is a consensus among researchers that for the excitation of brake squeal a friction force is necessary, which leads to an instability of the brake system and self-excited vibrations [41]. Instead of the intended energy conversion from kinetic energy of the vehicle to thermal energy in the brake, a small portion of energy is misrouted to vibrations of the brake system, mainly out-of-plane vibrations of the brake rotor [60,83]. However, further explanations of the origin of brake squeal differ with respect to the characteristics of the friction force necessary for the excitation. There are researchers who argue that the friction force has to exhibit certain characteristics to lead to squeal. Others see the origin of brake squeal in the structure of the equations of motions leading to instability, even if the frictional force is determined by Coulomb's law of friction with a constant coefficient of friction.

The first publications on brake squeal are part of the first group and point to a velocity-dependent coefficient of friction as an excitation mechanism of brake squeal, as is reported by Kinkaid et al. [60]. If the friction coefficient decreases with decreasing rotational velocity, a linearization about the steady-sliding state can result in velocity-proportional terms that can be thought of being negative damping, leading to increasing amplitudes of vibration. Despite the fact that this explanation for squeal nowadays is not acknowledged as sole origin of brake squeal [15, 60], some researchers still include velocity-dependent friction coefficients in their models [9, 58, 91, 105]. As long as the dynamic coefficient of friction between pad and disc is smaller than the static one, it is possible that a stick-slip motion results, which some researchers also

see as a possible explanation of brake squeal [90, 100]. However, most other authors consider it highly unlikely that this is the case [41, 91, 122], since stick-slip effects require the possibility of vanishing relative velocity between brake pad and rotor, which is not possible for the parameters of a realistic brake disc. For other noise effects associated with brakes like "groan", stick-slip can be the reason, as is presented in [91]. SPURR introduced an extension of the stick-slip brake squeal explanation, termed "sprag-slip", in 1961 as is reported unisonously by PAPINNIEMI et al. [94], OUYANG et al. [88] and KINKAID et al. [60]. Also, the coefficient of friction is known to be pressure- and/or temperature-dependent, what is also related to the excitation of brake squeal in some publications [49, 77]. This already hints to the fact that the tribology between brake pad and disc is very complicated and therefore COULOMB's law of friction might not be the best modeling approach in the context of brake squeal. Thus, there are publications that include more complex tribological behavior in the modeling of brake squeal [32].

Nevertheless, most researchers attribute the excitation mechanism of brake squeal to the structure of the equations of motion, which exhibits unsymmetric parts in the displacement-proportional forces (non-potential circulatory forces). This can occur even with COULOMB's law of friction with a constant friction coefficient [6, 60, 119, 122]. Due to the friction in the contact area between brake pad and disc, the degrees of freedom (DOF) of the brake pad and the brake disc are constrained and coupled, represented in the equations of motion by the presence of a skew-symmetric circulatory matrix. These circulatory terms in the linearized equations of motion can lead to eigenvalues with positive real parts corresponding to an instability, as will be explained in detail in section 2.1. Due to the fact that at least two DOF are required in a model exhibiting this type of instability, and since in continuous models always two eigenmodes participate in the unstable vibration, it is often referred to as "mode lock-in" (or flutter) instability. This is a very common term in the literature concerning brake squeal and is therefore used in this thesis as well. Historically, the excitation mechanism of brake squeal has frequently been attributed to the friction forces in the contact zone between brake rotor and pad being follower forces [60, 133]. Follower forces are forces that keep their

orientation relative to the body on which they act even if this body deforms. Even publications from the younger past consider follower forces as a root cause of brake squeal [59, 89]. However, HERRMANN points to the fact that the term "follower force" is not used consistently in the literature and that it is often used interchangeably with "moving load" or "circulatory force" [39].

In this thesis the perspective is taken that the friction forces at the interface between brake pad and disc lead to circulatory terms in the equations of motion which give rise to self-excited vibrations audible as brake squeal. The friction forces do not necessarily have to resemble what is classically understood by a "follower force", as it occurs e.g. in the buckling of a column under a force always acting in the direction of its neutral line. This perspective is also taken by many other scientists [18, 42, 58, 73, 85, 112, 122] and is experimentally strongly encouraged [3, 26, 60, 74]. Furthermore it is the basis for the state-of-the-art analysis of brake squeal using modern finite element (FE) codes as it will be introduced in the following section and explained in detail in section 2.1.

1.2 Modeling and analysis of squealing brake systems

Together with a deeper understanding of the excitation mechanism of brake squeal that has evolved over the past decades, also the modeling and further analysis have been refined. The first models for brake squeal were discrete systems with few DOF and lumped parameters [48, 60, 92], mainly because computing capacity was highly limited. This changed during the past two or three decades, still, even nowadays, minimal models of brake squeal or models with only a very limited number of DOF have their merits. They continue to be important since they allow a deep analytical insight into the important parameters, the excitation mechanism [59, 100, 122] and permit the inclusion and analytical or semianalytical treatment of nonlinearities [18, 41, 111]. Also, they can provide a basis for an active suppression of brake squeal [40, 42, 45].

Nevertheless, the complex geometry of modern disc brake systems cannot

be represented or quantitative results be given by such models. The common procedure is thus to use the finite element method (FEM) to model brake disc, pads, caliper and even parts of the suspension if available. Then, the stability of the linearized equations of motion[1] determined by the real part of the eigenvalues of the system matrix can be analyzed, as will be discussed in more detail in section 2.1. This procedure is referred to as complex eigenvalue analysis (CEA) in the automotive industry and allows to account for uneven stress distributions at the interface between brake disc and pads due to application of the brake pressure, for orthotropic material behavior of the pad or for material and friction-induced damping [9, 24, 30, 60, 92]. It is even possible to take into account acoustic radiation [85], gyroscopic terms [58] or thermal deformation [38]. Nevertheless, it is known that the CEA frequently over- or sometimes underestimates the susceptibility to brake squeal of a given brake system [60]. This encourages many engineers and scientists to analyze the system additionally or solely in the time-domain [1, 73, 92]. Also, doubts can be cast on whether results of the CEA have a meaning for brake discs that are not full discs [110]. This will be discussed in more detail in section 2.2.2.

Most publications concerning brake squeal are related to the automotive industry or discuss brake systems used in this context. Though, it also occurs in other applications like aircraft, trains, motorcycles and bicycles. Squeal phenomena occuring at railway block brakes are discussed in [124], while Lorang et al. study brake squeal of the French TGV train [70]. The effects and frequency ranges are similar to that found in brake systems in the automotive industry. This is not the case for aircraft brake systems, where not only the frequency range of friction induced vibrations is different, but also the fact that torsional modes of parts of the brake system dominate its vibrational

[1] Here, a seeming inconsistency must be pointed out: From a Lyapunov perspective, it does only make sense to speak of the stability of a solution of the equations of motion and not of the stability of the equations of motion themself or of the stability of the (brake) system. However, the stability is assessed here by an analysis of the equations of motion linearized about a solution representing the steady-sliding-state of the disc in frictional contact. Therefore, the eigenvalues of this linear system indeed do determine the stability of the steady-sliding state, which is searched for. If, for a shorter notation, the stability of the equations of motion is mentioned in this thesis, always the stability of the steady-sliding state is meant determined by the stability of the trivial solution of the equations of motion linearized about this steady state.

behavior [103]. NAKAE et al. experimentally study noise generated by bicycle disc brakes and examine the presence of two phenomena, which they denote as "squeal" and "chatter" [79]. While squeal occurs at a large temperature range starting at room temperature, chatter only occurs at very high temperatures around and above 300° Celsius. Squeal is related to a velocity-dependent friction coefficient in their work, while chatter originates in a coupling between an in- and out-of-plane eigenmode at 500 Hz and 1000 Hz, respectively. This is particularly interesting since the modeling and experiments presented in this thesis considering bicycle brake discs show that squeal in these cases is dominated by out-of-plane vibrations. It is far closer related to squeal phenomena in automotive disc brakes and can be treated with the same structural optimization procedure, as is discussed in section 4.5.

1.3 Brake squeal countermeasures

Although publications can be found solely intended to give insight into the excitation mechanism and characteristics of brake squeal, many others also present methods for brake squeal avoidance. Despite the fact that brake squeal has been studied since at least seven decades, there is no general remedy known against brake squeal in a robust sense [60]. Many brake parameters such as the brake pad stiffness vary considerably over the lifetime of the brake system, being sensitive to changes in the environmental conditions, temperature and/or wear. Furthermore, the pressure in the automotive industry is very high to use low cost, lightweight and environmentally friendly solutions. This complicates the development of squeal countermeasures. There are many solutions discussed in the engineering community, though, of which at least some have found their way to practical application. Basically, they can be divided into active and passive measures. Active or semi-active measures make use of sensors and actuators to inhibit brake squeal, e.g. brake pads with included piezoelectric devices, and have been demonstrated to be highly effective against squeal [20, 40, 42, 45, 80–82, 123]. Nevertheless, these measures are not widely used in practice since they are elaborate to tune and expensive. This is different for most passive squeal avoidance methods including:

brake rotor material with high damping, such as specially alloyed gray cast iron [26], damping rings decreasing vibrational amplitudes by friction-induced damping [24, 25], laminated brake discs that also increase friction-induced damping [61], chamfered and/or slotted brake pads [67] and shims, which are small, often laminated metal or rubber plates enhancing the damping of the brake assembly [46, 134]. These measures work for some brake systems, however, they are not generally applicable for all squealing brakes.

Another approach to avoid brake squeal passively has been studied in [121] and by Nishiwaki et al. [84] and Fieldhouse et al. [28]. They demonstrated experimentally that the introduction of asymmetry into the brake rotor inhibits the generation of brake squeal. The asymmetry of the brake rotor splits its double eigenfrequencies and therefore helps to stabilize the brake disc in frictional contact with the brake pads. This will be explained in detail in section 2.2. It leads to a structural optimization problem for the separation of eigenfrequencies, which is the main topic of this thesis.

1.4 Outline of the thesis

After this introduction discussing the excitation mechanism of brake squeal, its modeling and possible countermeasures, the next chapters of this thesis are organized as follows. In the second chapter, the avoidance of brake squeal by an introduction of asymmetry into the brake rotor is presented in detail. A definition of asymmetry useful in the context of squeal avoidance is given. As brake squeal can be seen as stability problem, it is shown that the conventional methods to determine stability by the calculation of the real parts of the system matrix of the linearized equations of motion do not deliver satisfying results for asymmetric brake discs. Modeling of such asymmetric discs leads to equations of motion with periodic coefficients. Still, the stability boundary can be approximated analytically. From this approximation, design criteria for squeal free asymmetric discs can be deduced, which lay the basis for a comprehensive structural optimization of brake rotors to avoid squeal. In chapter 3, a modeling technique for brake discs is introduced that allows for an efficient optimization with large changes in the geometry. First, the basic

concept and the mathematical background are given followed by an analysis of two simple examples, an inhomogeneous rod and a rectangular plate with a rectangular or circular hole, whose eigenfrequencies are calculated. The latter example is used to conduct a detailed convergence study, which shows the advantageous convergence behavior of the method. Afterwards, this modeling technique is applied to automotive and bicycle brake discs. In the fourth chapter, the structural optimization problem is introduced to split as far as possible the eigenfrequencies of a brake rotor in a predefined frequency band to inhibit brake squeal. Automotive brake discs with radial holes are optimized and the results are experimentally validated followed by the optimization of a more realistic brake disc with cooling channels. Then, bicycle brake discs are optimized, manufactured and tested on a test rig to assess the efficacy of the optimization. It is shown that the best optimized brake rotors indeed largely lower the squeal affinity of the brake system, which strongly supports the statements made in the second chapter. Finally, a short summary concludes this thesis in chapter 5.

2 Avoidance of brake squeal by breaking symmetries

In this chapter, it is shown that asymmetry of the brake rotor is a measure against brake squeal and design goals for asymmetric rotors will be deduced, forming the basis for the structural optimization presented in later chapters. Since symmetric brake rotors exhibit double eigenfrequencies when they do not rotate and are not in contact with the brake pads, they are susceptible to a flutter-type instability when rotating in frictional contact with the brake pads. This leads to self-excited vibrations and squeal. It can be shown mathematically that asymmetry splits the double eigenfrequencies of the brake disc enlarging the stability region up to a level of complete squeal avoidance. The minimal necessary distance between the eigenfrequencies of the rotor will be derived based on geometry and material parameters of the disc and the brake pad, as well as the frequency range in which squeal is possible. These design criteria can help to improve the brake design process.

2.1 Brake squeal as a stability problem

As has already been stated in the introduction, researchers agree that brake squeal originates in the frictional contact between brake pad and brake rotor [60, 92]. The steady-sliding-state solution of the rotating rotor can become unstable, the resulting self-excited vibrations are then audible as brake squeal. After discretization, a linearization about the steady state of the disc rotating with constant angular velocity Ω leads in the easiest case for a full rotor (without cooling channels, holes or chamfers) to equations of motion with constant coefficients given as

$$\mathbf{M}\ddot{\mathbf{q}} + (\mathbf{D} + \mathbf{G})\,\dot{\mathbf{q}} + (\mathbf{K} + \mathbf{N})\,\mathbf{q} = \mathbf{0}, \tag{2.1}$$

under the assumption of an appropriate reference frame. $\mathbf{M} = \mathbf{M}^{\mathrm{T}}$ represents the positive definite mass matrix, $\mathbf{D} = \mathbf{D}^{\mathrm{T}}$ the positive definite or positive semi-definite damping matrix, $\mathbf{G} = -\mathbf{G}^{\mathrm{T}}$ the skew-symmetric matrix of the gyroscopic terms, while $\mathbf{K} = \mathbf{K}^{\mathrm{T}}$ is the stiffness matrix, $\mathbf{N} = -\mathbf{N}^{\mathrm{T}}$ the skew-symmetric matrix with circulatory terms and $\mathbf{q} = \mathbf{q}(t)$ the vector of generalized coordinates. Due to the frictional contact between pads and disc, unwanted energy transport can take place from the rotation of the disc to vibrations of the disc perpendicular to the rotational axis, which are mainly out-of-plane vibrations. This finds its representation in the linearized case in the instability of the equations of motion leading to an onset of vibrations caused by the nonconservative matrix $\mathbf{N}$. The gyroscopic terms $\mathbf{G}$ result from the rotation of the disc and despite the fact that the rotational speed is small, they can have significant influence on the stability behavior [43,109,112]. The damping matrix $\mathbf{D}$ contains entries from material damping and terms caused by the kinematic linearization of nonlinear friction terms.

The stability of the equations of motion (2.1) is determined by the real parts of their eigenvalues. It is well known that the presence of circulatory terms $\mathbf{N}$ (and gyroscopic terms $\mathbf{G}$) can result in eigenvalues λ with a positive real part

$$\mathrm{Re}\,(\lambda) > 0, \tag{2.2}$$

leading to a potentially unstable system. In the absence of damping and with $\mathbf{G} \neq \mathbf{0}$ and $\mathbf{N} \neq \mathbf{0}$, the system always has at least one eigenvalue with vanishing or positive real part, in most cases it is unstable [36]. The positive real parts cause the solution of the linear equations of motion $\mathbf{q}(t) = \hat{\mathbf{q}} e^{\lambda t}$ to grow exponentially with time, which does not happen in the physical system. The linear system can only represent the onset of self-excited vibrations, the amplitudes of the vibrations will be limited by nonlinear effects, e.g. originating from nonlinear material behavior of the brake pad leading to limit cycle oscillations. Still, the above mentioned analysis is the core of the CEA. If a damping matrix is present, the structure of the this matrix decides whether it has a stabilizing or destabilizing effect, due to the presence of circulatory terms, even if it is positive semi-definite or positive definite. A short dis-

cussion about the influence of the structure of the damping matrix therefore follows in section 2.2.4.

Kinkaid et al. [60] report that North was the first in 1972 to develop a disc brake model with a non-symmetric "stiffness matrix"[1] $\mathbf{K}+\mathbf{N}$ due to the presence of dry friction with a constant coefficient of friction. The friction-induced terms in this matrix can lead to at least one positive real part of the eigenvalue. This type of instability is known as flutter instability. It was first reported in the analysis of flutter of aircraft wings showing the same excitation mechanism through circulatory forces except that in aircraft wings the self-excitation is created by airflow and not by friction forces. The enhancing modeling capabilities and the deepening understanding of brake squeal led to continuous models with a more precise representation of the excitation mechanism [48,49,60,92,94], as has already been reported in the introduction. It is an important characteristic of brake squeal that a standing wave (fixed in the inertial frame) can be generated on the rotating disc during squeal and that the two responsible coupled eigenmodes are attributed to a double eigenfrequency or two frequencies in direct vicinity to each other, at least when bending of the disc dominates its behavior.

While in the standard CEA procedure in the automotive industry only the stability of the linear equations of motion is analysed, some authors in the recent past promote the analysis of the system including possible nonlinear effects in addition to the dry friction between brake disc and pad [18, 41, 73, 92, 102, 111]. The most important of these is the highly nonlinear material behavior of the brake pad, but there are also others such as damping caused by the friction in the joints between brake disc and suspension. Still, these nonlinearities are frequently not well known in practice. Despite the fact that nonlinear effects are mostly neglected in the FE-based analysis of brake discs in frictional contact, a second issue is that any brake system that does not have a full disc as rotor cannot be modelled with constant coefficients [110]. This will be discussed in depth in the next section, where the

[1] In the literature, $\mathbf{K}+\mathbf{N}$ is sometimes referred to as "stiffness matrix". However, in this thesis the term stiffness matrix is reserved for the symmetric part $\mathbf{K}$, which corresponds to a potential energy expression. The matrix $\mathbf{N}=-\mathbf{N}^{\mathrm{T}}$ denotes the circulatory terms, for which no energy expression can be defined.

benefits of asymmetry of the brake rotor will be presented after a definition of asymmetry suitable for the purposes of this thesis. This introduces the basis for a comprehensible structural optimization of asymmetric brake rotors for squeal avoidance purposes, which is presented in later chapters.

2.2 Splitting of the brake rotor's eigenfrequencies by asymmetry

As is known since a long time, asymmetry of brake discs helps to avoid squeal. First patents for asymmetric brake discs can at least be dated back to the 1960s [22] and 1980s [78, 86], mainly motivated by experimental findings. Later, Suga and Katagiri patented a brake disc with unequally spaced radial grooves also for squeal avoidance purposes [116]. Nishiwaki et al. [84] and Fieldhouse et al. [28] also studied the influence of asymmetries on the stability of the brake rotor in frictional contact with the brake pad experimentally. They could clearly show that squeal at distinctive frequencies could be avoided by adding point masses to the brake rotor or by removing small portions of material by machining to introduce asymmetry to the disc. Their work was based on the experimental insight that the splitting of two eigenfrequencies in direct vicinity to each other and the squealing frequency inhibits squeal at this frequency. However, it did not provide a mathematical background for the squeal avoidance by asymmetry.

2.2.1 Definition of asymmetry in the context of squeal avoidance

Before explaining this mathematical background, it is necessary to define "symmetry" and "asymmetry" in the context of brake rotors, since the meaning of these terms is not clearly defined and differs in the relevant literature on brake squeal. Here, the approach to "symmetry" and "asymmetry" is from an engineering perspective (see the literature on group theory for a more rigorous mathematical approach [98, 115]). Most engineers have a certain intuitive understanding of symmetry and asymmetry, however, this does not always

correspond to an exact definition and is thus not useful without clarification. Since in the literature the term asymmetry mainly refers to brake rotors which are modified with respect to their midplane perpendicular to the axis of rotation, only a 2D view on symmetries is presented here, corresponding to a top view on the actual brake disc. There are three types of symmetry important for the analysis of brake discs from a geometric point of view. These are visualized in Fig. 2.1 by four examples of a brake disc with different configurations of cooling ribs.

The first type is the symmetry with respect to one or more axes. Fig. 2.1, a) presents an example of a brake disc with four cooling ribs in a configuration which is symmetric with respect to two perpendicular axes in the shown 2D plane[2]. This configuration would without doubt intuitively be denoted as "symmetric" by most engineers. The second type of symmetry, the point-symmetry, is shown in Fig. 2.1, b). The six cooling ribs are arranged such that there is no axis of symmetry in the plane depicted, however, the ribs are arranged point-symmetric to the midpoint of the disc. Most engineers are familiar with these two types of symmetry, which might not be the case for the third type. This third class of symmetry discussed here is the cyclic symmetry, which is often exploited in FE codes to reduce the computational effort of calculations involving cyclic symmetric structures. Cyclic symmetry refers to the fact that structures exhibiting this type of symmetry can be divided into N_{cyc} equally sized sectors of exactly the same shape. Each sector spans an angle of $\Delta\varphi_{\mathrm{cyc}} = 2\pi/N_{\mathrm{cyc}}$. One example of a brake disc exhibiting a cyclic symmetry with 3 sectors, each spanning an angle of $2\pi/3$, is shown in Fig. 2.1, c). The lines dividing the three sectors of same shape are dotted. Fig. 2.1, d) finally shows a disc with one cooling rib which exhibits symmetry with respect to one axis only. However, despite the presence of one symmetry line, some engineers certainly would identify this brake disc as "asymmetric".

This approach to "symmetry" and "asymmetry" is geometrically motivated and thus, one possible definition of "symmetric" and "asymmetric" brake rotors is the following. If the disc exhibits one or more axes of symmetry, point-

[2]The two depicted perpendicular axes of symmetry are not the only ones. Rotating them by 45° results in a second set of symmetry axes.

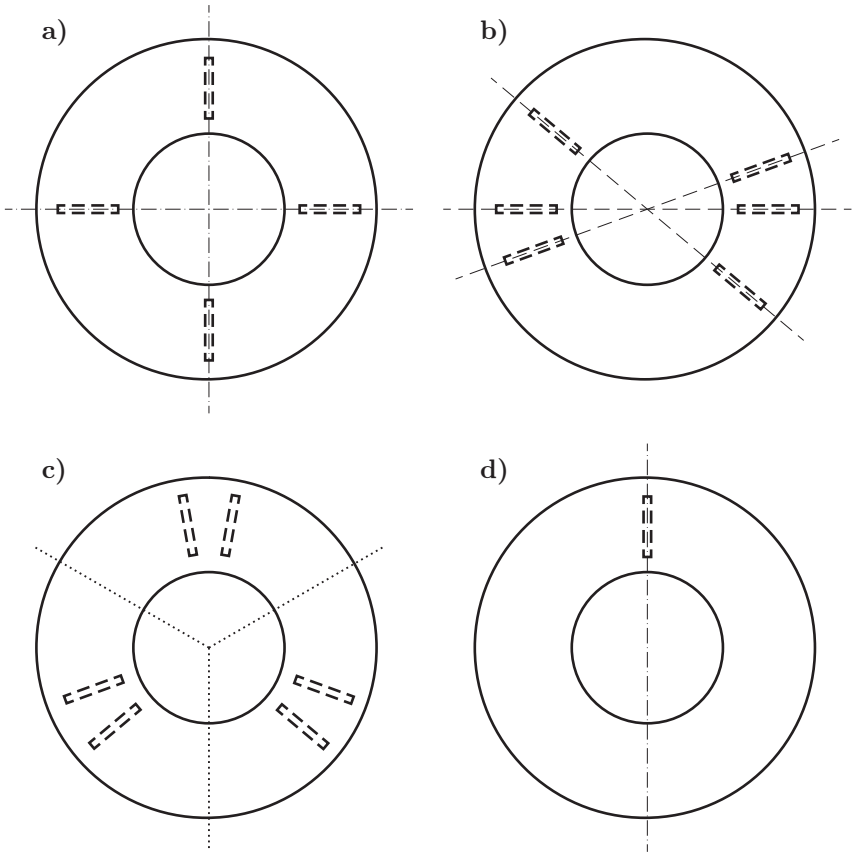

Figure 2.1: Top view on brake discs with different layouts of cooling ribs. a) Four cooling ribs with two axes of symmetry. b) Six cooling ribs with point symmetry. c) Six cooling ribs with cyclic symmetry. d) One cooling rib with one axis of symmetry.

symmetry or cyclic symmetry, it is defined as geometrical symmetric disc. If it lacks any of these types of symmetry, it is a geometrical asymmetric one. Despite being reasonable, this definition alone is not sufficient for the purposes of this thesis due to two facts. First, it does not agree with the

present denomination of "asymmetric" brake discs in the literature dealing with brake squeal, which exhibit e.g. a cyclic symmetry [28]. Second, a direct relation between brake squeal and geometrical symmetry cannot be deduced. This motivates a different approach which correlates to the understanding of "asymmetry" of researchers working in the field of brake squeal and its avoidance.

The idea behind all approaches presented in the first paragraph of section 2.2 to introduce "asymmetry" to the brake rotor is to prevent the "mode lock-in" effect discussed in the introduction. Measurements conducted by NISHIWAKI et al. [84] or FIELDHOUSE et al. [28] showed brake squeal with one dominating frequency. "Mode lock-in" occurred at this frequency, which could be seen by the standing waves (spatially fixed in the inertial frame) generated on the rotating disc resembling the eigenmode corresponding to the double eigenfrequency involved in the "mode lock-in" effect. With the attachment of single masses or the removal of a small portion of mass from the disc it was possible to remove the coupling of the two eigenmodes, destroy the generated standing wave, stabilize the system and thus prevent squeal. "Asymmetry" therefore refers to the fact that a double eigenfrequency of the nonrotating brake disc, not in contact with the brake pads, is split. It is well known that annular discs (having two perpendicular axes of symmetry) have double eigenfrequencies with two corresponding, orthogonal eigenmodes [35]. Sometimes the eigenvalues, of which these eigenfrequencies are the imaginary part, are referred to as semi-simple to distinguish them from nonderogatory double eigenvalues with only one corresponding eigenmode (or eigenvector) [99]. However, in this thesis only double eigenfrequencies with two orthogonal eigenmodes occur, so that this distinction is not necessary here. Some other continuous systems like strings or EULER-BERNOULLI beams cannot have double eigenfrequencies due to the STURM-LIOUVILLE characteristics of the underlying differential equations [35]. Also for discs with cyclic symmetry, which does not necessarily correspond to the presence of two axes of symmetry, it can be proven that they exhibit at least one double eigenfrequency for $N_{\mathrm{cyc}} > 2$ [108]. While in some cases the understanding of "asymmetry" in this context of splitting one or more double eigenfrequencies corresponds to the absence of the

geometrical types of symmetry presented above, this is not always the case. A full disc as well as a disc with cyclic symmetry would therefore not be an "asymmetric" one in the sense of a split in eigenfrequencies, while a disc with one axis of symmetry (Fig. 2.1, d)) would be "asymmetric" in this sense due to the fact that its eigenfrequencies are split. In order to distinguish the geometric symmetry from "symmetry" or "asymmetry" in the sense of split double eigenfrequencies, the following definition is helpful and will be used throughout this thesis.

Definition 1. *A structure exhibiting one or more double eigenfrequencies in a specific frequency band is defined as modal symmetric structure. All eigenfrequencies of modal asymmetric structures are split in a specific frequency band.*

For brake discs, one reasonable choice of the frequency band is the audible frequency range up to 20 kHz. Other definitions of the frequency band are possible and meaningful as will be shown in section 2.2.3. Definition 1 corresponds more to the intuition of "asymmetry" researchers on brake squeal have in mind than the geometrical asymmetry presented before. Furthermore it will be mathematically shown in the next section that modal asymmetric brake rotors prevent squeal.

Definition 1 also allows the introduction of grades in "asymmetry" of a given brake disc.

Definition 2. *The grade of modal asymmetry of a given structure is determined by the minimal distance between its eigenfrequencies. The higher this distance is, the higher is the grade of modal asymmetry.*

In general, the grade of modal asymmetry can be defined as an absolute or relative value. However, considerations given in 2.2.3 prove that it is more useful to take into account the absolute value for the case of modal asymmetric brake rotors.

Modal asymmetry can be introduced to brake discs by altering the mass and/or stiffness distribution of the rotor. In the easiest case by attachment of point masses, as has been done by Nishiwaki et al. [84], or in a more

sophisticated approach by changing the geometry of the brake disc, e.g. the distribution of cooling channels or the introduction of axial or radial holes. While the avoidance of geometric asymmetry is helpful in this context, it is not always necessary: A brake disc can be modal asymmetric in the audible frequency range and still exhibit a cyclic symmetry as does the brake disc presented in [28]. In the next section, the mathematical background of squeal avoidance by asymmetry will be explained in depth and the usefulness of Def. 2 will become obvious.

2.2.2 Analysis of asymmetric brake rotors

The analysis of rotating, flexible, full brake discs in frictional contact to brake pads after discretization and linearization leads to equations of motion (2.1) with constant coefficients (if an appropriate reference frame is chosen). This is not the case for all other brake systems as long as they are in contact to brake pads that do not span the whole circumference of the disc, e.g. brake discs with cooling channels. The equations of motion have then in the most general case the form

$$\mathbf{M}(t)\ddot{\mathbf{q}} + (\mathbf{D}(t) + \mathbf{G}(t))\,\dot{\mathbf{q}} + (\mathbf{K}(t) + \mathbf{N}(t))\,\mathbf{q} = \mathbf{0} \tag{2.3}$$

and have time-dependent, periodic system matrices defined as for the constant case (see Eq. (2.1)). The modeling, e.g. with flexible or rigid rotor, and the choice of coordinates, either in a frame fixed to the rotating disc or in the inertial, stationary frame, determines the allocation of the system matrices [109]. It is possible that at least some of the system matrices are allocated with constant entries with a smart choice of coordinates, however, always at least the stiffness matrix $\mathbf{K}$ and/or the circulatory matrix $\mathbf{N}$ have time-dependent coefficients. Consider a flexible brake disc with four cooling ribs as shown in Fig. 2.1, a): its stiffness (in a point-wise sense) depends on the position on the brake disc. The stiffness in axial direction is higher where the friction rings are supported by the cooling ribs and lower in between. If the coordinates are set up in the inertial frame, which is the standard choice for common FE tools, the stiffness matrix is periodic since the stiffness of the disc varies with

the position on the disc and therefore during the rotation also with time. The lowest period T of the change of the coefficients is given by $T = 2\pi / (N_{\mathrm{cyc}}\Omega)$, where Ω is the circular frequency of the disc and $N_{\mathrm{cyc}} = 4$ in the case shown in Fig. 2.1, a). If a rotating frame is chosen to avoid the time-dependence of the stiffness matrix, the circulatory matrix becomes periodic, since then the brake pads rotate with the circular frequency Ω and affect only parts of the brake disc at each time step; the material points staying in contact with the pad change over time.

It is well known that the stability of equations of motion with periodic coefficients cannot be determined by a standard eigenvalue analysis, since the periodic system does not admit solutions of the type $\mathbf{q}(t) = \hat{\mathbf{q}}e^{\lambda t}$. Though, it can be studied using FLOQUET theory [34]. A procedure like the CEA implemented in state-of-the-art FE software like ANSYS or ABAQUS to assess the stability of the brake system is therefore not applicable in a strict sense, but is still widely used in industry [110]. This leads to the following contradiction considering geometric and/or modal asymmetric brake discs: it is known from experiments that asymmetry and a split of double eigenfrequencies of the brake disc is helpful to avoid squeal, which is introduced by changing its geometry, stiffness or mass distribution. But the simulation in common FE tools with the CEA cannot be used to tune the measures correctly, since the calculated real parts of the eigenvalues, which are the most important CEA results, have no meaning for the stability of the system.

Since analytical or semi-analytical modeling is very limited in the case of geometrical and modal asymmetric brake discs due to their complex geometry and common FE tools presently cannot be used properly for the stability analysis of brake discs requiring a modeling with periodic system matrices, a different approach is chosen here. This approach has been developed in the past years [43, 106–109, 113, 122] and leads to a mathematical justification for the experimental finding that splitting of double eigenfrequencies of the non-rotating brake rotor leads to a stabilization of the system and an avoidance of brake squeal. The basic assumption of the approach is that the terms originating from the frictional contact between brake pad and brake disc are small compared to the elastic restoring terms. This assumption includes the

position dependent stiffening terms by the brake pad as well as the circulatory terms and is reasonable for brake systems used in practice, for which the stiffness of the brake pad is by magnitudes smaller than the stiffness of the metal rotor [40]. The discretized equations of motion can then be written as

$$\mathbf{M}\ddot{\mathbf{q}} + (\delta(\epsilon)\mathbf{D}(t) + \mathbf{G}(t))\,\dot{\mathbf{q}} + \left(\mathbf{K} + \kappa(\epsilon)\overline{\mathbf{K}}(t) + \gamma(\epsilon)\mathbf{N}(t)\right)\mathbf{q} = \mathbf{0}. \tag{2.4}$$

The terms $\delta(\epsilon)\mathbf{D}(t)$, $\mathbf{G}(t)$, $\kappa(\epsilon)\overline{\mathbf{K}}(t)$ and $\gamma(\epsilon)\mathbf{N}(t)$ are perturbations of the unperturbed problem

$$\mathbf{M}\ddot{\mathbf{q}} + \mathbf{K}\mathbf{q} = \mathbf{0}. \tag{2.5}$$

The perturbations result from damping of the brake system ($\mathbf{D}(t)$), from asymmetry of the rotor or stiffness of the brake pads ($\overline{\mathbf{K}}(t)$) and from the frictional contact between pads and disc ($\mathbf{N}(t)$). Also, the matrix of gyroscopic terms $\mathbf{G}(t)$ will be "small" for the low range of angular velocities important for brake squeal and can therefore be treated as perturbation. The denomination of the system matrices follows the case with constant coefficients (Eq. (2.1)), but here the system matrices are assumed to be normalized such that

$$\mathbf{M} = \mathbf{I}, \tag{2.6a}$$

$$\mathbf{K} = \mathrm{diag}(\omega_1^2, \omega_2^2, \ldots, \omega_P^2), \tag{2.6b}$$

where $\mathbf{I}$ is the identity matrix. The unperturbed system has P circular eigenfrequencies ${\omega_i}$[3], of which some can be double if the system is modal symmetric. The parameters $\delta(\epsilon)$, $\kappa(\epsilon)$ and $\gamma(\epsilon)$ determine the influence of the damping, stiffness and circulatory matrices in the perturbation analysis and are assumed to depend on the perturbation parameter ϵ. Thus, it is possible to expand all of them in terms of ϵ as

$$\delta(\epsilon) = \delta_1\epsilon + \delta_2\epsilon^2 + \ldots, \tag{2.7a}$$

$$\kappa(\epsilon) = \kappa_1\epsilon + \kappa_2\epsilon^2 + \ldots, \tag{2.7b}$$

[3] In this thesis, circular frequencies are referred to as ω, while f refers to frequencies. The same holds for eigenfrequencies.

$$\gamma(\epsilon) = \gamma_1\epsilon + \gamma_2\epsilon^2 + \dots. \tag{2.7c}$$

The stability of the trivial solution of Eq. (2.4) can be analyzed using FLOQUET theory and is determined by the magnitude of the eigenvalues ρ_j of the monodromy matrix, which are also called FLOQUET multipliers [34]. The analysis of the stability of Eq. (2.4) presented in short form here can be found in detail in [107, 109]. The notation follows these publications.

An expansion of the eigenvalues of the monodromy matrix in terms of the perturbation parameter ϵ leads to

$$\rho_j = \rho_{0j} + \left.\frac{\partial\rho_j}{\partial\epsilon}\right|_{\epsilon=0}\epsilon + \dots, \tag{2.8}$$

where ρ_{0j} corresponds to the unperturbed problem (2.5). It has a magnitude of $|\rho_{0j}| = 1$, which represents the stability boundary in FLOQUET theory, since the unperturbed problem is weakly stable. Therefore, the stability is determined by the magnitude of the derivative of the FLOQUET multiplier, which can be determined by

$$\left.\frac{\partial\,|\rho_j|}{\partial\epsilon}\right|_{\epsilon=0} = \frac{1}{|\rho_{0j}|}\mathrm{Re}\left(\rho_{0j}^*\left.\frac{\partial\rho_j}{\partial\epsilon}\right|_{\epsilon=0}\right) \tag{2.9}$$

with ρ_{0j}^* being the complex conjugate of ρ_{0j}. The solution of the system under investigation is stable if the derivative of the FLOQUET multiplier is negative and therefore directed into the stability region. It is shown in [107, 109] that the double, semi-simple eigenvalues of the monodromy matrix ρ_{0j} are important for the investigation of the stability of (2.4) and that $\partial\rho_j/\partial\epsilon|_{\epsilon=0}$ can be calculated from

$$\begin{aligned} 0 = \det\Bigg(\int_0^{2\pi}\frac{-\rho_{0j}}{2}\left(\delta_1\mathbf{D}(t) + \mathbf{G}(t)\right. \\ \left. + \frac{\mathrm{i}}{\omega_j}\left(\kappa_1\overline{\mathbf{K}}(t) + \gamma_1\mathbf{N}(t)\right)\right)\mathrm{d}t - \left.\frac{\partial\rho_j}{\partial\epsilon}\right|_{\epsilon=0}\Bigg). \end{aligned} \tag{2.10}$$

For further considerations, the perturbation parameters δ_1, κ_1 and γ_1 are set equal to 1, without loss of generality. The argument of the determinant in Eq. (2.10) can be reduced to a 2x2-system due to the fact that the double

eigenvalues of the monodromy matrix correspond to double eigenfrequencies $\omega_i = \omega_j$ of the unperturbed system (2.5), see [107, 109]. Therefore, only entries d_{ij}, g_{ij}, $\overline{k}_{ij}$ and n_{ij} of the time-dependent system matrices $\mathbf{D}(t)$, $\mathbf{G}(t)$, $\overline{\mathbf{K}}(t)$ and $\mathbf{N}(t)$ enter the equations that belong to the double eigenfrequencies $\omega_i = \omega_j$. After performing an orthogonal transformation that diagonalizes $\overline{\mathbf{K}}(t)$, Eq. (2.10) can then be written as

$$\begin{aligned} 0 = \det \Bigg(\frac{-\rho_{0j}}{2} \Bigg(& \begin{bmatrix} d & \widetilde{d} \\ \widetilde{d} & d + \Delta d \end{bmatrix} + \begin{bmatrix} 0 & g \\ -g & 0 \end{bmatrix} \\ & + \frac{\mathrm{i}}{\omega_j} \left(\begin{bmatrix} \overline{k} & 0 \\ 0 & \overline{k} + \Delta k \end{bmatrix} + \begin{bmatrix} 0 & n \\ -n & 0 \end{bmatrix} \right) \Bigg) - \left. \frac{\partial \rho_j}{\partial \epsilon} \right|_{\epsilon=0} \begin{bmatrix} 1 & 0 \\ 0 & 1 \end{bmatrix} \Bigg). \end{aligned} \tag{2.11}$$

The terms d, Δd, $\widetilde{d}$, g, $\overline{k}$, Δk and n are given by

$$d = \int_0^{2\pi} d_{ii}(t)\,\mathrm{d}t, \tag{2.12a}$$

$$\Delta d = \int_0^{2\pi} d_{jj}(t)\,\mathrm{d}t - \int_0^{2\pi} d_{ii}(t)\,\mathrm{d}t, \tag{2.12b}$$

$$\widetilde{d} = \int_0^{2\pi} d_{ij}(t)\,\mathrm{d}t = \int_0^{2\pi} d_{ji}(t)\,\mathrm{d}t, \tag{2.12c}$$

$$g = \int_0^{2\pi} g_{ij}(t)\,\mathrm{d}t = -\int_0^{2\pi} g_{ji}(t)\,\mathrm{d}t, \tag{2.12d}$$

$$\overline{k} = \int_0^{2\pi} \overline{k}_{ii}(t)\,\mathrm{d}t, \tag{2.12e}$$

$$\Delta k = \int_0^{2\pi} \overline{k}_{jj}(t)\,\mathrm{d}t - \int_0^{2\pi} \overline{k}_{ii}(t)\,\mathrm{d}t, \tag{2.12f}$$

$$n = \int_0^{2\pi} n_{ij}(t)\,\mathrm{d}t = -\int_0^{2\pi} n_{ji}(t)\,\mathrm{d}t, \tag{2.12g}$$

with $j > i$. The stiffness matrix is diagonalized and therefore the disc's modal asymmetry is represented by Δk, which can be expressed by

$$\Delta k = 2\pi\Delta\omega^2, \tag{2.13}$$

with the difference between between two neighboring eigenfrequencies $\Delta\omega = \omega_l - \omega_k$. This difference is induced by the rotating asymmetry of the brake disc, where asymmetry in the sense used here refers to geometric modifications of the disc or modifications in the mass and/or stiffness distribution. If this asymmetry is not present, $\Delta\omega = 0$ and the eigenfrequencies under consideration ω_k and ω_l are the double eigenfrequencies $\omega_i = \omega_j$. The damping matrix, however, is not guaranteed to be diagonal, therefore the terms Δd and $\widetilde{d}$ account for the most general structure of the damping matrix.

The following first order approximation of the stability boundary given by $\left.\frac{\partial\,|\rho_j|}{\partial\epsilon}\right|_{\epsilon=0}$ under the consideration of Eqs. (2.9) and (2.8) can be deduced from Eq. (2.11):

$$\begin{aligned} 0 = &-\left(\frac{d}{2} + \frac{\Delta d}{4}\right) \\ &+ \mathrm{Re}\left(\sqrt{\frac{\Delta d^2}{16} + \frac{\widetilde{d}^2}{4} + \frac{n^2}{4\omega_j^2} - \frac{g^2}{4} - \frac{\Delta k^2}{16\omega_j^2} + \mathrm{i}\left(\frac{\Delta d\Delta k}{8\omega_j} - \frac{gn}{2\omega_j}\right)}\right). \end{aligned} \tag{2.14}$$

This is the general case of the stability boundary achieved by perturbation theory and could directly be evaluated numerically. However, for the next steps the gyroscopic terms g will be neglected and the damping matrix will be assumed to be diagonal with $\Delta d = 0$ and $\widetilde{d} = 0$. This enables an analytical evaluation of Eq. (2.14) and therefore an analytical approximation of the stability boundary. The influence of the gyroscopic terms and of the structure of the damping matrix will be discussed in section 2.2.4 based on numerical evaluations. Still, these numerical studies show that the most important parameters influencing the stability are covered by the analytical approximation presented in the following.

For $g = 0$, $\Delta d = 0$ and $\widetilde{d} = 0$, Eq. (2.14) simplifies to

$$0 = -4d^2\omega_j^2 - \Delta k^2 + 4n^2 = s\left(d, \Delta k, n, \omega_j\right). \tag{2.15}$$

The steady-sliding state of the system is stable for $s < 0$ and unstable for $s > 0$, since the derivative of the FLOQUET multiplier then directs into the stable region or into the unstable one, respectively (see Eq. (2.8)). Thus, the damping d and the split between neighboring eigenfrequencies Δk act as stabilizing, while n destabilizes.

This mathematical derivation justifies the experimental evidence that splitting eigenfrequencies of the brake rotor helps to avoid squeal, which is an important basis for the following steps and the structural optimization of the brake rotor. For given circulatory terms n and damping d, a certain split of eigenfrequencies (represented by Δk) is necessary to stabilize the solution of the equations of motion leading to a minimal required grade of modal asymmetry of the brake rotor. Since the brake disc can have many pairs of double eigenfrequencies or closely spaced ones, it is necessary to introduce a split of eigenfrequencies for all pairs in a certain frequency range to assure stability. In the next section an estimate of the minimal necessary distance between eigenfrequencies is presented and the frequency range in which this has to be achieved. These are the criteria for the design of squeal free brakes.

2.2.3 Design criteria for squeal free brakes

The analysis in this section has been published originally in [125]. The minimal necessary distance Δf between eigenfrequencies of the rotor can directly be achieved by transformation of Eq. (2.15) under consideration of Eq. (2.13). This leads to

$$\Delta f = \frac{1}{2\pi} \sqrt[4]{\frac{1}{\pi^2} \left(n^2 - 4\pi^2 d^2 f_j^2 \right)} \tag{2.16}$$

with the double eigenfrequency f_j. If the brake system under consideration is known and modeled in detail and therefore the circulatory terms n and the damping d are known to a certain precision, Δf can be calculated directly. However, it is highly desirable to be able to estimate Δf before a final brake design is known, in order to conduct a structural optimization to achieve this split to avoid squeal in the final brake disc. Therefore, in the following, an estimate for the minimal necessary distance will be derived.

To achieve this, the terms n and d of Eq. (2.16) have to be estimated. In order to reach a reasonable estimate of n with all important parameters of the brake system, the easiest continuous model of a brake disc in frictional contact will be taken as a basis. This is the circular beam in contact to a massless friction pin connected to a linear spring. The pin is the most simple representation of the brake pad and the circular beam is a model of the brake disc that can be handled semi-analytically and includes all major influences of the structure exhibiting self-excited vibrations. The beam has many double eigenfrequencies and also the correct contact kinematics is considered leading to circulatory terms which are periodic if the beam is modelled in a rotating frame[4]. In Fig. 2.2 the beam rotating with a constant rotational frequency Ω is shown in contact with two pins connected to springs of stiffness k with a friction coefficient μ between pin and beam.

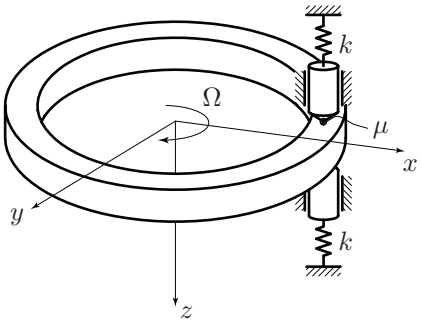

Figure 2.2: Circular beam in frictional contact to massless pins. Sketch adopted in a modified form from [109].

Under consideration of this beam model, the circulatory term n can be estimated by

$$n \leq \frac{2\pi h k \mu \hat{w}_i \hat{w}'_j}{r_p m_G}, \tag{2.17}$$

[4]It seems to be more convenient to set up the equations of motion in a stationary frame to achieve constant coefficients, however, here they are set up in a rotating frame such that they have the form presented in section 2.2.2.

as is shown in [109], where the thickness of the brake disc is denoted as h, r_p is the radius to the midpoint of the brake pad and k is its overall stiffness simplified here as a linear spring. The generalized mass corresponding to the double eigenfrequency $f_i = f_j$ is m_G, the maximal amplitude of the corresponding shape function is $\hat{w}_i$ and its maximal spatial derivative $\hat{w}'_j$ is given by $\hat{w}'_j = \nabla \hat{w}_j \cdot \mathbf{e}_\varphi$ with $\mathbf{e}_\varphi$ being the direction of the relative velocity between brake disc and pad. The factor 2π in Eq. (2.17) result from the integration of the entries of the matrix of circulatory terms over one period for the stability analysis using FLOQUET theory, see Eq. (2.12). The same holds for Eq. (2.19). For a conservative estimate, the product $\hat{w}_i \hat{w}'_j$ can be assessed to be

$$\hat{w}_i \hat{w}'_j \leq 1, \tag{2.18}$$

since the shape functions are assumed to be normalized to an amplitude of 1. For practical applications, the position of double eigenfrequencies in the frequency band of consideration and thus also the position of instabilities is not known before a final design is fixed. It has to be taken into account that they can occur everywhere in the whole frequency band. Therefore, Δf is not evaluated for discrete frequencies f_j anymore but for the continuous frequency f. For a conservative estimate, the generalized mass can then be chosen to be the minimal generalized mass $m_G^{\min}$ of all eigenmodes in the audible frequency range. Here, the minimal generalized mass is assumed to be calculated with eigenvectors normalized to an amplitude of 1. It can either be gained from a simplified analytical or finite element model.

In reality, the damping of the brake system not only originates from material damping of the disc and the brake pads, but also from the friction in the joints and from the friction between brake pad and rotor. Thus, the damping matrix can be a dense matrix. Still, as has been explained at the end of the previous section, it is assumed here that the damping matrix, corresponding to the double eigenfrequency $f_i = f_j$, is diagonal with equal elements d. Also, if the common assumption of mass and/or stiffness proportional damping is made,

d is given by

$$d = 2\pi(\underbrace{4\pi^2\alpha_S f^2}_{\text{prop. to stiffness}} + \underbrace{\alpha_M}_{\text{prop. to mass}}), \tag{2.19}$$

with the parameters α_S and α_M, which makes it possible to adjust the damping of the brake rotor to measurements. If measurements for the brake disc, for which the estimation is performed, are not yet available, it should be possible to adjust the parameters α_S and α_M from measurements of similar brake systems. It will be shown in the next section that the presented assumptions for the damping cover the most important effects considering its influence on the stability.

A combination of the approximations of n and d in Eq. (2.16) leads to a conservative estimate of the minimal necessary distance between the eigenfrequencies of the rotor given by

$$\Delta f \geq \frac{1}{\sqrt{2}\pi} \sqrt[4]{\frac{h^2k^2\mu^2}{r_p^2(m_G^{\min})^2} - 4\pi^2(4\pi^2\alpha_S f^2 + \alpha_M)^2 f^2}, \tag{2.20}$$

which is a function of the geometry and material parameters of the brake rotor, the damping, the pad stiffness and the considered frequency (the positions of double eigenfrequencies of the brake disc are not known a priori). If the distance is larger than the estimated limit calculated by Eq. (2.20), stability is ensured and squeal does not occur, while squeal may occur (but does not necessarily have to) if the distance is smaller. At low frequencies, the stabilizing effect of damping d is lacking and thus the maximum separation between the eigenfrequencies is necessary, while at higher frequencies the effect of damping is more pronounced and lowers the necessary separation of them. Two extremes can be formulated. The first being at lowest frequencies, where Δf has to be

$$\Delta f \geq \frac{1}{\sqrt{2}\pi} \sqrt{\frac{hk\mu}{r_p m_G^{\min}}}, \tag{2.21}$$

the second being the limit frequency $f_{\lim}$ above which squeal does not occur even without any separation of the eigenfrequencies due to damping of the

system. This frequency can be calculated by setting the right hand side of Eq. (2.20) to 0 leading to

$$\frac{h^2k^2\mu^2}{r_p^2(m_G^{\min})^2} - 4\pi^2(4\pi^2\alpha_S f_{\lim}^2 + \alpha_M)^2 f_{\lim}^2 = 0, \tag{2.22}$$

which can to be solved for the limit frequency $f_{\lim}$. This limit frequency above which squeal is not expected to occur is highly influenced by damping and therefore not easy to estimate, since damping can be difficult to measure.

In order to visualize these findings, four different types of brake discs are analyzed exemplarily with respect to the minimal necessary distance between the eigenfrequencies to avoid squeal and with respect to the maximum frequency they are expected to squeal without separation of the eigenfrequencies. Table 2.1 shows the parameters of the four types of brake discs. The first one

Disc	h [m]	r_p [m]	k [N/m]	μ [-]	$m_G^{\min}$ [kg]	α_S [s]	α_M [1/s]
P	0.026	0.125	$1.1 \cdot 10^6$	0.4	1.81	$2 \cdot 10^{-10}$	0.184
C	0.04	0.17	$2.2 \cdot 10^6$	0.5	2.0	$2 \cdot 10^{-10}$	0.184
I	0.012	0.12	$5.5 \cdot 10^5$	0.4	0.51	$1 \cdot 10^{-9}$	0.921
B	0.002	0.0735	$1.2 \cdot 10^5$	0.4	0.035	$1 \cdot 10^{-10}$	0.092

Table 2.1: Parameters of the four types of considered brake discs. Prototype brake disc (P), ceramic disc (C), cast iron rotor (I) and bicycle disc (B).

represents a steel prototype disc used for tests at the brake test rig at TU Darmstadt, of which the results of an optimization are presented in section 4.2, the three others represent exemplarily different types of state-of-the-art brake discs. The first one of those is a disc with the parameters of a ceramic brake disc with cooling channels used for expensive modern sports cars. The second one is a smaller cast iron disc without cooling channels which can typically be found at the rear axle of modern passenger cars with a much higher damping, and the third type is a bicycle brake disc which is much smaller, lighter and thinner than automotive brake discs. This bicycle brake disc was also optimized and tested, see section 4.5. Figure 2.3 shows the border between stable and unstable region of the prototype steel disc in frictional

contact calculated with Eq. (2.20). If the separation of any eigenfrequency

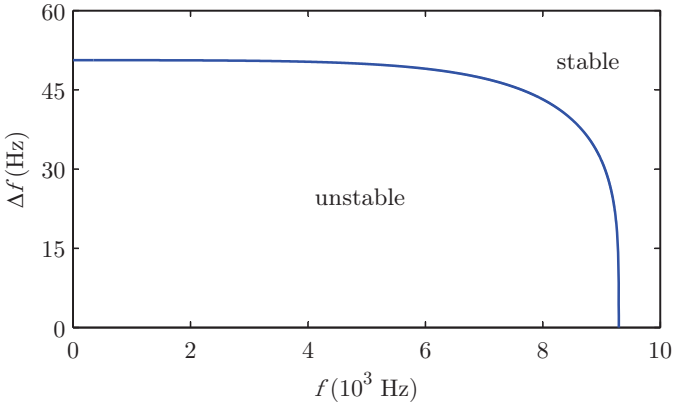

Figure 2.3: Minimal necessary separation of eigenfrequencies Δf for the prototype disc. The stable and unstable regions are marked in the figure.

pair of a brake disc under consideration lies inside the limit curve given by an equality sign in Eq. (2.20), the brake disc is potentially unstable. It can squeal, but does not necessarily have to. If the separation of all eigenfrequencies is above the bound, stability is ensured and no squeal can occur, which visualizes the goal of a defined split of eigenfrequencies in a estimated frequency band to avoid squeal. This directly relates to the definition of modal asymmetry (Def. 1) and of the grade of modal asymmetry (Def. 2) in section 2.2.1. It can be seen in Fig. 2.3 that for a large frequency band, a separation of eigenfrequencies is necessary for the stabilization of the system which is near the maximum value necessary at the lowest considered frequency, which is calculated with Eq. (2.21) to be approximately 50 Hz. Only at very high frequencies the effect of damping reduces the necessary separation until no separation of eigenfrequencies is necessary anymore to avoid squeal. Above this limit frequency of approximately 9300 Hz, even a modal symmetric steel disc is not expected to squeal. Figure 2.4 shows a comparison between the minimal necessary separation of eigenfrequencies of the four brake discs presented in Tab. 2.1. In comparison to the steel prototype disc, the ceramic

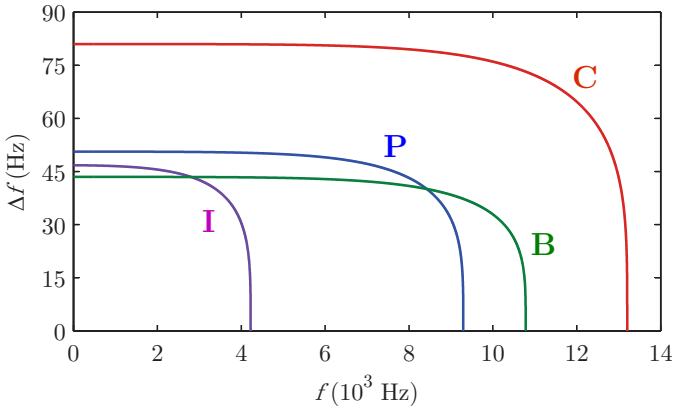

Figure 2.4: Comparison of the minimal necessary separation of eigenfrequencies Δf for the four considered types of brake discs. Prototype brake disc (P), ceramic disc (C), cast iron disc (I), bicycle disc (B).

brake disc requires a much higher separation of eigenfrequencies for squeal avoidance and also shows affinity for brake squeal up to much higher frequencies. This partially originates from a stiffer brake pad and a higher friction coefficient between brake pad and disc, partially from a different geometry. In contrast, the much thinner cast iron brake disc, which is in contact with a brake pad of lower stiffness and has a higher damping, shows reduced affinity to squeal. This corresponds to the practical experience that less stiff brake pads and higher damping frequently lead to brake systems less susceptible to squeal. In contrast to first intuition, the bicycle brake disc, which is a totally different kind of brake disc as is shown in Fig. 4.18, lies in the same range of frequency split and squeal limit frequency as the other three types of brake discs. The necessary separation of eigenfrequencies Δf and the limit frequencies f_{lim} for the four types of analyzed brake discs are given in Tab. 2.2. Some important conclusions can be drawn for the structural optimization of brake discs that will be presented in the following chapters. The first is that it is not necessary to optimize in the whole audible frequency range up to 20 kHz but only up to a smaller limit frequency that can be estimated in advance if

	P	C	I	B
Δf (Hz)	50	81	47	43
f_{lim} (Hz)	9300	13200	4200	10800

Table 2.2: Necessary separation of eigenfrequencies Δf and limit frequencies f_{lim} for the four types of analyzed brake discs rounded to 1 Hz and 100 Hz, respectively. Prototype brake disc (P), ceramic disc (C), cast iron disc (I) and bicycle disc (B).

some basic parameters of the brake system are known. This largely reduces the amount of eigenfrequencies to be considered and therefore enables a more efficient optimization process. Also, it is important to optimize the absolute distance between the eigenfrequencies instead of the relative one, since a higher separation between the eigenfrequencies is necessary at low frequencies. At first glance, both would seem to be reasonable. In the next section, the influence of the gyroscopic terms and of the structure of the damping matrix is analyzed, which have been neglected so far. These influences will be studied considering the example of the steel prototype disc.

2.2.4 Influence of gyroscopic terms and of the structure of the damping matrix

It is well known that gyroscopic terms can influence the stability of the steady-sliding-state condition of the brake system, despite the fact that they are small in the low range of rotational speeds important for the analysis of brake squeal [43, 109, 112]. In Fig. 2.5, the stability boundary is shown for three values of g, which is calculated numerically with Eq. (2.14) using the estimates for the circulatory terms n and d presented in Eqs. (2.17) and (2.19), respectively. The terms Δd and $\widetilde{d}$ are set equal to zero. The first stability bound for $g = 0$ is already known from Figs. 2.3 and 2.4. For the other two cases, the values of g are chosen to be in the same range as the damping terms d evaluated at a frequency of 1 kHz, which is known to be the lower bound of squealing frequencies for automotive brake discs [60]. The first one of these cases is calculated with a gyroscopic term of $g = d(f = 1000\,\text{Hz})/5$ and the

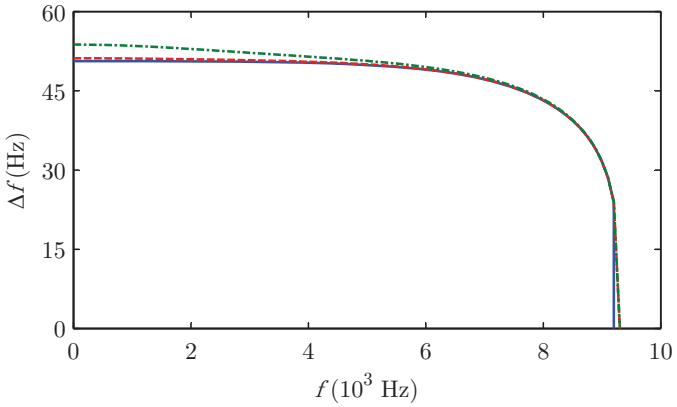

Figure 2.5: Minimal necessary separation of eigenfrequencies Δf for the prototype disc for $g = 0$ (solid, blue), $g = d(f = 1000\,\mathrm{Hz})/5$ (dashed, red) and $g = d(f = 1000\,\mathrm{Hz})/2$ (dash-dotted, green).

second one for $g = d(f = 1000\,\mathrm{Hz})/2$. The gyroscopic terms have two effects. They enlarge the range in which the brake system is susceptible to squeal and they increase the split of eigenfrequencies necessary to avoid squeal at low frequencies. However, both effects are small and thus it seems to be reasonable to neglect the gyroscopic terms for the further analysis as long as they are indeed "small". The gyroscopic terms increase with increasing rotational speed of the brake rotor as also will their influence on the stability boundary, but the squeal relevant range is at very low speeds leading to "small" gyroscopic terms.

While it is well known that gyroscopic terms can have unwanted effects in conjunction with circulatory terms, less is known about the influence of the structure of the damping matrix. The influence of Δd and $\widetilde{d}$ is studied in direct analogy to the influence of gyroscopic terms g; the parameters g and Δd or $\widetilde{d}$, respectively, are set equal to 0. For the first numerical study, Δd is set to $\Delta d = 0.3\,d$ and $\Delta d = 2\,d$ leading to the resulting stability boundaries presented in Fig. 2.6, a). It can seen that Δd has a destabilizing effect at low frequencies, which has to be compensated by a higher split of eigenfrequencies.

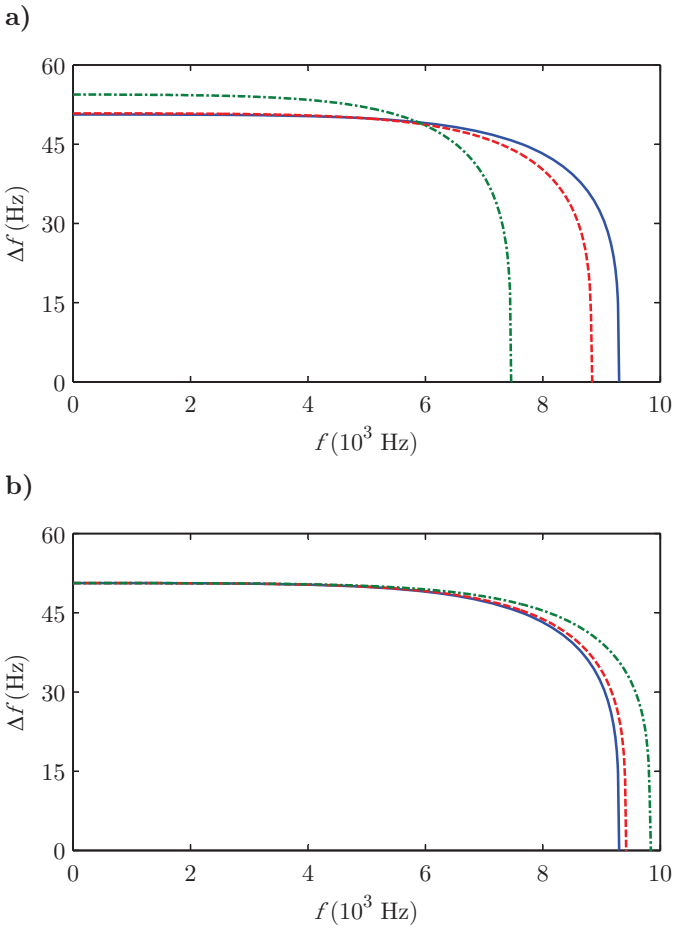

Figure 2.6: a) Minimal necessary separation of eigenfrequencies Δf for the prototype disc for $\Delta d = 0$ (solid, blue), $\Delta d = 0.3\,d$ (dashed, red) and $\Delta d = 2d$ (dash-dotted, green). b) Minimal necessary separation of eigenfrequencies Δf for the prototype disc for $\widetilde{d} = 0$ (solid, blue), $\widetilde{d} = 0.25\,d$ (dashed, red) and $\widetilde{d} = 0.5\,d$ (dash-dotted, green).

At higher frequencies, the effect is positive instead, since the limit frequency up to which squeal is possible is reduced. However, both effects are small and a very high difference of the damping terms on the diagonal of the damping

matrix[5] is required to change the stability behavior significantly. Also, if the idea of stiffness proportional damping is implemented rigorously, Δd can only have values far below $0.3\,d$, since Δf is only a very low percentage of f.

The influence of the off-diagonal terms $\widetilde{d}$ is shown in Fig. 2.6, b). For the calculation of these results, $\widetilde{d}$ has been chosen as $\widetilde{d} = 0.25\,d$ and $\widetilde{d} = 0.5\,d$. It can be seen that higher values of $\widetilde{d}$ lead to higher limit frequencies (up to which squeal is possible). The off-diagonal terms of the damping matrix therefore compensate the positive effect of the diagonal terms to a certain degree. In the limit of a positive semi-definite damping matrix with $\widetilde{d} = d$, it completely cancels the effect of d. However, even the presence of large values of $\widetilde{d}$ does not destabilize the steady-sliding-state, if a sufficient split between the eigenfrequencies is achieved. Also, the damping matrix will be diagonal-dominant in most cases after the transformation that diagonalizes $\overline{\mathbf{K}}(t)$ and therefore the influence of $\widetilde{d}$ will be negligible.

Numerical studies with an equivalent 2x2 **M-D-G-K-N**-system with constant coefficients (Eq. (2.1)) show the same tendencies. If the assumption of "small" gyroscopic, circulatory and damping terms is dropped, this can change and a difference of the diagonal terms of the damping matrix and the presence of the off-diagonal ones can lead to instability. However, since for the brake systems discussed in this thesis the mentioned assumption is valid, as will be shown by the results presented in chapter 4, this shall not be discussed further here.

After this short analysis of the importance of gyroscopic terms and of the structure of the damping matrix, in the next section a procedure for the design of asymmetric brake discs will be presented to achieve squeal free brake discs. This lays the basis for the structural optimization presented in later chapters and helps to classify it in the context of the design of brake discs for practical applications.

[5] Here, this reference is made to the damping matrix of the 2x2-system of Eq. (2.11).

2.3 Procedure for the design of asymmetric, squeal-free discs

If modal asymmetric brake discs are to be used in practical applications, it is necessary to account for the asymmetric design in a very early design stage. This is especially important for the automotive industry, since changes of the rotor design in later design stages will require expensive revisions, e.g. of the casting molds for cast iron discs. In the following, an overview of a possible workflow for the design of asymmetric discs with the focus on squeal avoidance is presented.

Workflow for the design of asymmetric brake discs

1. Starting point
   - Definition of the design space of the rotor: thickness, inner and outer radius and, if present, dimensions of the hat.
   - Determination of the material to be used, e.g. cast iron or steel.
   - Estimation of the coefficient of friction between brake pad and brake disc, the pad overall stiffness and the overall damping
2. Formulation of design criteria for squeal free asymmetric discs
   - Minimal necessary split of eigenfrequencies for squeal avoidance
   - Frequency range in which squeal is possible
3. Choice of geometry variations to fulfill design criteria, e.g. variation of the cooling channels
4. Structural optimization of the disc
   - Formulation of a useful objective function
   - Consideration of constraints (reaching from balance requirements to manufacturing demands)
5. Realization of the final design under possible consideration of other design criteria

In the first stage, basic parameters of the brake disc are known or can be determined either from requirements of the practical application or knowledge from similar brake discs already in use. Before the final design is fixed, goals for the structural optimization of the brake disc for squeal avoidance can be deduced. In order to achieve those in the final design, geometry variations are chosen to fulfill these criteria. These can reach from very simple modifications, like the application of small single masses, to more realistic modifications of the cooling channels. Based on a proper model, which will be a FE model due to the complicated geometry of the brake rotor in practical applications, a structural optimization can be conducted to achieve a final design robust against brake squeal. However, it is obvious that for a final design of a realistic brake disc, there are many objectives to take into account. The basic function of the brake disc has to be fulfilled in first place, then, thermal deformation, wear resistance, manufacturing issues, costs etc. have to be considered. These objectives are all important but frequently conflicting. As one example, from a squeal free point of view, it would be very beneficial to manufacture brake pads with a small stiffness and a low friction coefficient between brake pad and disc. However, for automotive applications a brake pad with high stiffness and high friction coefficient is required to allow the customer to have a better "feeling" for the brake application and to realize short stopping distances of the vehicle. In this thesis, the focus lies on the avoidance of brake squeal, the other mentioned requirements are not taken into account directly. This might not seem to be satisfying at first glance, however, the intention of this thesis is not to achieve brake disc designs directly suitable for usage in a passenger car or for a bicycle, but to show the possibilities and limits of squeal avoidance by the design and optimization of brake rotors. Before the structural optimization is introduced in detail in chapter 4, the modeling of brake discs used in the optimization is presented in the next chapter.

3 Efficient modeling of brake discs

This chapter presents a modeling technique for brake discs with modifications that can range from the insertion of radial or axial holes to the incorporation of cooling channels. It gives an efficient basis for a structural optimization that aims for a change in the distribution of eigenfrequencies, as will be presented in the next chapter, and allows for large changes in the geometry of the structure to be optimized. For a shorter and easier notation, this modeling approach is referred to as energy modification method (EMM) throughout this thesis. After the derivation of the method in section 3.1, the EMM will be used to study the free vibration problem of two simple examples, an inhomogeneous rod and a rectangular plate with a hole. The former example gives a first insight into advantages and limits of the approach, the latter will be used to study the convergence of the EMM in detail. The method will then be applied to model an automotive brake rotor with radial holes, a brake disc with cooling ribs defining the cooling channels of a realistic automotive brake disc and to a simple example of a bicycle brake rotor. Large parts of this chapter have been published first in [126].

3.1 A suitable modeling approach for an efficient structural optimization

The structural optimization problem to split all eigenfrequencies of a brake rotor in a specified frequency range is a nonlinear optimization problem requiring very high computational effort due to the fact that in each optimization step the eigenvalue problem has to be solved. It will be shown in chapter 4.2 that satisfying results can only be achieved if large variations in the geometry are possible. Therefore, the underlying modeling technique has to allow for

these large changes as efficiently as possible. Additionally, the geometry of the brake disc can be complicated due to the presence of hat, holes or cooling channels, which prevents the usage of semianalytical modeling techniques with a discretization with global shape functions but encourages the usage of the FEM with local shape functions. The EMM to be introduced and derived in the following has the required properties and avoids the necessity to remesh the structure in the optimization process that is often necessary if the structure to be optimized is modeled with the FEM.

3.1.1 Basic concept

In their 2007 publication, Kwak and Han presented an approach to model plates with holes, where the holes are treated as parts with negative material parameters [63]. The main idea of this modeling technique is to discretize a plate and a hole separately, using a Ritz approach with global shape functions and to combine them by kinematical constraints leading to mass and stiffness matrices and thus eigenfrequencies of the combined structure. The benefit of this method is that due to the separate discretization of plate and hole the position of the hole can be varied without changing the underlying discretization itself. In the method discussed in the following, the approach of Kwak and Han is generalized, modified and combined with the FEM. The basic idea is in direct analogy to [63] to discretize the basis structure, e.g. a plate or a brake disc, and the modifications, e.g. the holes or cooling ribs, separately and then to combine modifications and basis structure in the energy expressions, which can also account for geometrical nonlinearities in the approach presented here. If holes are considered, they are treated as parts with vanishing stiffness and mass density, so that the modification of the basis structure corresponds to a subsystem with negative stiffness and mass. Finally, the coordinates of the modifications are expressed in terms of the coordinates of the basis structure and thus the mass and stiffness matrices of the completely assembled system are obtained. For the discretization, the use of the FEM based on local shape functions is encouraged, since it allows the discretization of complex strucutures, is a very flexible method and is readily available in

commercial tools. Despite the fact that the EMM has been designed to allow a structural optimization of brake discs with various modifications to adjust the disc's eigenfrequency distribution, it can be applied to a large variety of problems, as long as it is not the aim to represent very localized effects, like stress distributions at cracks in a structure.

If holes or cut-outs are to be modeled, the core idea of the EMM is to use negative mass and stiffness parameters. This is already known in the scientific community in the context of asymptotic modeling of constraints [50, 52, 54]. The approach to utilize negative stiffness and inertia terms in asymptotic modeling can not only be applied to vibrational problems, but also to a stability analysis [51]. Furthermore, detailed studies about convergence are available [53]. However, this is not the case for using negative terms for modeling modifications, thus a detailed convergence study will be presented in section 3.3.2 of this chapter. The combination of parts of the model with positive and negative material parameters is also known in the context of hybrid modeling, where parts of the model are experimentally measured and parts are modeled analytically or numerically. Frequently, a combination of experimentally measured substructures and analytical or numerical substructures in one combined model is advantageous. The analytical or numerical substructures can have negative material parameters [5, 75].

It is also interesting to note that the coupling of the coordinates of modification and basis structure in the EMM is related to common mesh coupling methods, which address challenges reaching from the coupling of different (FEM) element types [19] to coupling of different physical domains (e.g. fluid-structure interaction) [23].

3.1.2 Mathematical derivation

In the following, a detailed mathematical derivation of the approach will be presented starting from basic equations of elasticity. Consider an elastic body D with its boundary ∂D, density ρ and a material law with linear stress-strain relationships shown in Fig. 3.1. A domain H inside the elastic body D (H $\subset$ D) with the boundary ∂H, density $\rho + \overline{\rho}$ and other different material parameters

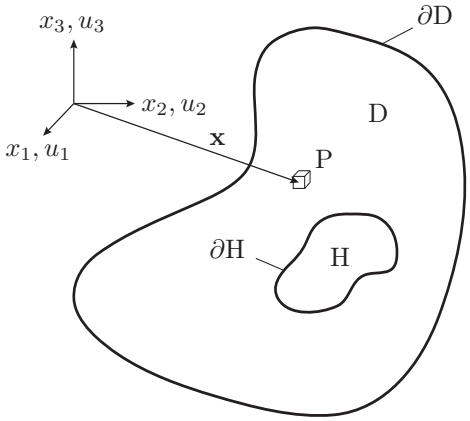

Figure 3.1: Elastic body D with a modification H.

makes the body inhomogeneous. The kinetic energy of the body is then given by

$$T = \frac{1}{2}\int_{\mathrm{D}} \rho(\mathbf{x})\dot{\mathbf{p}}(\mathbf{x},t)\cdot\dot{\mathbf{p}}(\mathbf{x},t)\mathrm{d}V, \tag{3.1}$$

where the vector of displacements $\mathbf{p}$ of a material point P of the body reads

$$\mathbf{p}(\mathbf{x},t) = u_1(\mathbf{x},t)\mathbf{e}_1 + u_2(\mathbf{x},t)\mathbf{e}_2 + u_3(\mathbf{x},t)\mathbf{e}_3, \tag{3.2}$$

with the displacement in x_1-direction u_1, in x_2-direction u_2, in x_3-direction u_3 and the unity vectors $\mathbf{e}_1$, $\mathbf{e}_2$ and $\mathbf{e}_3$. The vector $\mathbf{x}$ denotes the position of a material point inside the body. The potential energy can be written as

$$U = \frac{1}{2}\int_{\mathrm{D}} \boldsymbol{\sigma}(\boldsymbol{\epsilon}) : \boldsymbol{\epsilon}\mathrm{d}V = \frac{1}{2}\int_{\mathrm{D}} \sigma_{ij}\epsilon_{ij}\mathrm{d}V \tag{3.3}$$

using the summation convention, where $\boldsymbol{\sigma}(\boldsymbol{\epsilon})$ is the stress tensor depending on the Green-Lagrange strain tensor $\boldsymbol{\epsilon}$, which are both tensors of second order (with their components σ_{ij} and ϵ_{ij}). The components of the strain tensor $\boldsymbol{\epsilon}$ are related to the displacements u_i of a material point in the finite strain case by

$$\epsilon_{ij} = \frac{1}{2}\left(\frac{\partial u_i}{\partial x_j} + \frac{\partial u_j}{\partial x_i} + \frac{\partial u_k}{\partial x_i}\frac{\partial u_k}{\partial x_j}\right), \tag{3.4}$$

where $i, j, k = 1, 2, 3$ and the summation convention is also used. As the most common material law, HOOKE's law can be used to express the components of the stress tensor $\boldsymbol{\sigma}$ in terms of the components of the strain tensor $\boldsymbol{\epsilon}$ as

$$\sigma_{ij} = c_{ijkl}\epsilon_{kl}, \tag{3.5}$$

in which the summation convention is used again to shorten the occurring expressions [12]. c_{ijkl} are the components of a tensor $\mathbf{C}$ of fourth order containing the material constants, where $\mathbf{C} = \mathbf{C}(\mathbf{x})$ here. Inserting HOOKE's law into the potential energy and considering the different tensors containing the material constants in the domains D\H with the material constants $\mathbf{C}$ and H with $\mathbf{C} + \overline{\mathbf{C}}$ results in

$$U = \underbrace{\frac{1}{2}\int_{\mathrm{D}} (\mathbf{C} : \boldsymbol{\epsilon}) : \boldsymbol{\epsilon} \mathrm{d}V}_{\mathrm{I}} + \underbrace{\frac{1}{2}\int_{\mathrm{H}} \left(\overline{\mathbf{C}} : \boldsymbol{\epsilon}\right) : \boldsymbol{\epsilon} \mathrm{d}V}_{\mathrm{II}}. \tag{3.6}$$

Similarly, the kinetic energy (3.1) can be written as

$$T = \underbrace{\frac{1}{2}\int_{\mathrm{D}} \rho \dot{\mathbf{p}}(\mathbf{x}, t) \cdot \dot{\mathbf{p}}(\mathbf{x}, t) \mathrm{d}V}_{\mathrm{I}} + \underbrace{\frac{1}{2}\int_{\mathrm{H}} \overline{\rho} \dot{\mathbf{p}}(\mathbf{x}, t) \cdot \dot{\mathbf{p}}(\mathbf{x}, t) \mathrm{d}V}_{\mathrm{II}}. \tag{3.7}$$

It is well known that for isotropic material behavior, the material constants c_{ijkl} can be expressed by two independent material constants [12], e.g. the modulus of elasticity E and POISSON's ratio ν leading to

$$\sigma_{ij} = \frac{\nu E}{(1+\nu)(1-2\nu)}\epsilon_{kk}\delta_{ij} + \frac{E}{1+\nu}\epsilon_{ij}, \tag{3.8}$$

making use of δ_{ij} as the well known KRONECKER-Delta. In the case considered here, the modulus of elasticity in the domain D\H is E and in the domain H $E + \overline{E}$. The expression for the potential energy (3.6) simplifies accordingly.

The discretized equations of motion for the system can be obtained using the RITZ method, where the basic idea of the EMM is to use separate discretization schemes for the domains I (denoted as basis structure) and II (representing the modification) in the RITZ approximation of the system and

later to combine them. The ansatz for the displacement in domain I is

$$\begin{pmatrix} u_1(\mathbf{x},t) \\ u_2(\mathbf{x},t) \\ u_3(\mathbf{x},t) \end{pmatrix} = \begin{pmatrix} \sum_i U_i(\mathbf{x}) q_i^u(t) \\ \sum_i V_i(\mathbf{x}) q_i^v(t) \\ \sum_i W_i(\mathbf{x}) q_i^w(t) \end{pmatrix} = \begin{pmatrix} \mathbf{U}^{\mathrm{T}}(\mathbf{x})\mathbf{q}^u(t) \\ \mathbf{V}^{\mathrm{T}}(\mathbf{x})\mathbf{q}^v(t) \\ \mathbf{W}^{\mathrm{T}}(\mathbf{x})\mathbf{q}^w(t) \end{pmatrix}, \tag{3.9}$$

where the shape functions $U_i(\mathbf{x})$, $V_i(\mathbf{x})$ and $W_i(\mathbf{x})$ can be global or local shape functions fulfilling the essential boundary conditions. The ansatz for the displacement in domain II is

$$\begin{pmatrix} \overline{u}_1(\mathbf{x},t) \\ \overline{u}_2(\mathbf{x},t) \\ \overline{u}_3(\mathbf{x},t) \end{pmatrix} = \begin{pmatrix} \sum_j \overline{U}_j(\mathbf{x}) \overline{q}_j^u(t) \\ \sum_j \overline{V}_j(\mathbf{x}) \overline{q}_j^v(t) \\ \sum_j \overline{W}_j(\mathbf{x}) \overline{q}_j^w(t) \end{pmatrix} = \begin{pmatrix} \overline{\mathbf{U}}^{\mathrm{T}}(\mathbf{x})\overline{\mathbf{q}}^u(t) \\ \overline{\mathbf{V}}^{\mathrm{T}}(\mathbf{x})\overline{\mathbf{q}}^v(t) \\ \overline{\mathbf{W}}^{\mathrm{T}}(\mathbf{x})\overline{\mathbf{q}}^w(t) \end{pmatrix}, \tag{3.10}$$

respectively. The separate discretization schemes for I and II are combined by the condition

$$\begin{pmatrix} \overline{u}_1(\mathbf{x},t) \\ \overline{u}_2(\mathbf{x},t) \\ \overline{u}_3(\mathbf{x},t) \end{pmatrix} = \begin{pmatrix} u_1(\mathbf{x},t) \\ u_2(\mathbf{x},t) \\ u_3(\mathbf{x},t) \end{pmatrix}, \quad \text{for } \mathbf{x} \in H. \tag{3.11}$$

In the discretized case, this condition reduces to

$$\begin{pmatrix} \overline{\mathbf{U}}^{\mathrm{T}}(\mathbf{x})\overline{\mathbf{q}}^u(t) \\ \overline{\mathbf{V}}^{\mathrm{T}}(\mathbf{x})\overline{\mathbf{q}}^v(t) \\ \overline{\mathbf{W}}^{\mathrm{T}}(\mathbf{x})\overline{\mathbf{q}}^w(t) \end{pmatrix} = \begin{pmatrix} \mathbf{U}^{\mathrm{T}}(\mathbf{x})\mathbf{q}^u(t) \\ \mathbf{V}^{\mathrm{T}}(\mathbf{x})\mathbf{q}^v(t) \\ \mathbf{W}^{\mathrm{T}}(\mathbf{x})\mathbf{q}^w(t) \end{pmatrix}, \quad \text{for } \mathbf{x} \in H, \tag{3.12}$$

which cannot be fulfilled in a strong sense with a limited number of shape functions. But it can be fulfilled in a weak, error minimizing sense, either in an integral sense, as has been done by Kwak et al. [63], or by fulfilling the condition at χ discrete points. This seems to be advantageous if local shape functions are used, here shown for the x_3-direction:

$$\begin{aligned} \overline{\mathbf{W}}^{\mathrm{T}}(\mathbf{x}_1)\overline{\mathbf{q}}^w &= \mathbf{W}^{\mathrm{T}}(\mathbf{x}_1)\mathbf{q}^w \\ &\vdots \\ \overline{\mathbf{W}}^{\mathrm{T}}(\mathbf{x}_\chi)\overline{\mathbf{q}}^w &= \mathbf{W}^{\mathrm{T}}(\mathbf{x}_\chi)\mathbf{q}^w \end{aligned} \tag{3.13}$$

This leads to a system of equations

$$\overline{\mathbf{S}}\overline{\mathbf{q}} = \mathbf{S}\mathbf{q}, \tag{3.14}$$

relating the coordinates of the modification $\overline{\mathbf{q}} = (\overline{\mathbf{q}}^u, \overline{\mathbf{q}}^v, \overline{\mathbf{q}}^w)^{\mathrm{T}}$ to the coordinates of the basis structure $\mathbf{q} = (\mathbf{q}^u, \mathbf{q}^v, \mathbf{q}^w)^{\mathrm{T}}$. The matrix $\overline{\mathbf{S}}$ is given by

$$\overline{\mathbf{S}} = \begin{bmatrix} \left[\overline{U}_j(\mathbf{x}_i)\right] & 0 & 0 \\ 0 & \left[\overline{V}_j(\mathbf{x}_i)\right] & 0 \\ 0 & 0 & \left[\overline{W}_j(\mathbf{x}_i)\right] \end{bmatrix}, \tag{3.15}$$

while the matrix $\mathbf{S}$ can be written as

$$\mathbf{S} = \begin{bmatrix} \left[U_j(\mathbf{x}_i)\right] & 0 & 0 \\ 0 & \left[V_j(\mathbf{x}_i)\right] & 0 \\ 0 & 0 & \left[W_j(\mathbf{x}_i)\right] \end{bmatrix}. \tag{3.16}$$

The entries of these matrices are given by the shape functions evaluated at the mentioned χ discrete points. In order to guarantee the solvability of Eq. (3.14), the χ points, where the displacements in the modification (II) are set to be identical to selected points in the basis structure (I), are chosen to be the nodes of local, normed shape functions. Then the matrix $\overline{\mathbf{S}}$ becomes the identity matrix and Eq. (3.14) simplifies to

$$\overline{\mathbf{q}} = \mathbf{S}\mathbf{q}. \tag{3.17}$$

After this substitution of the displacement in domain II by the displacement of domain I, the resulting ansatz for the displacement of the modified body can be inserted into the kinetic energy (3.7) and the potential energy (3.6) after taking proper derivatives, if necessary (see Eq. (3.4)). The discretized kinetic energy of the structure with modification then reads

$$T = \frac{1}{2}\dot{\mathbf{q}}^{\mathrm{T}}\mathbf{M}\dot{\mathbf{q}} + \frac{1}{2}\dot{\mathbf{q}}^{\mathrm{T}}\mathbf{S}^{\mathrm{T}}\overline{\mathbf{M}}\mathbf{S}\dot{\mathbf{q}}, \tag{3.18}$$

where $\mathbf{M}$ is the mass matrix of the discretized basis structure (I) and $\overline{\mathbf{M}}$ is the mass matrix of the modification (II). The discretized potential energy becomes

$$U = \frac{1}{2}\mathbf{q}^{\mathrm{T}}\mathbf{K}\mathbf{q} + \frac{1}{2}\mathbf{q}^{\mathrm{T}}\mathbf{S}^{\mathrm{T}}\overline{\mathbf{K}}\mathbf{S}\mathbf{q} + \mathcal{O}(\mathbf{q}^2), \tag{3.19}$$

with the stiffness matrix of the basis structure $\mathbf{K}$ in domain I, the stiffness matrix of the modification $\overline{\mathbf{K}}$ in domain II and higher order terms. These discretized energy expressions can be inserted into LAGRANGE's equations to derive the equations of motion of the system, which are nonlinear in the case of finite strains. In the linear case presented in the following, this is straightforward since the energy expressions of the linear system directly yield mass and stiffness matrices. In the special case of small strains, the entries of the GREEN-LAGRANGE strain tensor $\boldsymbol{\epsilon}$ simplify to

$$\epsilon_{ij} = \frac{1}{2}\left(\frac{\partial u_i}{\partial x_j} + \frac{\partial u_j}{\partial x_i}\right), \tag{3.20}$$

leading to a discretized potential energy given by

$$U = \frac{1}{2}\mathbf{q}^{\mathrm{T}}\mathbf{K}\mathbf{q} + \frac{1}{2}\mathbf{q}^{\mathrm{T}}\mathbf{S}^{\mathrm{T}}\overline{\mathbf{K}}\mathbf{S}\mathbf{q}. \tag{3.21}$$

Mass and stiffness matrices of basis structure and modification can be calculated using the RITZ method with global shape functions or by using FEM tools. Obtained from these energy expressions, the mass matrix $\mathbf{M}_c$ and the stiffness matrix $\mathbf{K}_c$ of the system with one modification read

$$\mathbf{M}_c = \mathbf{M} + \mathbf{S}^{\mathrm{T}}\overline{\mathbf{M}}\mathbf{S}, \tag{3.22a}$$

$$\mathbf{K}_c = \mathbf{K} + \mathbf{S}^{\mathrm{T}}\overline{\mathbf{K}}\mathbf{S}. \tag{3.22b}$$

It is also possible to consider N modifications leading to

$$\mathbf{M}_c = \mathbf{M} + \sum_{n=1}^{N} \mathbf{S}_n^{\mathrm{T}}\overline{\mathbf{M}}\mathbf{S}_n \tag{3.23}$$

and

$$\mathbf{K}_c = \mathbf{K} + \sum_{n=1}^{N} \mathbf{S}_n^{\mathrm{T}}\overline{\mathbf{K}}\mathbf{S}_n, \tag{3.24}$$

with the coordinate coupling matrix $\mathbf{S}_n$ of each modification. These steps illustrate the assembly of mass and stiffness matrices of structures with modifications using the EMM. The resulting matrices can then be used for further

calculations, in this thesis for the calculation of eigenfrequencies ω and eigenvectors $\mathbf{v}$. The corresponding eigenvalue problem can be written as

$$\left(\mathbf{K}_c - \mathbf{M}_c\omega^2\right)\mathbf{v} = \mathbf{0}. \tag{3.25}$$

In order to complete the explanation of the EMM and to introduce holes or clearances in the basis structure, it is possible to set the density of the modifications as $\overline{\rho} = -\rho$ and the modulus of elasticity (or another stiffness parameter) to $\overline{E} = -E$. Then the mass matrix and stiffness matrix of the modifications become negative and the effect of the hole or clearance is embedded in the mass and stiffness matrices $\mathbf{M}_c$ and $\mathbf{K}_c$ accordingly. The addition of the mass matrices of the modifications to the mass matrix of the basis structure might lead to a mass matrix $\mathbf{M}_c$ that loses its positive definiteness possibly yielding numerical difficulties. In order to avoid this, it is proposed to calculate the mass matrix of the structure with holes or clearances as

$$\mathbf{M}_c = \mathbf{M} + (1-\kappa)\sum_{n=1}^{N} \mathbf{S}_n^{\mathrm{T}}\overline{\mathbf{M}}\mathbf{S}_n, \tag{3.26}$$

with a small parameter $\kappa \ll 1$. In the next section, as a first, simple example, the EMM will be used to study the free longitudinal vibrations of an inhomogeneous rod.

3.2 Longitudinal vibrations of an inhomogeneous rod

This example of a linear-elastic rod with density ρ, area A and modulus of elasticity E has also been studied in [114]. Between $x = L_1$ and $x = L_2$, the density is $\rho + \overline{\rho}$ and the modulus of elasticity is $E + \overline{E}$, as is shown in Fig. 3.2, making the rod inhomogeneous. The homogeneous bar as the basis structure can be discretized with global shape functions

$$U_i^{\mathrm{glob}}(x) = \sin\left(\frac{(2i-1)\pi x}{2L}\right) \tag{3.27}$$

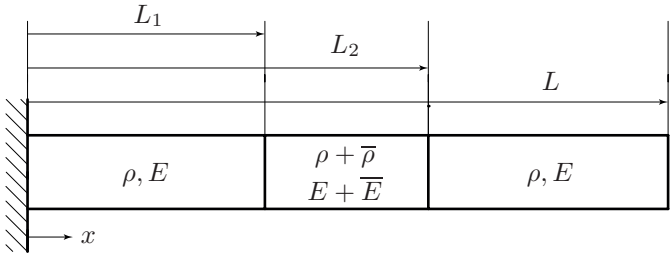

Figure 3.2: Inhomogeneous rod.

or local shape functions

$$U_i^{\mathrm{loc}}(x) = \begin{cases} 1 + \frac{x-ih}{h} & \text{for } (i-1)h \leq x \leq ih \\ -\frac{x-(i+1)h}{h}, & \text{for } ih \leq x \leq (i+1)h \\ 0, & \text{else.} \end{cases} \tag{3.28}$$

The modification between $x = L_1$ and $x = L_2$ with density $\overline{\rho}$ and modulus of elasticity $\overline{E}$ is discretized using only local shape functions $\overline{U}_j^{\mathrm{loc}}(x)$ defined in analogy to Eq. (3.28). The mass and stiffness matrices of basis structure and modification are then obtained with the EMM, where the entries s_{ij} of the coordinate coupling matrix $\mathbf{S}$ are given by Eq. (3.16), leading to the mass and stiffness matrices of the inhomogeneous bar obtained with Eqs. (3.22a) and (3.22b).

Using the parameters presented in Tab. 3.1, where $E + \overline{E} = 0.5E$, three

$\rho = 7850\,\mathrm{kg/m^3}$	$E = 206000\,\mathrm{MPa}$	$L = 1\,\mathrm{m}$	$L_2 = 0.65\,\mathrm{m}$
$\overline{\rho} = 0\,\mathrm{kg/m^3}$	$\overline{E} = -103000\,\mathrm{MPa}$	$L_1 = 0.4\,\mathrm{m}$	$\kappa = 0$

Table 3.1: Parameters of the rod.

numerical experiments are performed, in which the first five non-zero eigenfrequencies of the inhomogeneous rod are computed. In one calculation 12 global shape functions are used for the discretization of the homogeneous rod and

for the second calculation 80 local ones. The modification is approximated with 40 local shape functions in both cases. Table 3.2 shows that all results are in good agreement.

Performing the same calculation using $\overline{E} = -E$ reveals a very different re-

Eigenfrequency (rad/s)	Global shape f.	Local shape f.	Difference (%)
ω_1	7274	7229	0.62
ω_2	21625	21533	0.43
ω_3	37188	36921	0.72
ω_4	51544	51286	0.50
ω_5	65326	64753	0.88

Table 3.2: Eigenfrequencies of the bar for $E + \overline{E} = 0.5E$.

sult, as is demonstrated in Tab. 3.3.

The agreement between the approach with global shape functions and the

Eigenfrequency (rad/s)	Exact solution	Global shape f.	Local shape f.
ω_1	20117	6487	19938
ω_2	45981	24033	45535
ω_3	60350	33043	59863
ω_4	91962	52321	91208
ω_5	100580	70399	99927

Table 3.3: Eigenfrequencies of the bar for $E + \overline{E} = 0$.

exact solution is poor, while the agreement for the approach with local shape functions is very good. However, it has to be noted that the approximations do not yield an upper bound for the eigenfrequencies, as for a standard RITZ approach. This originates from a possible underestimation of the potential energy due to the presence of negative terms, depending on the discretization. A couple of approximately zero eigenvalues corresponding to the nodes in the perturbed area of the rod have been discarded in the table. The reason

for the poor agreement between the approach with global shape functions and the exact solution lies in the fact that for the case $\overline{E} = -E$ the left and the right part of the rod are not connected, whereas the global shape functions always couple both parts. Therefore, they can only poorly approximate discontinuities as they occur here with the placement of the hole between both parts of the rod. Concluding, local shape functions can cover local effects in most cases better than global ones and thus are recommended for a use with the approach presented here. In the next section, the EMM will be applied to a rectangular plate with one rectangular or circular hole.

3.3 Free vibrations of a rectangular plate with a rectangular or circular hole

Both cases have also been studied by Kwak et. al. [63] using a related approach based on global shape functions for plate and holes. Also, this example is widely studied in the literature using a variety of methods [17, 66, 69, 117, 137] and can therefore be considered as a benchmark problem. Here, the discretization is conducted with the FEM and thus local shape functions only, for reasons discussed in the previous section. However, the obtained results will be compared to the results presented in [63] in the next section and are in good agreement.

3.3.1 Modeling details

The plate with a rectangular hole is shown in Fig. 3.3, a) and the plate with circular hole in Fig. 3.3, b). The basis structure, here a plate, and the modification, in this case a rectangular or circular hole, are discretized using the FEM yielding the mass and stiffness matrices of the basis structure and the modification. The applicability of the EMM does not depend on the type of elements chosen for the discretization, however, the discretization will be conducted with 3D isoparametric elements with quadratic shape functions here. Their formulation can e.g. be found in [68] as well as the general formulation of mass and stiffness matrices for this type of elements. The calculation of

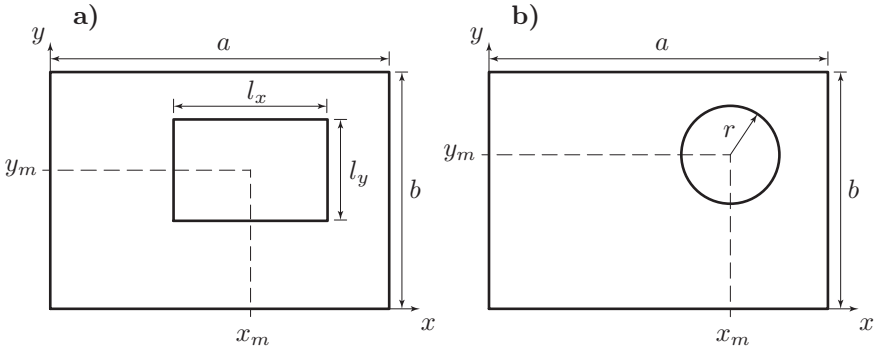

Figure 3.3: a) Rectangular plate with a rectangular hole. b) Rectangular plate with a circular hole.

mass and stiffness matrices of the plate with hole is then conducted using the approach described in section 3.1.2. Since local shape functions are used for the formulation of these elements, the entries of the coordinate coupling matrix $\mathbf{S}$ are given by local shape functions $U_j^{\text{loc}}(\xi_i, \eta_i, \tau_i)$, $V_j^{\text{loc}}(\xi_i, \eta_i, \tau_i)$ and $W_j^{\text{loc}}(\xi_i, \eta_i, \tau_i)$ evaluated at local element coordinates ξ_i in x-direction, η_i in y-direction and τ_i in z-direction (if a cartesian coordinate system is used). Thus for each node in the mesh of the modification it is necessary to determine the element in the mesh of the basis structure where the node is placed and to determine the local coordinates from the global position $\mathbf{x}_i$ of the node. In general, it could be an elaborate procedure to determine the element in which the modification's node is placed, e.g. if different kinds of elements were used in one mesh. However, for the rectangular plate presented here, a mesh is used which consists only of bricks with edge angles of 90^o shown in Fig. 3.4, a), which makes it very easy to determine the element belonging to the considered hole node at position $\mathbf{x}_i$. The second important point is to determine the local coordinates ξ_i, η_i and τ_i from the position $\mathbf{x}_i$ of the actual node. Depending on the choice of the element type used to mesh the body (e.g. plate elements), their shape and the local coordinate system used, this might require additional calculations. Nevertheless, the utilization of isoparametric elements, which use (local) shape functions not only to describe displacements

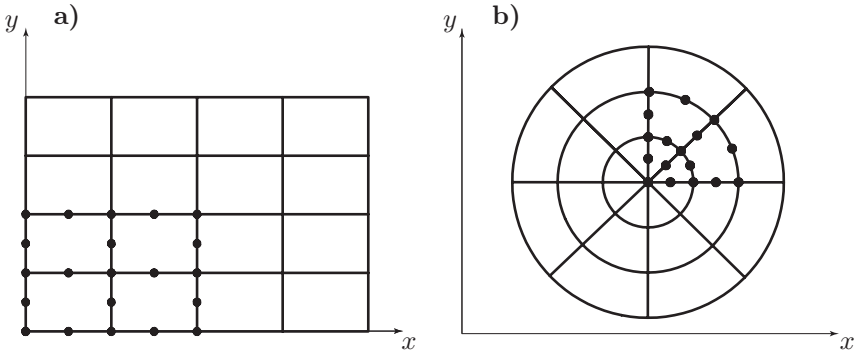

Figure 3.4: a) Finite element mesh of the rectangular plate. The mesh of the rectangular hole has the same configuration. b) Mesh of the circular hole.

but also to describe their geometry, simplifies the matter greatly [68]. The relationship between local coordinates ξ_i, η_i and τ_i and global coordinates x, y and z (in cartesian coordinates) for isoparametric elements can be formulated as

$$\xi_i = a_1 + a_2 x + a_3 y + a_4 z + a_5 xy + a_6 xz + a_7 yz + a_8 xyz + a_9 x^2 + ... \quad (3.29)$$

for the x-direction and analogously for the other two directions. The coefficients a_k are functions of the considered element's node positions, which are known due to the considerations presented above and can be calculated using an approach presented in [68]. For many of the well-established (solid) isoparametric elements, e.g. the 8-node brick with linear shape functions or the 20-node brick with quadratic ones, the coefficients a_k can be derived analytically, thus making it unnecessary to determine the local coordinates from the global ones numerically, which is less efficient. The determination of the local coordinates ξ_i, η_i and τ_i resulting from the node position $\mathbf{x}_i$ allows for a very quick assembly of the coordinate coupling matrix $\mathbf{S}$. This yields a very efficient calculation of the mass and stiffness matrices of the plate with hole. Nevertheless, it should be kept in mind that the assembly of the matrix $\mathbf{S}$ based on the conversion of global to local coordinates using the shape functions of the isoparametric elements could introduce modeling errors, if the

elements are distorted.

In the next section, a detailed convergence study of the rectangular plate with a rectangular or circular hole is presented to demonstrate the accuracy and efficiency of the method. As a measure for the convergence of the approach, the first six non-zero eigenfrequencies are computed.

3.3.2 Convergence study

Four cases of a free-free rectangular plate with a hole (see Fig. 3.3) will be considered. The cases are presented in Tab. 3.4 and differ with respect to the geometry of the hole (rectangular or circular) and the position of the hole's midpoint (in the middle of the plate or at an edge). The common dimensions

Case	Hole configuration	x_m	y_m
1	rectangular ($l_x = 0.25$m, $l_y = 0.25$m)	0.5m	0.5m
2	rectangular ($l_x = 0.25$m, $l_y = 0.25$m)	$\sqrt{2}/2$m	$\sqrt{2}/2$m
3	circular ($r = 0.25$m)	0.5m	0.5m
4	circular ($r = 0.25$m)	$\sqrt{2}/2$m	$\sqrt{2}/2$m

Table 3.4: Studied settings of the rectangular plate with a hole.

and parameters of the studied plates with a thickness of 0.01m are given in Tab. 3.5. The convergence study is performed calculating the first six

$a = 1$ m	$E = 206000$ MPa	$\rho = 7850$ kg/m^3
$b = 1$ m	$\nu = 0.3$	$\kappa = 0$

Table 3.5: Common dimensions and parameters of the analyzed plates.

non-zero eigenfrequencies of the four cases with the EMM and with ABAQUS with extremely fine meshes with approximately 470000 DOF consisting of 20-node brick elements of quadratic shape function order (C3D20 in ABAQUS terminology) serving as a reference solution. In Figs. 3.5 to 3.8, the relative error of the first and sixth natural frequency for all four cases is plotted versus

the number of DOF either in the hole's or in the plate's mesh. The calculated reference values are given in the captions. The number of DOF in the

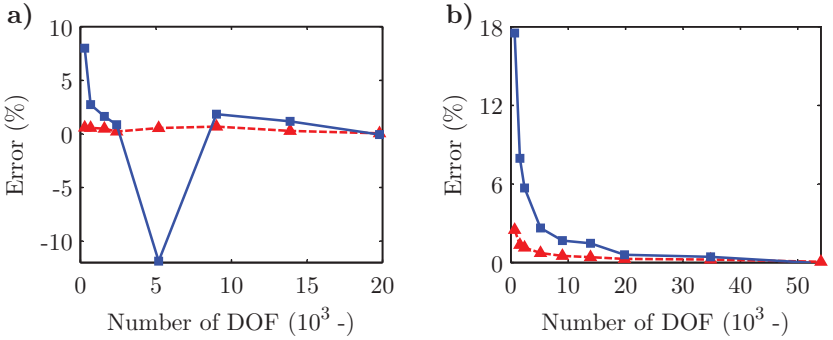

Figure 3.5: Convergence of the first and sixth eigenfrequency of case 1. a) 54009 DOF in the plate mesh, varying DOF in the hole mesh. b) 19809 DOF in the hole mesh, varying DOF in the plate mesh. The reference eigenfrequencies are 31,10 Hz and 140,15 Hz, respectively.

plate's mesh is kept constant in parts a), while in parts b) the number of DOF in the hole's mesh is constant. The minimal number of DOF in the base mesh corresponds to 5 elements in each direction and the maximum number to 50 elements. The characteristic side length of the plate's elements therefore varies between $0.2 \cdot a$ and $0.02 \cdot a$. It lies in the same range for the holes. The error for the first eigenfrequency is shown as a (red) dashed line, while the error for the sixth one is shown as (blue) solid line. As can be seen, the eigenfrequencies calculated with the EMM rapidly converge to the reference values for both the varying number of plate DOF and the hole DOF for all considered cases. The calculated results for the other four eigenfrequencies are not presented, but show exactly the same convergence behavior. It can be concluded that it is not necessary to use a high number of DOF in the hole's mesh for a certain required precision, but for the plate a much finer grid has to be used. The reason for this is that first the convergence of the plate without a hole has to be ensured by a proper choice of DOF before the hole can be inserted. This can be seen as a rather general guideline. Still, before using the

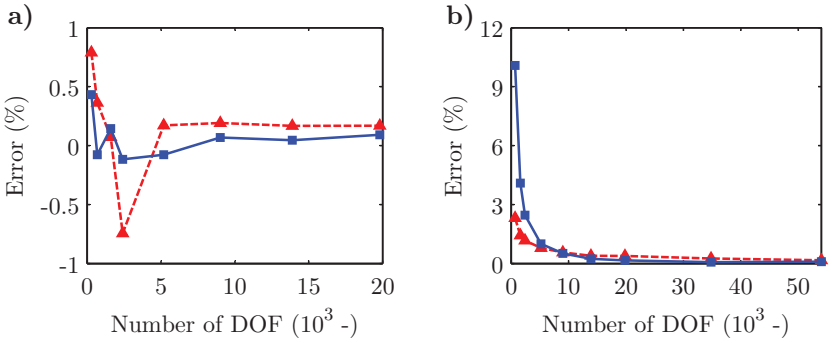

Figure 3.6: Convergence of the first and sixth eigenfrequency of case 2. a) 54009 DOF in the plate mesh, varying DOF in the hole mesh. b) 19809 DOF in the hole mesh, varying DOF in the plate mesh. The reference eigenfrequencies are 31,79 Hz and 142,75 Hz, respectively.

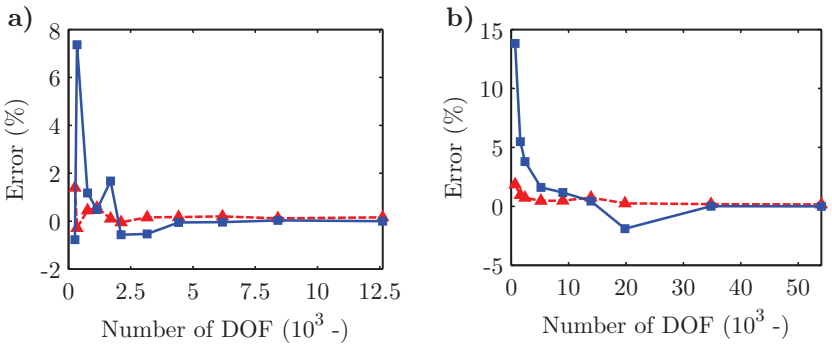

Figure 3.7: Convergence of the first and sixth eigenfrequency of case 3. a) 54009 DOF in the plate mesh, varying DOF in the hole mesh. b) 12609 DOF in the hole mesh, varying DOF in the plate mesh. The reference eigenfrequencies are 31,63 Hz and 145,34 Hz, respectively.

method e.g. in optimization problems, it is necessary to check the achieved convergence.

The results presented for the holes in the middle of the rectangular plate (case 1 and 3) are compared to results reported by Kwak et al. [63], calculated using the independent coordinate coupling method (ICCM) introduced

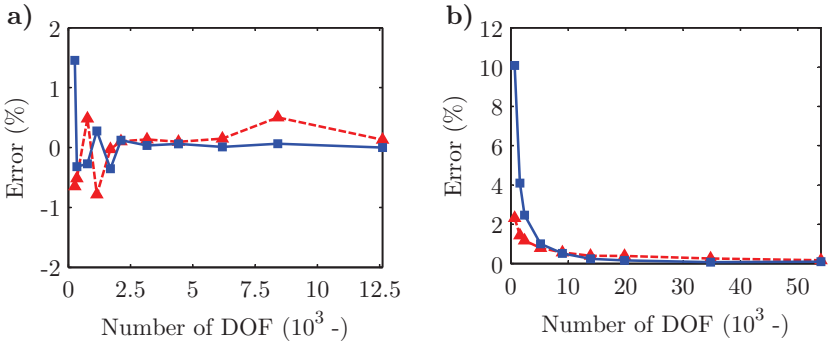

Figure 3.8: Convergence of the first and sixth eigenfrequency of case 4. a) 54009 DOF in the plate mesh, varying DOF in the hole mesh. b) 12609 DOF in the hole mesh, varying DOF in the plate mesh. The reference eigenfrequencies are 32,17 Hz and 144,03 Hz, respectively.

in their paper. The comparison is shown in Tab. 3.6. The results of the ICCM

C1 ref. sol.	C1 EMM	C1 ICCM	C3 ref. sol.	C3 EMM	C3 ICCM
31.10	31.12	32	31.63	31.68	31
44.67	44.67	45	45.57	45.55	44
54.78	54.83	57	55.87	55.86	56
84.58	84.61	85	84.78	85.03	82
84.58	84.61	85	84.78	85.03	82
140.15	140.07	149	145.34	145.34	137

Table 3.6: Comparison between the first six non-zero eigenfrequencies (Hz) calculated using the EMM and the ICCM presented in [63]. Also, a reference solution calculated in Abaqus is given. Case 1 (C1) and case 3 (C3) are considered.

have been taken from Figs. 10 and 14 presented in [63] in the highest possible observational accuracy, while the results of the EMM have been calculated using 20-node brick elements and 54009 degrees of freedom in the basis structure and 12609 degrees of freedom in the hole's mesh. The results are in good agreement, however, it should be kept in mind that the results in [63] were

obtained based on KIRCHHOFF plate theory while the results presented here were obtained using FE meshes with solid isoparametric elements.

On the one hand, the four discussed settings have been chosen to demonstrate that the EMM can not only be applied when meshes for basis structure and modification are similar, as in the rectangular plate with rectangular hole cases, but also when they differ in shape. On the other hand, it is shown that it is not necessary that nodes of the modification's mesh directly overlap the basis structure's nodes, which allows for the usage of non-matching meshes. It can also be seen that the eigenfrequencies calculated with the EMM do not represent upper bounds for the real eigenfrequencies, as would be the case using the well known standard RITZ method. This has been expected, since it has also been observed in the case of the inhomogeneous bar studied previously. Two interesting observations can additionally be made. The first remarkable point is that the rapid convergence of the method is partially caused by the fact that the allocation of the coordinate coupling matrix $\mathbf{S}$ is exact, since the mesh of the rectangular plate solely consists of regular bricks with edge angles of 90° making the transformation between global node coordinates of the hole to local coordinates of the plate element errorless. Consequently, this means that for a mesh with more distorted elements a slower convergence might be expected. The second observation is that most of the CPU time necessary to compute the eigenfrequencies with the EMM is needed for the solution of the eigenvalue problem and not for the allocation of the mass and stiffness matrices of the assembled rectangular plate with a hole. For the computation of the results presented here, the MATLAB function 'eigs' has been used to solve the eigenvalue problem and this took at least 80 % of the CPU time. Concluding, the assembly of the mass and stiffness matrices of the system can be considered as very efficient with the EMM. This strongly encourages the use of this approach in structural optimization problems regarding global properties like frequencies, where the modifications are not too complex. In the next section, the application of the method to the modelling of automotive and bicycle brake discs is discussed.

3.4 Application to brake discs

The EMM will be used as a basis for the structural optimization of brake discs in all design settings studied in this thesis, except for the case of a complex bicycle brake disc. For this case, the modelling technique differs, as will be discussed in more detail in section 4.5. The studied designs originate from applications of the automotive industry and the bicycle industry and are of varying complexity. First, an optimization of an automotive brake disc with N radial holes is presented in section 4.2, which represents a first, rather academic example, still giving useful insights. A schematic drawing of it is shown in Fig. 3.9.

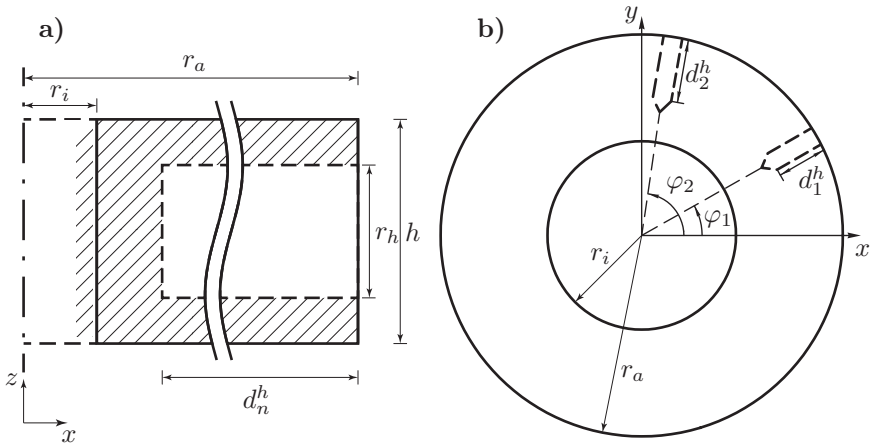

Figure 3.9: a) Cross section of the automotive brake disc with radial holes. b) Top view on the brake disc, two radial holes are shown exemplarily.

The rotor is assumed to be fixed at the inner radius across the complete thickness, where the term fixed refers to displacement and rotational DOF set to zero. The hat of the brake rotor is not modelled explicitly. It is not considered in the optimization, since changes in the geometry of the friction rings of the rotor are mainly intended to change the bending behavior of the rotor, which is hardly influenced by the hat, at least as long as the dimensions of the hat are small. In general, the hat can significantly influence the vibrational

behavior of the brake disc [8], therefore, a short justification for this modelling aspect follows in section 4.2.3. In Fig. 3.9, a), the cross section of the disc with radial holes is shown with an inner radius r_i, an outer radius r_a and a thickness h. The disc is assumed to have a modulus of elasticity E, a density ρ and POISSON's ratio ν, the holes of depth d_n^h are inserted using the EMM with negative material parameters $\overline{E} = -E$ and $\overline{\rho} = -\rho$. The top view on the disc is given in Fig. 3.9, b), where two radial holes are shown exemplarily with depths d_1^h and d_2^h and angles φ_1 and φ_2. In the optimization, the depth and angle of each hole is varied, while the radius r_h of the holes is predefined. The holes are drilled into the disc in such a way that their midpoints lie in the midplane of the disc. This model of a brake disc was optimized because it can readily be manufactured in a machine shop and is therefore highly suitable for the generation of test samples, however, it can only be a crude approximation of realistic brake discs with cooling channels.

A more realistic model of a brake disc with cooling channels is therefore necessary and shown in Fig. 3.10. The cooling channels are defined by cooling

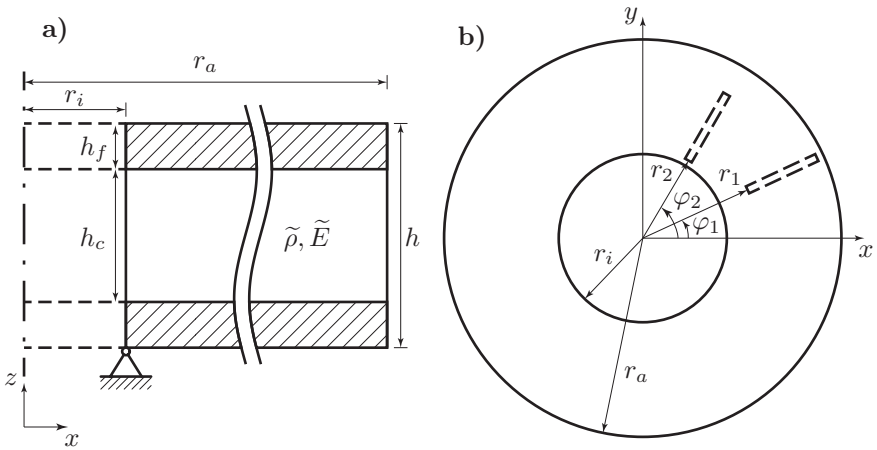

Figure 3.10: a) Cross section of the automotive brake disc with cooling channels. b) Top view on the brake disc, two cooling ribs are shown exemplarily.

ribs placed between the two friction rings and also connecting them. The cooling ribs are inserted into the clearance between the friction rings with

positive material parameters. The clearance is modeled as material with a very low density $\widetilde{\rho}$ and elastic modulus $\widetilde{E}$, all other modeling assumptions and basic parameters and dimensions are the same as for the disc with radial holes. The angular and radial position of the cooling ribs will be varied in the optimization. Two angles φ_1 and φ_2 and two radii r_1 and r_2 are shown in Fig. 3.10, b), respectively. Each friction ring has a thickness of h_f, a modulus of elasticity E and a density ρ as well as the cooling ribs, which have a thickness of h_c, the length l_c and the width b_c. The cooling ribs are all assumed to be of the same, constant shape. It would be possible to vary the shape of the cooling ribs also, but as will be shown in section 4.3, the optimization goal can be reached and even exceeded without this additional variation of the design parameters. The rotor is assumed to be simply-supported[1] at the inner lower ring, therefore, the hat of the brake rotor is not modeled explicitly, as was also the case for the disc with radial holes.

Not only automotive brake discs will be studied and optimized, but also bicycle brake discs. The design of bicycle brake discs is completely different from automotive ones as can be seen in Fig. 3.11, a), where a state-of-the-art bicycle brake disc of a major German manufacturer is shown. These brake discs are far smaller, thinner and lighter than automotive ones and normally manufactured of stainless, martensitic steel instead of cast iron. In the first optimization step, a simplified brake disc without the bars connecting the hub and the friction ring will be optimized by variation of the radial and angular position of axial holes drilled into the friction ring. For bicycle applications, these holes are intended to decrease the weight of the disc and can be found in all state-of-the-art brake discs with varying compositions. The friction ring is assumed to have free-free boundary conditions allowing to optimize the bending modes of the disc. A top view on the friction ring is shown in Fig. 3.11, b), where two holes with radial positions r_1 and r_2 and angular positions φ_1 and φ_2 are shown. Linear-elastic material with E, ρ and ν is assumed and the holes are inserted using the EMM with negative material parameters $\overline{E} = -E$ and $\overline{\rho} = -\rho$. The thickness is denoted as

[1] In this thesis, the term simply-supported refers to fixed displacement DOF and rotational DOF that are not limited.

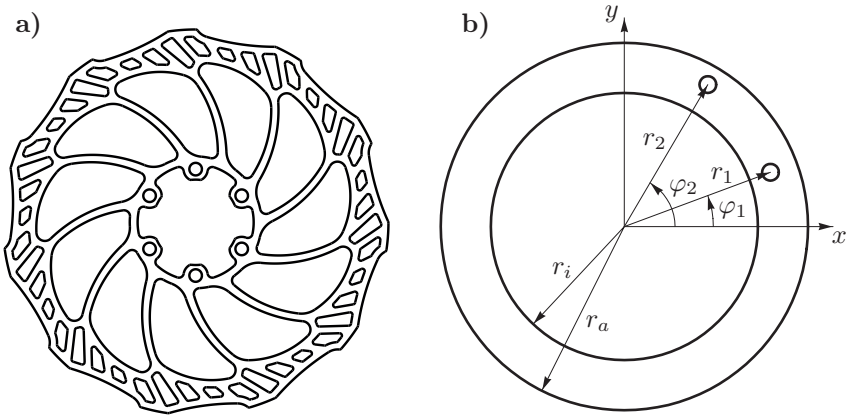

Figure 3.11: a) Steel bicycle brake disc of a major German brand. b) Top view on the friction ring of a bicycle brake disc, two axial holes are shown exemplarily.

h as in the case for the automotive brake discs and each hole is assumed to have a fixed radius r_h. A more realistic model of a bicycle brake disc is then introduced in paragraph 4.5.2. In the next chapter, the structural optimization of automotive as well as bicycle brake discs will be introduced and discussed in detail based on the modeling presented in this section.

4 Structural optimization of automotive and bicycle brake discs

In this chapter, an optimization of automotive as well as bicycle brake discs is presented with the goal to split their eigenfrequencies in order to avoid brake squeal. First, a short and concise overview over structural optimization in general is given to introduce the main concepts and optimization algorithms. Then, as a first example, the optimization of an automotive brake rotor with radial holes is shown starting with the statement of the optimization problem and its solution followed by test results obtained with a prototype disc manufactured in the final optimized design. It is demonstrated that the optimization goals have been achieved in theory and practice with a complete avoidance of brake squeal. Since the brake disc with radial holes is not a realistic case for practical applications in the automotive industry, a brake rotor with cooling channels has been optimized as a further step. Two different optimization approaches have been used, a deterministic mathematical programming approach and a heuristic evolutionary one. They are compared to each other and both deliver very satisfying results. However, brake squeal is not limited to the automotive case but also occurs in bicycle applications. A first introductory example of a bicycle brake disc optimization highlights the fact that the freedom in the design of potentially squeal-free bicycle brakes is required to be higher than in the case of automotive brake discs. This is considered in the optimization of the realistic bicycle brake rotor presented in the last part. Three optimized brake discs and two reference ones were tested on a bicycle test rig. Even though none of these designs could reach the theoretical limit of eigenfrequency separation to be completely squeal free, a significant improvement of squeal affinity has been achieved. This is demonstrated by a comparison to a commercially available brake rotor.

4.1 A short introduction to structural optimization

As has been shown in chapter 2, it is necessary to split the eigenfrequencies of the nonrotating brake rotor by a defined value in a certain frequency band to ensure a stable operating condition of the brake rotor in frictional contact and thus to avoid brake squeal. This goal can be achieved by a variation of the brake rotor's geometry leading to a structural optimization problem which can be written in mathematical form as

$$\begin{aligned} &\max_{p_n} \quad \min_{k} \quad |f_{k+1} - f_k| \\ &\text{s.t.} \\ &\mathbf{c}^{\text{eq}}(\mathbf{p}) = \mathbf{0} \\ &\mathbf{c}(\mathbf{p}) \leq \mathbf{0}, \end{aligned} \tag{4.1}$$

where f_k are the eigenfrequencies of the rotor and p_n the parameters varied during the optimization, e.g. the radial or angular position of cooling ribs (see section 4.3). While the inequality constraints $\mathbf{c}(\mathbf{p})$ can either be linear or nonlinear and result from limits of the optimization variables or minimal and maximal distance constraints, the equality constraints $\mathbf{c}_{\text{eq}}(\mathbf{p})$ are always nonlinear, representing the balance requirement of the rotor ensuring a safe and proper operation on a vehicle. This optimization problem is highly nonlinear, nonconvex, with linear and nonlinear constraints and has been shown to exhibit many local optima [108] making its numerical solution elaborate. This is complicated further by the fact that the evaluation of the objective function requires the solution of the eigenvalue problem, which is expensive if the system is modeled with many DOF, as is the case here. Nevertheless, there are structural optimization approaches and algorithms that can deal with this kind of problem.

An overview over the topic of structural optimization can be found in [37, 95, 96]. Most structural optimization problems are in fact nonlinear. A more general overview of these optimization problems can be found in [7]. Frequently, structural optimization is divided into sizing, shape and topology optimization. While sizing only allows the variation of some predefined

dimensions of a product, shape optimization allows more freedom in the design of the geometry by a more flexible (and changeable) parametrization of the boundaries [47, 62]. This additional freedom is very beneficial, however, special care is to be taken to properly select and combine the geometry representation and the analysis method, which is in most cases the FEM [96, 101]. Also, during the optimization, FE meshes have to be deformed or remeshing has to be conducted [120,135]. Finally, topology optimization allows the maximum amount of freedom in the design space by a possible change even in the topology of a structure [95, 96]. Some topology optimization approaches are discussed in [14, 37, 130, 136]. However, frequently it is desired to enable large changes in the geometry with a detailed description of the boundaries, which cannot directly be achieved with topology optimization. Therefore, level set methods for this kind of structural optimization have been proposed, which combine advantages of topology and shape optimimzation [71, 127–129, 131]. They allow for large geometry changes and changes in the topology but can be elaborate to use and can lead to frequent, ineffective remeshing of the structure if the FEM is used as analysis method. In the optimization problems dealt with in this thesis, large geometry changes are required while the topology is kept untouched. Thus, an easier modeling method has been applied, which has been presented in detail in chapter 3.

Often, the nonlinear optimization problems underlying shape or topology optimization are solved with mathematical programming algorithms [37], which use linear or quadratic approximations of the objective function and nonlinear constraints in the solution process [7]. One of the most common methods nowadays is the sequential quadratic programming (SQP) method [10, 97], which uses a series of quadratic approximations of the objective function and linear approximations of the nonlinear constraints to find a local optimum of the optimization problem. There are many other mathematical programming methods available, like the successive approximation method [10, 104] or interior-point algorithms; an initial overview is given in [7]. These methods are known to be efficient for problems which do not exhibit many local optima, especially if it is possible to derive design sensitivities analytically or at least semi-analytically [13, 120]. They are of local character, converging

only to local optima for most nonlinear optimization problems, and thus their performance might be poor for problems with many local optima and for non-continuous ones [118]. The problem to be addressed in this thesis, Eq. (4.1), exhibits many local optima. Nevertheless, it is possible to successfully apply mathematical programming algorithms for its solution, as will be shown in the following sections. As an alternative to mathematical programming methods, heuristic approaches are proposed in the context of structural optimization, which are known to have the potential to approach the global optimum. A first overview in very short form can be found in [7,37]. Nature inspired heuristics reach from well-known evolutionary strategies [93], genetic algorithms [4, 64] and simulated annealing [16] over particle swarm [29,56,132] and firefly [31,76] algorithms to the so-called harmony search algorithm [65, 72], just to name a few. All have in common that they are of rather global character and that they do not require design sensitivities or gradients for their operation. Despite these advantages, they are known to be computationally demanding. As will be shown in section 4.3.2, a genetic algorithm (GA) has been successfully applied for the optimization of an automotive brake disc with cooling channels. It is satisfactorily used for the optimization of a realistic bicycle brake disc as well, which is discussed in chapter 4.5.3.

This introduction into structural optimization has been quite general so far. There are, however, also many publications dealing with the optimization of structures to change their eigenvalues and eigenfrequencies, a review is presented in [33]. The objective in this thesis is to split all eigenfrequencies of a structure in a certain frequency range, still, most publications in this field only deal with the modification of the first eigenfrequency or the gap between the first two [129–131, 136]. The manipulation of eigenfrequencies in the context of structural optimization by geometry variation can be seen as an inverse problem to assign the imaginary eigenvalues of a structure by mass and stiffness variations. This problem has been discussed in [87] considering examples with few DOF and is shown to be nontrivial, which also hints to the complexity of the presented optimization problem.

In the following, the optimization of automotive and bicycle brake discs is presented. Before the details are explained in each section, the basic approach

is briefly introduced here, which is similar for all applications. It consists of three parts, as is shown in the flowchart given in Fig. 4.1. First, in part A, random initial configurations are generated, which are optimized with continuous algorithms in parallel in part B. The latter step is also the by far most time-consuming one. Three types of algorithms are chosen for this continuous optimization, either an interior-point, sequential quadratic programming or genetic algorithm. Afterwards, in part C, a check is conducted whether the found results are local optima or can still be enhanced by further optimization. This part is included in the algorithm implementations used, however, it is separately listed. This is due to the fact that for the optimization of realistic bicycle brake discs (presented in the last section of this chapter), the continuous optimization with a global genetic algorithm is followed by a continuous local search to enhance the found results further. This helps to reduce the runtime of the continuous GA. Also, the generation of random initial configurations is followed by a discrete optimization in this case to increase the distances between the eigenfrequencies of the initial rotor configurations up to a certain level before the more complex continuous optimization starts.

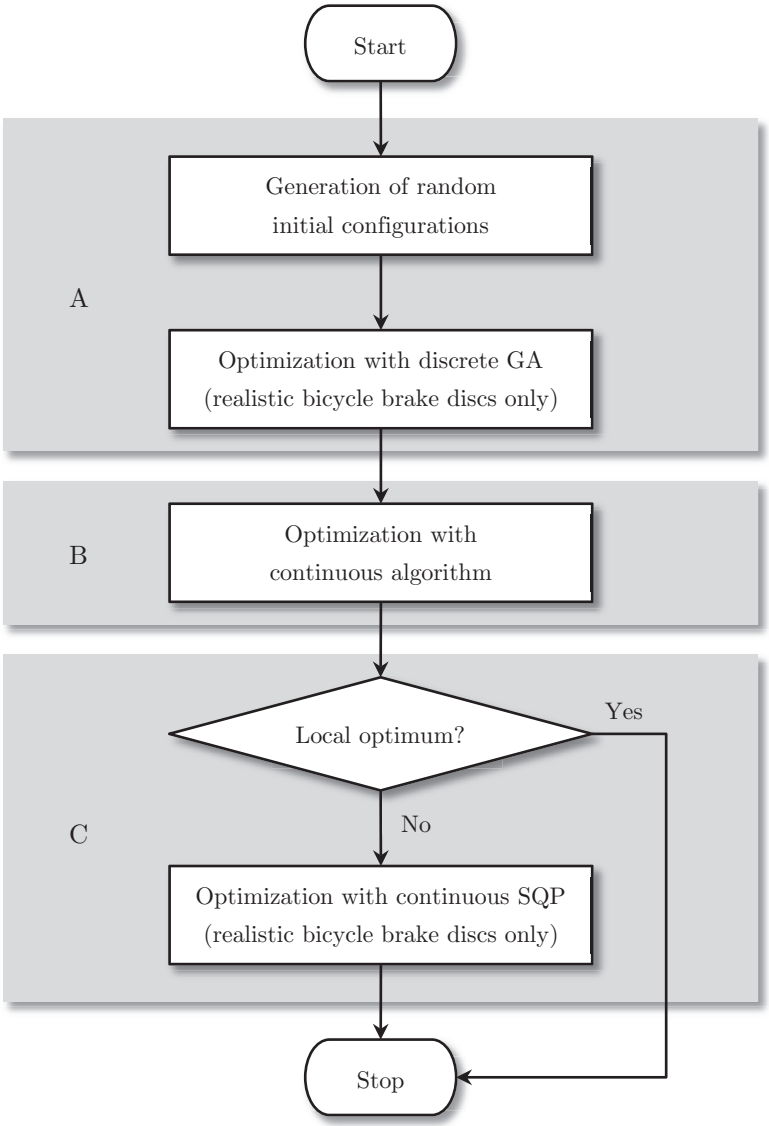

Figure 4.1: Flowchart illustrating the optimization approaches presented in this chapter.

4.2 Automotive brake disc with radial holes

As a first step, the optimization of an academic automotive brake disc with radial holes has been conducted. The intention has been to find an optimized design exhibiting the necessary grade of modal asymmetry to inhibit squeal and which can readily be manufactured in a machine shop. A prototype can thus be generated easily and be tested on a test bench. Therefore also, the material has been chosen to be steel instead of the common cast iron.

4.2.1 Optimization approach

The optimization goal to split all eigenfrequencies up to a limit frequency f_{lim} can be written in mathematical form as

$$
\begin{aligned}
&\max_{d_n^h,\,\varphi_n} \quad \min_k \ |f_{k+1} - f_k| \\
&\text{s.t.} \\
&d^h_{\mathrm{min}} \le d_n^h \le d^h_{\mathrm{max}} \\
&0 \le \varphi_n \le 2\pi \\
&\varphi_1 < \varphi_2 < \ldots < \varphi_N \\
&\mathbf{c}^{\mathrm{eq}}(d_n^h, \varphi_n) = \mathbf{0} \ \ (2 \ \text{ balance constraints}) \\
&\mathbf{c}(d_n^h, \varphi_n) \le \mathbf{0} \ \ (N \ \text{ min. distance constraints}),
\end{aligned}
\tag{4.2}
$$

if the angular positions φ_n and drilling depths d_n^h are varied while the radius r_h and number N of the holes is kept constant. The upper and lower bounds on the drilling depths are d^h_{min} and d^h_{max}, respectively. The parameters of the brake disc considered in this section are presented in Tab. 4.1 and represent a disc whose geometry fits to the brake test rig available at TU Darmstadt. A top view on the disc with the holes to be optimized is shown in Fig. 3.9, b).

The two scalar balance constraints can easily be formulated since the disc is assumed to be homogeneous, all holes have the same constant diameter and are drilled into the disc such that their midpoints lie in the midplane of the disc. As can be seen in Fig. 4.2, each inserted hole generates an inertia force $\mathbf{F}_n^f$ with the disc rotating at a constant rotational speed Ω. This leads to the

$E = 210000$ MPa	$N = 18$
$\nu = 0.3$	$r_p = 0.14$ m
$\rho = 7850$ kg/m^3	$\mu = 0.4$
$r_i = 0.076$ m	$k = 1.1 \cdot 10^6$ N/m
$r_a = 0.162$ m	$m^{\min_G} = 1.67$ kg
$h = 0.026$ m	$\alpha_M = 0.184$ s
$r_h = 0.008$ m	$\alpha_S = 2 \cdot 10^{-10}$ 1/s

Table 4.1: Parameters of the automotive brake disc with radial holes.

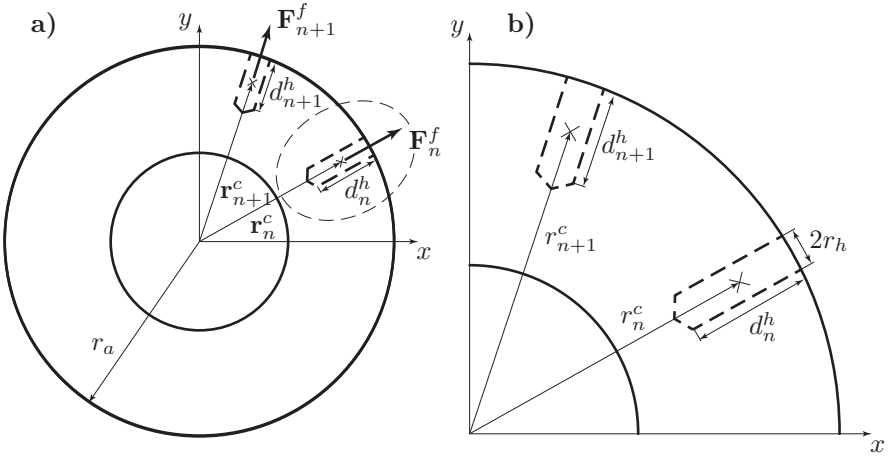

Figure 4.2: a) Inertia forces created by the unbalance introduced by the drilling of the holes. b) Radii r^c_n and r^c_{n+1} from the midpoint of the disc to the center of mass of two holes.

balance constraint in vector notation given by

$$\sum_n \mathbf{F}^f_n = \mathbf{0}, \tag{4.3}$$

where

$$\mathbf{F}^f_n = \rho V^h_n \mathbf{r}^c_n \Omega^2, \tag{4.4}$$

with the volume of each hole V^h_n and the radius to its center of mass $\mathbf{r}^c_n$. The

volume V_n^h of each hole is

$$V_n^h = \pi r_h^2 d_n^h + \frac{\pi}{3\tan 59^\circ} r_h^3 \tag{4.5}$$

under consideration of the tip of the hole with a tip angle of 118°. This also leads to the expression for the magnitude of the radius to the center of the mass

$$|\mathbf{r}_n^c| = \frac{\left(r_a - d_n^h/2\right)\pi r_h^2 d_n^h + \left(r_a - \frac{r_h}{4\tan 59^\circ} - d_n^h\right)\frac{\pi}{3\tan 59^\circ} r_h^3}{V_n^h}. \tag{4.6}$$

Inserting Eqs. (4.4) to (4.6) into Eq. (4.3), cancelling ρ and Ω and projecting the result onto x- and y-direction leads to the nonlinear balance constraints

$$\begin{aligned} c_1^{\mathrm{eq}}(d_n^h, \varphi_n) &= 1/V_{\mathrm{sub}} \textstyle\sum_{n=1}^N V_n^h |\mathbf{r}_n^c| \cos\varphi_n, \\ c_2^{\mathrm{eq}}(d_n^h, \varphi_n) &= 1/V_{\mathrm{sub}} \textstyle\sum_{n=1}^N V_n^h |\mathbf{r}_n^c| \sin\varphi_n. \end{aligned} \tag{4.7}$$

The constraints are normalized with respect to the volume $V_{\mathrm{sub}} = \sum_{n=1}^N V_n^h$ of all holes and therefore represent the projection of the eccentricity of the brake disc onto x- and y-direction. For a perfect statical and dynamical balance, these constraints would be required to be zero, however, for the optimization a bound e_{vio} is set on the violation of this constraints to achieve reasonable results. Since the x-y-plane ($z = 0$) is a plane of symmetry of the disc (with and also without holes), the axis of rotation (z-axis) automatically is a principal axis of inertia.

The N nonlinear minimal distance constraints c_n are intended to inhibit the overlapping of holes. The minimal distance between two holes is given by an angle $\Delta\varphi_{\min}$ between the holes' rims, as shown in Fig. 4.3. Simple geometric observations lead to

$$\begin{aligned} c_n(d_n^h, \varphi_n) = \Delta\varphi_{\min} - \varphi_{n+1} + \varphi_n + \arctan\frac{r_h}{\sqrt{r_a^2 - r_h^2} - d_{n+1}^h} \\ + \arctan\frac{r_h}{\sqrt{r_a^2 - r_h^2} - d_n^h}. \end{aligned} \tag{4.8}$$

Due to the fact that the hole depths can vary largely, it is necessary to write these constraints in a nonlinear form despite the fact that this makes the optimization problem more difficult and elaborate to solve. For the optimization

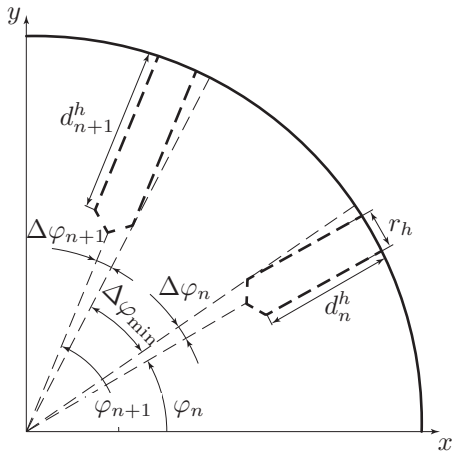

Figure 4.3: Zoom on two holes drilled into the disc to determine the minimal distance $\Delta\varphi_{\min}$ between two holes.

of cooling channels it is possible to write the distance constraints in a more beneficial linear form, as will be shown in section 4.3.1.

The FE meshes for the discretization of the model were generated using Abaqus with 3D solid isoparametric elements of quadratic shape function order (C3D20), where the disc has 16506 DOF and the holes have between 387 and 1719 DOF, depending on their depth d^h_n. This choice of the number of degrees of freedom offers a good compromise between convergence and runtime of the optimization process, which is significant in this case (see below). The parameter κ (see Eq. (3.26)) was set equal to zero. In order to avoid very fine meshing of the tip of the holes, the tip in the model is replaced by a length correction of the holes' cylinder, conserving the volume of the hole. The grade of modal asymmetry that has to be achieved during the optimization is a split between the eigenfrequencies of 50 Hz estimated with Eq. (2.20), using the parameters given in Tab. 4.1. Despite the fact that the limit frequency is 9100 Hz, the optimization considers the first 25 eigenfrequencies of the structure up to 14000 Hz. This is reasonable, since the measured eigenfrequencies will be considerably lower than the optimized ones due to the assumption of a fixed inner ring in the model, as will be shown

in section 4.2.3. The physical parameters for the optimization are presented in Tab. 4.2. The choice of $e_{\text{vio}} = 0.001$ m corresponds to an inertia force of

$d^h_{\min} = 0.005$ m	$\Delta\varphi_{\min} = 5^{\text{o}}$
$d^h_{\max} = 0.075$ m	$e_{\text{vio}} = 0.001$ m

Table 4.2: Parameters for the optimization of the brake disc with radial holes.

approximately 10 N at a vehicle speed of 200 km/h, which is assumed to be tolerable. Also, a violation of the minimal angle $\Delta\varphi_{\min}$ between two holes of 0.001 rad is accepted during the optimization.

An interior-point algorithm provided by the MATLAB Optimizaton Toolbox was chosen to solve the optimization problem, which is able to target local optima of the nonlinear, nonconvex objective function [7]. In order to increase the possibility to achieve satisfying results, which are results with a split between the eigenfrequencies larger than 50 Hz, 12 randomly generated starting configurations were optimized in parallel. In order to avoid very long runtimes, each optimization was stopped in the iteration after reaching 5000 evaluations of the objective function. A solution was treated as a local optimum if the change in the objective function between the last two iterations was below 10^{-12}, the size of the last step below 10^{-8} and the nonlinear constraints where satisfied to the limits given above[1].

A comparison between the maximum minimal distances between the eigenfrequencies obtained in the 12 optimization runs is shown in Fig. 4.4, a). The dashed, red line shows the limit of 50 Hz above which the solutions are treated as satisfying exhibiting the necessary grade of modal asymmetry to avoid squeal. It can be seen that nine of twelve optimization runs lead to a minimal separation between the eigenfrequencies larger than the necessary split and three of them have a split larger than 70 Hz. The best configuration exhibits 73,6 Hz separation and is shown in Fig. 4.4, b) together with its starting configuration. Large changes in the geometry were necessary to realize this optimum, which could successfully be achieved using the EMM as modeling

[1] All three conditions hold simultaneously.

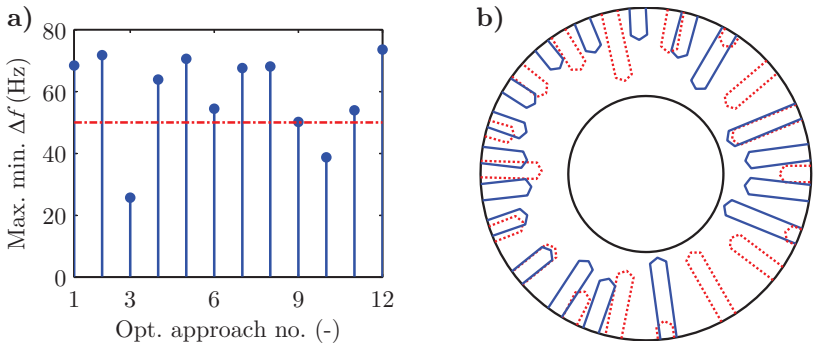

Figure 4.4: a) Comparison of the maximum minimal distance between the eigenfrequencies of the twelve optimization approaches. b) Hole configuration of the best optimized result (solid, blue line) and the starting configuration (dashed, red line).

method. The best result was reached after 5045 function evaluations, which is at the predefined limit. The algorithm was stopped prematurely, but since the changes in the objective function were very small in the last iterations, it was assumed that a local optimum had been found. The runtime cumulated up to about two weeks for all 12 optimization runs on a Intel Xeon system with two X5650 processors and 24 GB RAM. The optimized eigenfrequency distribution of the best result is shown in Fig. 4.5, a) and it can be seen that the basic distribution did hardly change during the optimization with respect to the distribution of the starting configuration. Nevertheless, the distances between the eigenfrequencies have been increased reasonably as is demonstrated in Fig. 4.5, b). The smallest minimal distances achieved are all at the lowest eigenfrequencies, additionally there are at least four distances with nearly exactly the same magnitude. The success of the optimization becomes even more pronounced if the distances of the best optimized results are compared to the distances between the eigenfrequencies of a full, symmetric disc without holes, as is shown in Fig. 4.6, a). The full disc has many double eigenfrequencies due to its geometric symmetry, while the optimized one has a high grade of modal asymmetry.

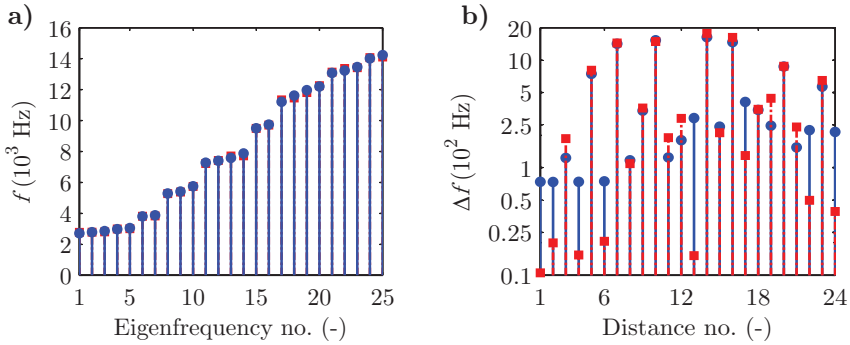

Figure 4.5: a) Eigenfrequency distribution of the best optimized result (solid, blue line, circular markers) and the corresponding starting configuration (dashed, red line, square markers). Both distributions are nearly congruent. b) Distances between the eigenfrequencies for the best result (solid, blue line, circular markers) and its starting configuration (dashed, red line, square markers). The y-axis is in logarithmic scale.

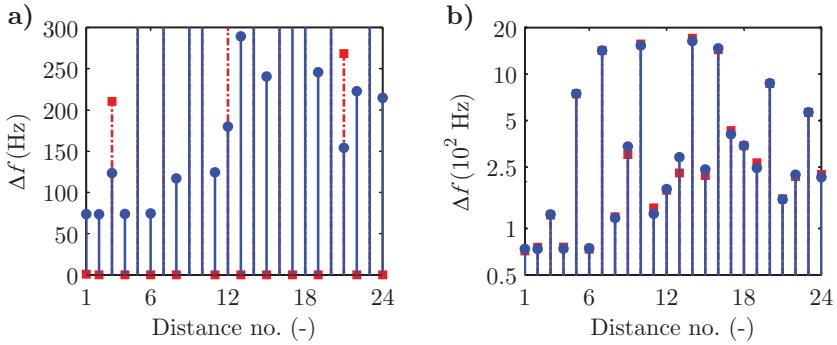

Figure 4.6: a) Distances between the eigenfrequencies of the best found configuration (solid, blue line, circular markers) and the full disc (dashed, red line, square markers). b) Distances between the eigenfrequencies of the rounded (solid, blue line, circular marker) and the exact (dashed, red line, square markers) best configuration. The y-axis is in logarthmic scale.

Still, the robustness of the solution could be in doubt under consideration of manufacturing inaccuracies. In order to assess this issue, the best opti-

mization result was rounded to one degree in the angular position and one millimeter in drilling depth and the resulting distances were calculated again. The chosen angular and radial precision was a worst case assumption on the precision of the machine shop's process of manufacturing the prototype and is equivalent to a maximum change in the optimization parameters d_n^h and φ_n of 6%. The distances of the rounded configuration are shown in comparison to the values resulting from the exact configuration in Fig. 4.6, b). The four smallest distances between the eigenfrequencies do not change more than 4% due to the rounding process, which reflects the robustness of the obtained solution against manufacturing uncertainties. A consideration of uncertainties in the parameters could be taken into account during the optimization, possibly leading to an even increased robustness. However, the achieved result was considered to be satisfying in this respect. Furthermore, the evaluation of the objective function is considered to be too expensive to allow for an optimization under uncertainties. For tests on the brake test bench at TU Darmstadt, the optimized disc and a full disc without holes as a reference were manufactured using S235JR steel.

4.2.2 Test results

Two types of tests were performed with the two prototype discs, originally presented in the Bachelor thesis [57]. First, a modal analysis to check the distances between the eigenfrequencies and therefore validate the optimization results. Second, a squeal test to determine the achieved reduction in squeal affinity of the optimized brake rotor. The test rig is shown in Fig. 4.7 with the optimized brake rotor attached. In Fig. 4.7, a), a front view on the test rig is shown. The bench contains an original car suspension, where fixation of the brake disc is guaranteed by an adaptor instead of a rim. This allows measurements with the laser vibrometer on the complete surface of the disc. Also, it can be seen that the caliper is attached to the test rig. This allows for the application of adjustable brake pressure during squeal tests; the caliper is detached from the test rig during modal analysis tests. While during the latter tests the disc is not rotating, it is driven by an electrical motor for squeal

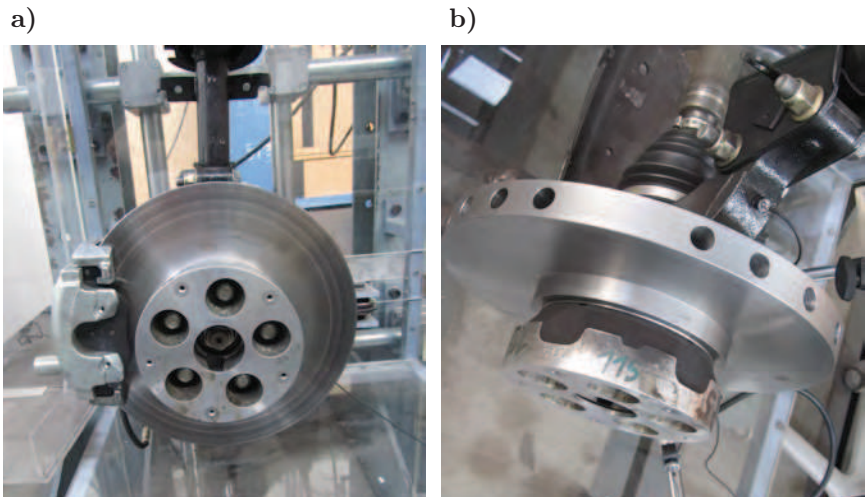

Figure 4.7: a) Front view and b) top view on the brake test bench.

tests, the rotational speed being adjustable. The shaft from the engine to the disc can be seen in a top view on the test bench presented in Fig. 4.7, b). From this perspective also the holes drilled into the disc in its midplane can be seen, with varying angles between them and different drilling depths.

The surface velocity of points on the rotor is measured by a POLYTEC laser vibrometer with a PSV-400 scanning head in the modal as well as in the squeal analysis test case. The disc is excited by hammer impulses at a point at the backside of the disc for the modal analysis shown here and the transfer function between the velocity signal of the laser vibrometer and the force transducer of the modal hammer is calculated. An Hanning window is used in the evaluation of the vibrometer signals to avoid leakage effects. This is not necessary for the force signal of the hammer. A regularly spaced grid with 150 measurement points on the surface of the disc is used to enable the recording of disc eigenmodes up to higher orders. Ten measurements were taken at each point followed by an averaging of the complex signals, to increase the reliability of the measurements. The sampling frequency was set to 32 kHz, which allows a bandwidth of 12.5 kHz in the frequency response spectrum

using POLYTEC's analysis unit. Still, the bandwidth was limited further by the hammer excitation, as will be shown below. For the modal analysis case, the resolution of the frequency response spectrum was 1.95 Hz, while it was 3.9 Hz in the squeal test case offering a reasonable accuracy.

Figure 4.8 shows the normalized FOURIER-transform of the force transducer signal of the modal hammer. It can be seen that the signal level crosses -10 dB

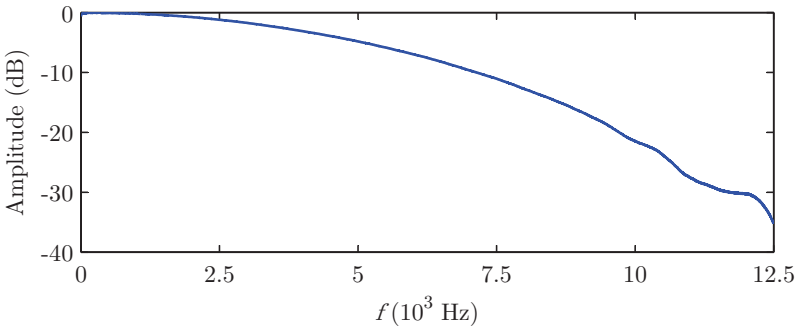

Figure 4.8: Normalized spectrum of the force signal of the modal hammer.

at approximately 8 kHz, which is the level up to which the measurements are assumed to be trustworthy. This limit is strongly influenced by the tip used on the modal hammer, which was a steel one in this case to increase the limit as far as possible. Due to this limit, also the transfer function between the laser vibrometer's velocity signal and the modal hammer's force signal, shown in Fig. 4.9, a), is only evaluated up to 8 kHz, instead of the originally possible 12.5 kHz. For the generation of this figure, the transfer functions of all 150 measurement points are averaged for higher reliability. Figure 4.9, b) shows the coherence between the velocity and force signal and is close to one at least at the peaks of the transfer functions mentioned before. A comparison between the spectrum of the full, symmetric disc and the optimized one presented in Fig. 4.9, a) shows that the (visible) eigenfrequencies of the optimized disc are indeed all split significantly while they are double in the full disc case. This proves the efficacy of the optimization. Additionally to the generation of these transfer functions, it is also possible to visualize the operating deflection

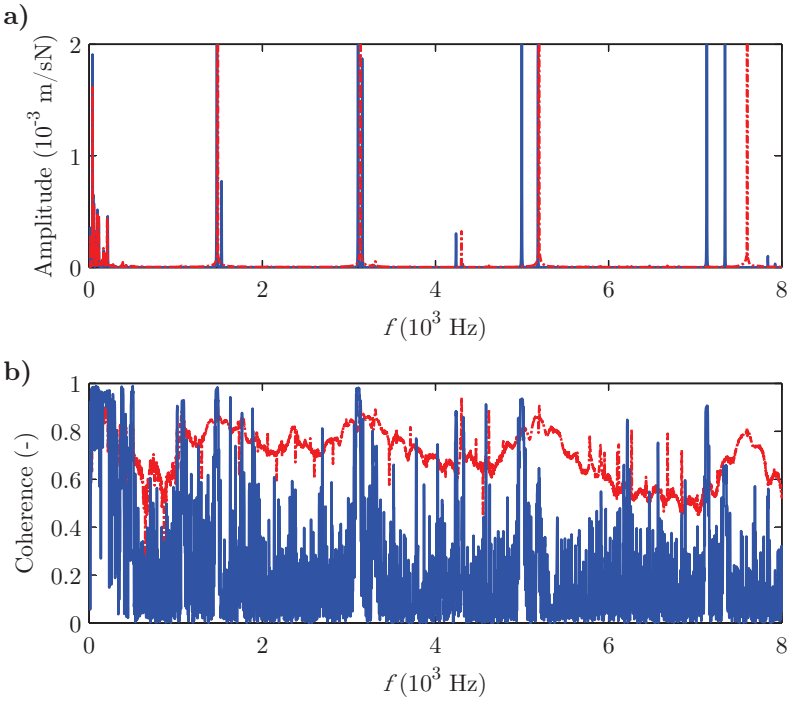

Figure 4.9: a) Transfer function between the velocity signal of the laser vibrometer (measuring the surface velocity) and the force transducer signal of the modal hammer. Full disc (dashed, red line) and optimized disc (solid, blue line). b) Coherence between the laser vibrometer's velocity signal and the force transducer's signal of the modal hammer. Full disc (dashed, red line) and optimized disc (solid, blue line).

shapes of the brake disc using the POLYTEC software accompanying the laser vibrometer. This allows the identification of the eigenmodes of the brake rotor in a realistic assembly state. In this thesis, the denomination of the bending-dominated modes of the disc follows IRRETIER [55], where each mode shape is labeled as α/β. α represents the number of nodal lines in circumferential direction and β the number of nodal lines in radial direction. The clearly identifiable eigenmodes of the full disc and the optimized one are presented in Tab. 4.3 in conjunction with the corresponding measured eigenfrequencies

f_i and the distances Δf_i between the eigenfrequencies of the optimized brake rotor. Since all eigenmodes of the symmetric disc are double ones, only one

Eigenmode	f_i (FD)	f_i (OD)	Δf_i (OD)
2/0	1486	1476	53
		1529	
3/0	3131	3107	47
		3154	
4/0	5194	5000	186
		5186	
5/0	7600	7132	212
		7344	

Table 4.3: Measured eigenmodes of the full disc (FD) and the optimized one (OD).

measured frequency is given in the table. The conclusion can be drawn that the optimization to split the eigenfrequencies at least by 50 Hz was successful, if the missing 3 Hz in the distance of the 3/0 modes are attributed to measurement inaccuracy. In order to complete the discussion on the success of the optimization from a modal analysis point of view, a note on the difference between measurements and calculation results follows in section 4.2.3.

The grade of modal asymmetry of the optimized disc should be sufficient to exclude squeal. Squeal tests were performed at the brake test rig at TU Darmstadt to verify (or rebut) this statement. For these tests, the brake pressure was varied between 1 bar and 15 bar and the rotational frequency between 1 rad/s and 20 rad/s, which is equivalent to a vehicle speed of approximately 1 km/h and 20 km/h. The surface temperature of the brake rotor was measured before and after each test, it did never rise above 100° Celsius. Using the laser vibrometer, the velocity amplitude of one point on the surface of the disc was measured, from which the spectrum during squeal could be determined. As a result, the spectrum for squeal of the full disc is presented in Fig. 4.10. The disc did squeal in a broad band of rotational frequencies from 5 rad/s to 15 rad/s but in a more narrow pressure band of 8 bar to 10 bar. The squeal was

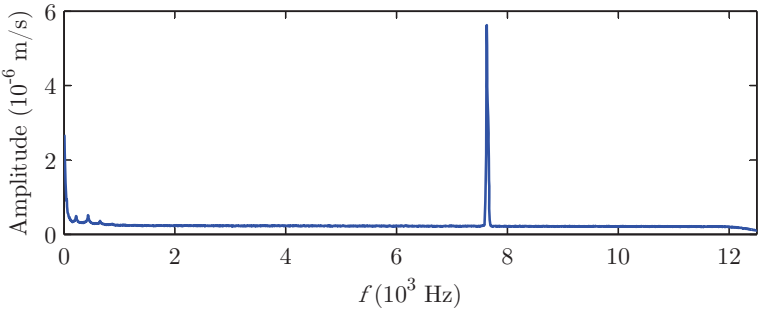

Figure 4.10: Spectrum of the laser vibrometer's velocity signal during squeal of the full, symmetric disc.

always monofrequent with a frequency of 7.6 kHz, which exactly corresponds to the 5/0 eigenmode of the disc without brake pads. The pads obviously change the eigenfrequencies of the disc only marginally, which justifies the modeling assumption to consider the terms originating from the brake pad as perturbations.

The same squeal test procedure was applied to the optimized brake disc with 18 holes. The measured surface velocity spectra for the same range of rotational speed and brake pressure were analyzed. Still, no significant amplitude in the spectra could be identified, the brake disc did not squeal under any applied braking condition.

The three following points should be kept in mind concerning the interpretation of these test results. First, the existing test rig at TU Darmstadt does not allow to change the environmental conditions like air humidity or temperature during the test, as is possible with more sophisticated test rigs used in the automotive industry. Second, the tests were performed with constant rotational speed, realistic stops with decreasing speed could not be performed. And third, wear occuring over the lifetime of a brake disc and especially of the pad could not be simulated. Despite these three facts, the test results strongly indicate that the desired split of 50 Hz between the first 25 eigenfrequencies of the brake disc indeed avoids brake squeal completely. This can be considered

as a verification of the theory underlying the optimization, which has been presented in chapter 2. Later, in section 4.5.4, test results with realistic bicycle brake discs will be presented, backing up the experimental findings shown here for the automotive brake discs with radial holes.

4.2.3 On the choice of boundary conditions for the optimization

As has been noted in section 3.4, the boundary conditions for the disc to be optimized were fixed at the inner radius of the disc (across the complete thickness) and free elsewhere; a hat was not modeled explicitly. This is motivated by the fact that including the hat of the disc in the modeling would drastically increase the number of DOF due to the rather complex geometry of this thin design feature. And since an increase in the number of DOF leads to a disproportionate increase in the computational time required to solve the eigenvalue problem, which accounts for most of the CPU time required in the optimization, this is very undesired. Of course, the manufactured prototype has a small hat for fixation on the test bench (see Fig. 4.7, b)) and therefore the boundary conditions at the inner rim of the disc do not match the model's ones exactly. Thus, the first measured eigenfrequencies are significantly lower than the calculated ones, as is shown by the comparison of calculated and measured eigenfrequencies of the optimized disc presented in Tab. 4.4. However, three additional observations can be made. The first is that the higher eigenfrequencies are very closely approximated by the model (without hat and fixed inner ring), which matches the expectations [35]. The second is that the differences between the eigenfrequencies are lower in the measurements than in the model, however, they are still in the range of the goal of 50 Hz. The last is that also the tendency is correct: The smallest differences in the eigenfrequencies occur at the low eigenfrequencies in the model as well as in the measurements. As a conclusion, it is assumed in this thesis that it is acceptable not to model the hat explicitly but to use appropriate boundary conditions. Thus, the hat will also not be modeled explicitly for the optimization of the more realistic brake rotor with cooling channels

Eigenmode	f_i (F)	Δf_i (F)	f_i (H)	Δf_i (H)
2/0	2779	74	1476	53
	2853		1529	
3/0	3795	74	3107	47
	3869		3154	
4/0	5287	117	5000	186
	5404		5186	
5/0	7275	124	7132	212
	7399		7344	

Table 4.4: Eigenfrequencies f_i and corresponding distances between the eigenfrequencies Δf_i of the optimized 18 hole disc. Calculations with fixed inner rim and without hat (F) and measurements with a hat (H).

presented in the next section. This brake rotor is smaller, lighter and has a less stiff hat, as the geometry resembles a series brake disc of a major German car manufacturer. Since the hat is less stiff than in the case presented above, the boundary conditions are changed to a simply supported inner ring (and a free outer one).

4.3 Automotive brake disc with cooling channels

In this section a structural optimization of a cast iron brake rotor with cooling channels is presented. This type of brake rotors is widely used in the automotive industry. Using the parameters presented in Tab. 4.5, the minimal necessary distance between the eigenfrequencies of the disc can be estimated to be approximately 50 Hz and the limit frequency above which the system does not squeal is 9 kHz. For the estimation of this limit frequency very low damping parameters are used since no measurement data is available and the estimate is intended to be conservative.

$E = 140000$ MPa	$h_c = 0.009$ m
$\nu = 0.25$	$b_c = 0.0065$ m
$\rho = 7200$ kg/m^3	$r_p = 0.125$ m
$r_i = 0.079$ m	$\mu = 0.4$
$r_a = 0.138$ m	$k = 1.1 \cdot 10^6$ N/m
$h = 0.026$ m	$m_G^{\min} = 1.81$ kg
$h_f = 0.0085$ m	$\alpha_M = 0.184$ s
$l_c = 0.043$ m	$\alpha_S = 2 \cdot 10^{-10}$ 1/s

Table 4.5: Parameters of the automotive brake disc with cooling channels.

4.3.1 Optimization approach

The layout of the cooling channels of the considered automotive brake disc is to be optimized. Therefore, the radial position r_n and the angle φ_n of each of the N cooling ribs is varied, while their shape (l_c and b_c) is kept constant. In Fig. 3.10, b), two cooling ribs are shown exemplarily, one at an angle φ_1 and radius r_1 and the other with an angle φ_2 and radius r_2. The parameters of the brake disc are presented in Table 4.5. The optimization problem to split all eigenfrequencies f_k of the rotor up to a limit frequency of $f_{\lim}$ (here 9 kHz) can be written as

$$
\begin{aligned}
&\max_{r_n, \varphi_n} \quad \min_k \quad |f_{k+1} - f_k| \\
&\text{s.t.} \\
&r_{\min} \leq r_n \leq r_{\max} \\
&0 \leq \varphi_n \leq 2\pi \\
&\varphi_1 < \varphi_2 < \ldots < \varphi_N \\
&\varphi_n - \varphi_{n+1} \leq -\Delta\varphi_{\min} \ \text{(min. distance constraints)} \\
&\varphi_{n+1} - \varphi_n \leq \Delta\varphi_{\max} \ \text{(max. distance constraints)} \\
&\mathbf{c}^{\mathrm{eq}}(\mathbf{r}, \varphi) = \mathbf{0} \ \ (2 \ \text{balance constraints}),
\end{aligned}
\tag{4.9}
$$

where $r_{\min}$ and $r_{\max}$ are the minimal and maximal radii of each cooling rib to keep a minimal distance between cooling rib and inner and outer radius of the brake disc. $\Delta\varphi_{\min}$ and $\Delta\varphi_{\max}$ are the minimal and maximal angles

between two cooling ribs and thus give the minimal and maximal distances between them, which have to be kept due to cooling and material strength requirements. In contrast to the case with radial holes, the maximal and minimal distance constraints can be written in linear form, since the variation in radial direction is much smaller. The brake disc has to be statically and dynamically balanced leading to the nonlinear equality constraints

$$\begin{aligned} c_1^{\mathrm{eq}}(\mathbf{r},\varphi) &= \textstyle\sum_{n=1}^{N} r_n \cos\varphi_n, \\ c_2^{\mathrm{eq}}(\mathbf{r},\varphi) &= \textstyle\sum_{n=1}^{N} r_n \sin\varphi_n, \end{aligned} \tag{4.10}$$

which can easily be derived, since the brake disc's friction rings and each of the cooling ribs are assumed to be homogeneous bodies of constant geometry rotating at a constant angular velocity. These constraints for static balancing represent the projection of the excentricity of the brake disc induced by the placement of the cooling ribs onto x-direction (c_1^{eq}) and y-direction (c_2^{eq}), respectively. Also, the dynamic balancing is automatically guaranteed due to the symmetry with respect to the middle plane of the disc.

As has been introduced in section 4.1, the presented optimization problem is nonconvex and nonlinear with linear and nonlinear constraints and many local optima to be expected. The brake disc to be optimized is modeled using the method proposed in chapter 3. The underlying FE meshes of the friction rings and each cooling rib have been assembled using ABAQUS with 3D solid isoparametric elements of quadratic shape function order (C3D20) leading to 65250 DOF in the friction ring mesh and 4860 DOF for each cooling rib, fulfilling convergence requirements. The parameters of the filling material between the friction rings were chosen as $\widetilde{E} = 1.4$ MPa and $\widetilde{\rho} = 1$ kg/m^3. Since the limit frequency f_{lim} is estimated to be 9 kHz, the first 21 eigenfrequencies of the brake disc with $N = 39$ cooling ribs are considered in the calculation. Solutions are treated as infeasible if one of the constraints c_1^{eq} and c_2^{eq} is violated by an absolute value of 0.005 m. The parameters for the upper and lower bounds and the linear constraints can be found in Tab. 4.6. Due to the properties of the optimization problem, deterministic optimization approaches cannot guarantee the finding of the global optimum, therefore, heuristic algorithms are indicated. In the following, these two types of algorithms will be

$r_{\min} = 0.08$ m	$\Delta\varphi_{\min} = 4^{\circ}$
$r_{\max} = 0.094$ m	$\Delta\varphi_{\max} = 12^{\circ}$

Table 4.6: Parameters for the optimization.

compared and their performance will be assessed.

4.3.2 Comparison between optimization algorithms

First, a deterministic SQP approach is chosen to solve the optimization problem. Since SQP procedures are known to be efficient for finding local optima but unable to guarantee the finding of the global optimum for the problem class considered here [7], 20 randomly chosen starting points were generated to increase the probability of finding satisfying solutions. In the context addressed here, satisfying results mean results that exhibit a minimal separation of eigenfrequencies of at least 50 Hz in the frequency range up to 9 kHz. The MATLAB Optimization Toolbox provides the SQP implementation used here, an overview over the results is given in Tab. 4.7. In order to avoid over-long runtimes, the optimization was stopped in the iteration after reaching 10000 function evaluations, if the algorithm did not find a local optimum before or ended due to infeasibility. This led to a termination of the algorithm in 6 of 20 cases, all of which leading to feasible solutions and mostly very good results. Furthermore, 7 of 20 optimization runs led to infeasible configurations. A solution was treated as a local optimum if the change in the objective function between two optimization iterations was below 10^{-12}, the absolute value of the step size below 10^{-8} and the constraints were satisfied (to the limit given above).

Figure 4.11, a) shows a comparison of the maximum minimal distances between the eigenfrequencies which could be realized in the 13 feasible optimization approaches. A dashed (red) line shows the limit of 50 Hz, above which the solution is assessed as satisfactory fulfilling the requirement to avoid squeal. It can be seen that only 7 of the SQP approaches led to good results, while 13 fail, either because of constraint violation, or a solution exhibiting

No.	No. iter.	No. f. eval.	Constr. vio. (m)	Min. Δf (Hz)	Infeas.
1	10	963	$4.1 \cdot 10^{-3}$	45.3	
2	58	5369	$2.6 \cdot 10^{-2}$	58.8	x
3	111	10026	$2.5 \cdot 10^{-6}$	64.5	
4	44	4247	$1.9 \cdot 10^{-2}$	67.2	x
5	16	1633	$1.1 \cdot 10^{-1}$	67.2	x
6	13	1283	$7.7 \cdot 10^{-3}$	43.4	x
7	70	6242	$3.6 \cdot 10^{-5}$	60.6	
8	115	10061	$5.1 \cdot 10^{-8}$	75.8	
9	7	649	$3.8 \cdot 10^{-3}$	42.5	
10	33	3589	$3.2 \cdot 10^{-2}$	57.1	x
11	112	10061	$4.7 \cdot 10^{-8}$	68.3	
12	114	10076	$2.4 \cdot 10^{-8}$	71.1	
13	107	10064	$3.7 \cdot 10^{-7}$	49.7	
14	7	650	$3.8 \cdot 10^{-3}$	35.8	
15	13	1304	$4.1 \cdot 10^{-3}$	45.3	
16	57	5231	$1.1 \cdot 10^{-2}$	67.9	x
17	20	1779	$3.9 \cdot 10^{-3}$	58.0	
18	117	10042	$2.9 \cdot 10^{-9}$	73.3	
19	14	1391	$4.7 \cdot 10^{-2}$	43.0	x
20	7	650	$3.8 \cdot 10^{-3}$	35.8	

Table 4.7: Number of iterations, function evaluations, max. violation of constraints, minimal difference between the eigenfrequencies Δf and infeasibility of the solutions of the 20 SQP optimization approaches.

a separation of eigenfrequencies being too small. In the best case, a minimal difference between the eigenfrequencies of 75.8 Hz was realized comprising a very high grade of modal asymmetry. The eigenfrequency distribution of the best SQP optimization result and its corresponding starting configuration is given in Fig. 4.11, b), which did not change significantly during the optimization. A comparison between the starting configuration's distances between

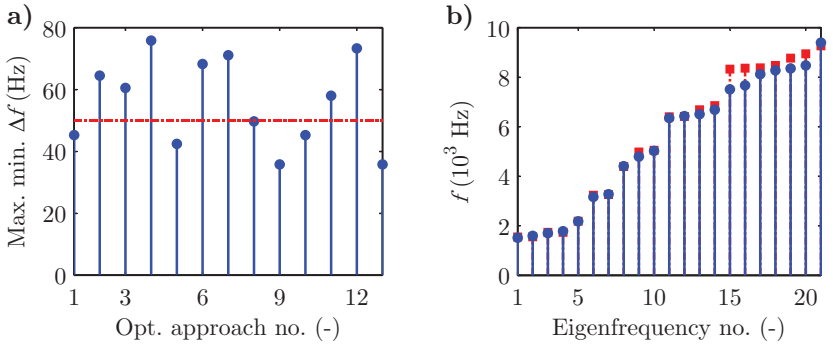

Figure 4.11: a) Maximum minimal distance Δf between the eigenfrequencies of the 13 feasible SQP optimization runs. b) Eigenfrequency distribution of the best result found with the SQP algorithm (solid, blue line, circular markers) and of its starting configuration (dashed, red line, square markers).

the eigenfrequencies and the optimized configuration's distances is shown in Fig. 4.12, a). Clearly, the minimal difference between the eigenfrequencies has been increased largely during the optimization. The significance of this fact is demonstrated even more intensely if the best result is compared to a reference configuration exhibiting a cyclic symmetry. In this configuration, the ribs are placed exactly in the middle between inner and outer radius of the disc and the angles are evenly distributed leading to a difference angle of approximately 9.2° between the ribs. This comparison is presented in Fig. 4.12, b). While the symmetric configuration exhibits many double eigenfrequencies, the grade of modal asymmetry is large in the optimized case. Figure 4.13, a) shows a top view on the brake disc with the cooling ribs in the best configuration found with the SQP algorithm and the corresponding, randomly generated starting configuration. Many ribs in the optimized configuration have a radius r_n either on the lower or upper bound. This can be seen in more detail in Fig. 4.13, b), where the radius r_n of each rib is plotted together with the angle φ_n. Also, the upper and lower bounds for the radius are given in the figure as dashed, green lines. Since the lower and upper bounds of the radius are induced by physical necessities, it is not possible to relax these bounds to

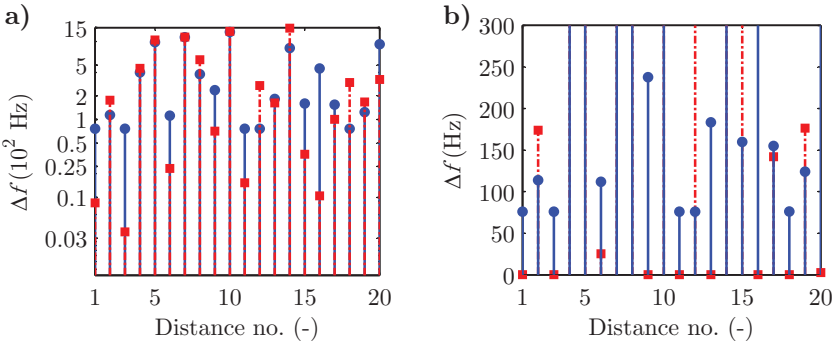

Figure 4.12: a) Distances between the first 21 eigenfrequencies of the best solution (solid, blue line, circular markers) and its starting configuration (dashed, red line, square markers). The y-axis is in logarithmic scale. b) Distances between the first 21 eigenfrequencies of the best solution (solid, blue line, circular markers) and a symmetric reference configuration (dashed, red line, square markers).

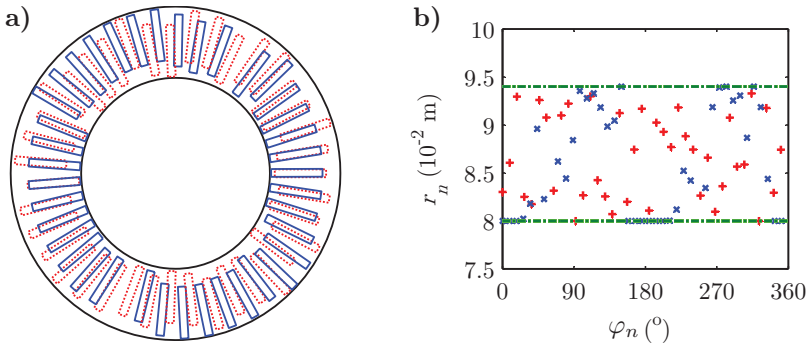

Figure 4.13: a) Rib configuration of the best optimized result (solid, blue line) and its starting configuration (dashed, red line). b) Plot of the radius r_n and the angle φ_n of each cooling rib for the best configuration (blue x) and the starting configuration (red +).

achieve an even better local optimum. The SQP approach leads to very satisfying results, as has been shown, nevertheless it exhibits two drawbacks. The first is that it is based on the calculation of gradients of the objective function and of the nonlinear constraints, which is less effective with the EMM used to

model the brake disc. The second is the fact that only 35% of all optimization approaches led to satisfying results, which is a rather low percentage, even if the nonlinearity and nonconvexity of the problem are considered.

As a second approach to solve the problem, the use of a heuristic GA is proposed, provided in the MATLAB Global Optimization Toolbox. For the initial population, 200 random distributions of cooling ribs were generated. The algorithm's stopping criterion was chosen to be a minimal change in the objective function of 10^{-14}. The further settings of the algorithms were chosen such that the linear constraints and upper and lower bounds are always fulfilled during the optimization. Also, the fraction of individuals performing crossover (generation of children from the parent generation without mutation) was set to 60%. The algorithm took 6 generations and approx. 28000 function evaluations to reach an optimum solution with a minimal split between the eigenfrequencies of 60.2 Hz, which is satisfying. Figure 4.14, a) shows the evolution of the minimal distance between the 21 considered eigenfrequencies during the optimization with the GA. It can be seen that in each genera-

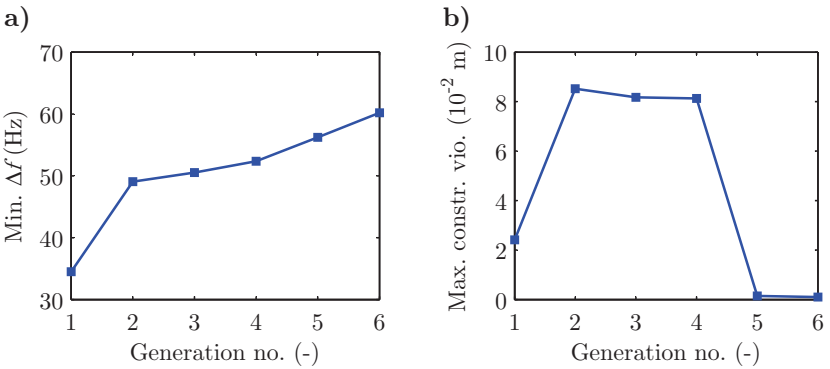

Figure 4.14: a) Evolution of the minimal distance Δf between the eigenfrequencies. b) Evolution of the maximum absolute constraint violation.

tion the objective function increases, which could be considered as unusual for genetic algorithms. The development of the maximum absolute violation of the constraints is documented in Fig. 4.14, b). First, the violation increases,

then stays constant and then abruptly diminishes to a feasible value, which hints at the heuristic characteristic of the approach. The rib configuration of the solution is shown in Fig. 4.15, a) together with the rib configuration of the best solution calculated with the SQP approach. While many ribs of the SQP

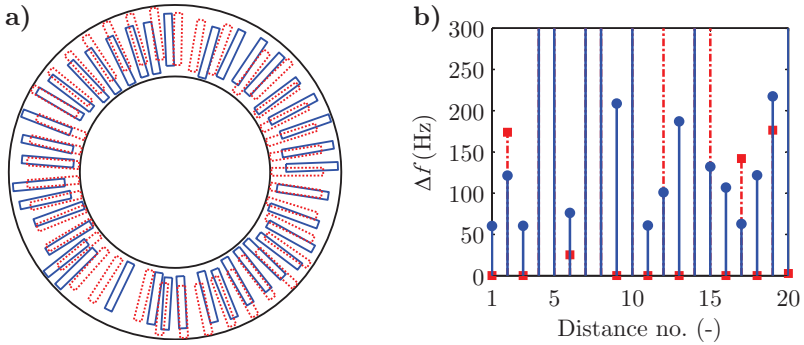

Figure 4.15: a) Rib configuration of the result optimized with the GA (solid, blue line) and the best SQP solution (dashed, red line). b) Distances between the 21 eigenfrequencies of the solution of the GA (solid, blue line, circular markers) and a symmetric reference configuration (dashed, red line, square markers).

solution are at the upper and lower bounds, this is not the case for the solution generated with the GA. The distances between the eigenfrequencies of the GA solution and for the symmetric reference configuration already introduced in the paragraph considering the SQP approach are presented in Fig. 4.15, b). They exhibit qualitatively a similar distribution as in the best case found with the SQP approach. Again, the large increase of modal asymmetry is obvious. The best solution of all approaches was achieved with one of the 20 SQP runs deterministically targeting a local optimum and not with the GA, which is conceived to target the global optimum due to its heuristic nature. This leads to the conclusion that for the presented nonlinear, nonconvex optimization problem, a deterministic approach is a good choice for achieving satisfying results, even under the expectation of many local optima [108].

Still, the GA has important advantages: It required approx. thrice as much function evaluations to reach its solution as one SQP run, however, it directly

led to a satisfying result, which the SQP approach only did in 35% of all approaches. Furthermore, the GA approach profits more from parallelization than the SQP approach (of course depending on the implementation) and is a gradient free method, which is beneficial when used in conjunction with the EM method of modeling the structure to be optimized.

Since the optimized configurations are intended to be used in a realistic context, they would have to be manufactured by a casting process. This process can lead to geometry variations due to manufacturing uncertainties. In order to assess their influence, the radii r_n and angles φ_n of the best SQP and GA solution are rounded to an assumed manufacturing precision of 0.001 m and 1°, respectively, similar to the case of the brake disc with radial holes. Figure 4.16 shows a comparison of the distances between the eigenfrequencies for the rounded configurations and the exact ones. As can be seen, the distances

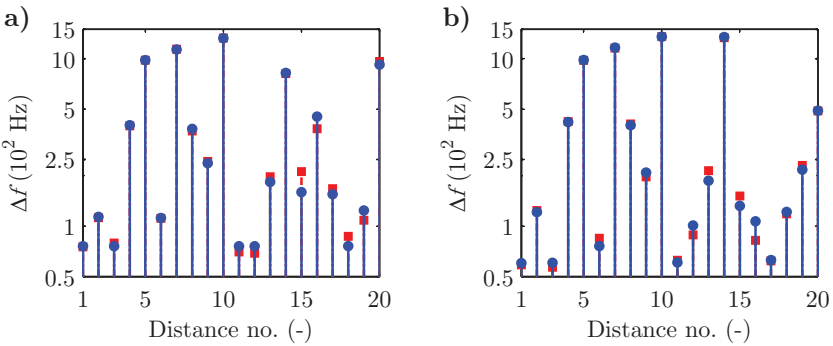

Figure 4.16: a) Distances between the 21 eigenfrequencies of the best rounded configuration found with the SQP approach (solid, blue line, circular markers) and the exact configuration (dashed, red line, square markers). The y-axis is in logarithmic scale. b) Distances between the 21 eigenfrequencies of the best rounded configuration found with the GA approach (solid, blue line, circular markers) and the exact configuration (dashed, red line, square markers). The y-axis is in logarithmic scale.

of the rounded configurations differ only slightly from the exact ones for both optimization approaches. A deviation of the minimal distance between the eigenfrequencies of 7.7 % in the SQP case and 5.5 % in the GA case result

from the rounding process. This leads to the conclusion that both solutions can be treated as robust against manufacturing uncertainties and are therefore, from this point of view, highly suitable for the application in passenger cars.

Of course, the resistance against brake squeal is only one aspect when considering brake discs for series applications. Others, even more important ones are e.g. temperature endurance, fatigue and wear resistance or manufacturing costs. These aspects have not been considered here and would surely lead to changes in the designs when considered properly. It was, however, not the goal of this work to develop realistic brake discs directly applicable for series production. Still, the optimized designs would be suitable for the generation of prototypes for squeal tests similar to the tests performed with the disc with radial holes. Since the generation of such cast prototypes is elaborate and cost-intensive, no prototypes were generated. It is more convenient and similarly significant to test bicycle brake discs and therefore, these have been optimized as well. This optimization and the results will be presented in the next sections.

4.4 Introductory example of a bicycle brake disc optimization

In order to give a first insight into the optimization of bicycle brake discs and to highlight similarities and differences to the automotive case, a first example of the optimization of a bicycle brake disc is shown. It was first published in [126]. The angular position φ_n and radial position r_n of the holes in the friction ring is varied here, as is presented in Fig. 3.11, b). The optimization problem to split the eigenfrequencies of the brake disc under variation of N

parameters r_n and φ_n is then formulated as

$$\begin{aligned}
&\max_{r_n,\varphi_n} \quad \min_k \ |f_{k+1} - f_k| \\
&\text{s.t.} \\
&r_{\min} \le r_n \le r_{\max} \\
&0 \le \varphi_n \le 2\pi \\
&\varphi_1 < \varphi_2 < \ldots < \varphi_N \\
&\mathbf{c}^{\mathrm{eq}}(r_n, \varphi_n) = \mathbf{0} \ \ (2 \ \text{ balance constraints}) \\
&\mathbf{c}(r_n, \varphi_n) \le \mathbf{0} \ \ (N \ \text{ min. distance constraints}),
\end{aligned} \tag{4.11}$$

where f_k are the eigenfrequencies of the disc and $r_{\min}$ and $r_{\max}$ are the minimal and maximal radii to the midpoints of the inserted holes, respectively. The balance constraints $\mathbf{c}^{\mathrm{eq}}$ can be easily deduced since the rotor is assumed to be a homogeneous body rotating at a constant angular velocity and the holes are of a constant diameter leading to

$$\begin{aligned}
c_1^{\mathrm{eq}}(r_n, \varphi_n) &= \textstyle\sum_{n=1}^{N} r_n \cos\varphi_n, \\
c_2^{\mathrm{eq}}(r_n, \varphi_n) &= \textstyle\sum_{n=1}^{N} r_n \sin\varphi_n.
\end{aligned} \tag{4.12}$$

They originate from the fact that in rotor dynamics balance is a crucial requirement. Since an intersection between holes has to be avoided and a minimal distance between two holes is necessary due to material strength requirements, minimal distance constraints $\mathbf{c}$ have to be introduced. They can be written as

$$c_n(r_n, \varphi_n) = d_{\min} - d_n^b, \tag{4.13}$$

where $d_{\min}$ is the minimal necessary distance between the midpoints of two holes and d_n^b is the actual distance between two holes given by

$$d_n^b = \sqrt{(r_{n+1}\cos\varphi_{n+1} - r_n\cos\varphi_n)^2 + (r_{n+1}\sin\varphi_{n+1} - r_n\sin\varphi_n)^2}. \tag{4.14}$$

As in the case of the automotive brake disc with radial holes, the minimal distance constraints cannot be written in linear form without major simplifications.

The presented nonlinear, nonconvex optimization problem was solved using the SQP algorithm implemented in the MATLAB Optimization Toolbox with

$E = 206000$ MPa	$h = 0.002$ m
$\nu = 0.3$	$r_h = 0.00225$ m
$\rho = 7850$ kg/m^3	$r_{\min} = 0.0715$ m
$r_i = 0.067$ m	$r_{\max} = 0.0755$ m
$r_a = 0.08$ m	$d_{\min} = 0.008$ m

Table 4.8: Parameters for the introductory bicycle brake disc optimization.

the parameters given in Tab. 4.8. Both FE meshes used for the rotor and the holes consist of 3D isoparametric elements of quadratic shape function order (C3D20) with 40800 DOF in the plate mesh and 12609 DOF in the hole mesh fulfilling convergence requirements. Also for convergence reasons, the parameter κ was chosen to be 10^{-6} (see Eq. 3.26). The disc's boundary conditions were selected as free at the inner and outer radius, in order to optimize the bending dominated eigenmodes in this introductory example. 36 regularly spaced holes were considered in the initial configuration exhibiting a cyclic symmetry, which can be seen in 4.17, a). The resulting configuration

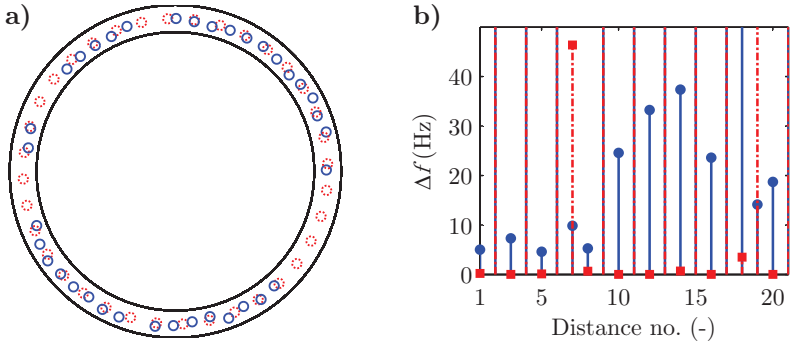

Figure 4.17: a) Brake rotor with a symmetric (dashed, red line) and the optimized hole configuration (solid, blue line). b) The distances between the first 22 eigenfrequencies of the optimized configuration (solid, blue line, circular markers) and the starting configuration (dashed, red line, square markers).

after the optimization, which took 7 iterations with 623 evaluations of the

objective function, is also presented in Fig. 4.17, a). The first 22 non-zero eigenfrequencies reaching up to 5 kHz were considered in the optimization.

This limit lies well below the frequency which can be calculated using Eq. (2.22) and was chosen for two reasons. First, as will be presented in the following, the increase in the grade of modal asymmetry was very low and it would be very likely that it decreases even more with more eigenfrequencies considered. Second, the runtime for this first bicycle brake disc optimization example could be kept low by limiting the number of computed eigenfrequencies. The distances between the eigenfrequencies of the optimized configuration and the starting configuration are shown in Fig. 4.17, b). While the initial configuration exhibits many double eigenfrequencies, a maximum minimum distance between the eigenfrequencies of 4.6 Hz was achieved as a local optimum. However, this grade of modal asymmetry is approximately a magnitude below the value necessary to avoid squeal completely (see section 2.2.3). It is highly unlikely that the usage of heuristic algorithms or the generation of many starting configurations to enhance the possibility of finding better optima would increase the achievable grade of modal asymmetry largely. Therefore, two important conclusions can be drawn from this introductory bicycle brake disc optimization. The first is that it is necessary to change the geometry to a far larger extent than was the case presented here and also in the automotive case in order to reach the potential to avoid squeal completely. The second is that it has to be assessed whether even grades of modal asymmetry below the limit of complete squeal avoidance can have beneficial effects on the performance of optimized brake discs in the squeal context. Both aspects will be considered in the next section, which deals with the optimization of a bicycle brake disc with a realistic geometry.

4.5 Bicycle brake disc with a realistic geometry

Bicycle brake discs have to fulfill many important criteria for save operation, in direct analogy to automotive brake discs. These reach from the provision of brake torque even under very high thermal loads to wear resistance. Additionally, lightweight construction and optical design aspects are far more

important than in the automotive case. This leads to a very complex and sophisticated geometry, as can be seen in Fig. 4.18, where a MAGURA Storm SL brake rotor is shown. MAGURA is a major German manufacturer of bi-

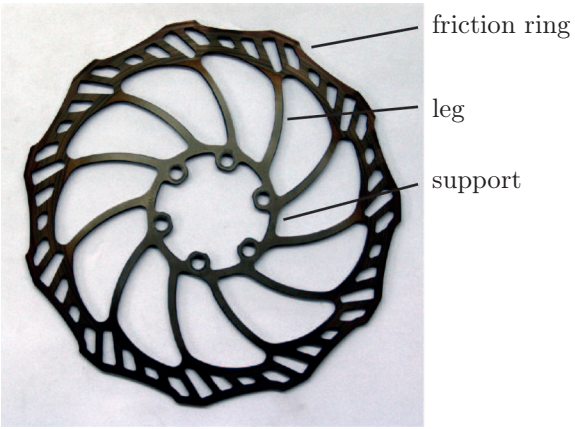

Figure 4.18: MAGURA Storm SL brake rotor.

cycle brake systems and the Storm SL is one of their commercially available, very light rotors. It is manufactured of stainless X30Cr13 steel offering a high hardness and wear resistance. While the friction ring is connected to the support by curved legs, six bolts connect the support with the hub at the bicycle. The outer and inner rim of the friction ring is curved as well and cut-outs reduce its weight. These geometrical elements present in state-of-the-art brake discs will be varied and optimized in the following to achieve higher grades of modal asymmetry as in the simple case shown in the section before. Large parts of this optimization have been conducted in the Master thesis [11].

4.5.1 Optimization problem

The optimization problem to increase the distance between the eigenfrequencies of the brake disc in a defined frequency range can be written as

$$\begin{aligned} &\max_{\mathbf{p}} \ \min_{k} \ |f_{k+1} - f_k| \\ &\text{s.t.} \\ &c^{\text{eq}}(\mathbf{p}) = 0 \\ &\mathbf{c}(\mathbf{p}) \leq \mathbf{0}, \end{aligned} \tag{4.15}$$

where the parameters to be varied are given by

$$\mathbf{p} = (\mathbf{b}^l,\, \varphi^l,\, \mathbf{r}^h,\, \mathbf{b}^h,\, \varphi^h,\, \gamma^r,\, \mathbf{a}^r,\, \varphi^r)^{\mathrm{T}}. \tag{4.16}$$

Figure 4.19 introduces these parameters in more detail. The optimization

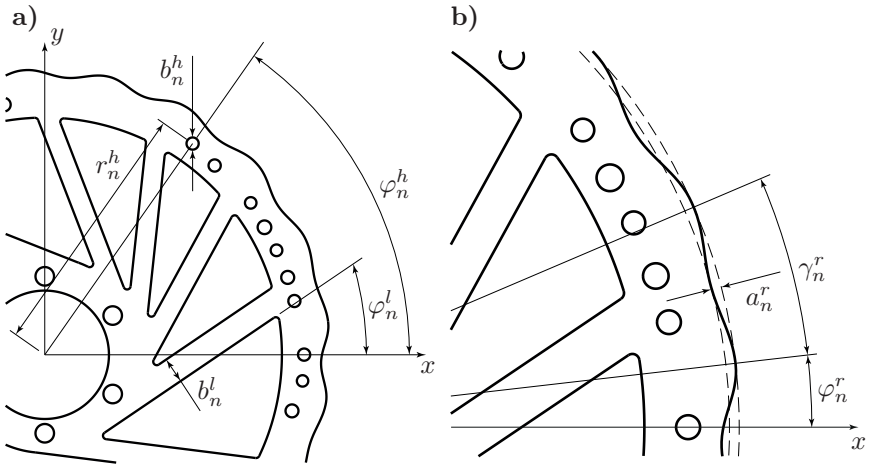

Figure 4.19: a) Section of a top view on a brake disc to be optimized. b) More detailed section of the top view to highlight the optimization variables varying the rim of the friction ring.

parameters are: the width b_n^l and angle φ_n^l of the legs connecting the support and the friction ring, the radius r_n^h to and angle φ_n^h of each hole on the friction ring and its diameter b_n^h and also the parameters γ_n^r, a_n^r and φ_n^r used to vary

the outer rim of the friction ring. The inner rim of the friction ring is not varied. Also, the legs are not curved for the optimization presented here and there are only holes in the friction rings considered and no cut-outs of other form. The number of legs N^l and the number of holes N^h in the friction ring are kept constant during the optimization. The outer rim of the friction rim is parameterized such that it can exhibit a wave form. This is introduced by cosine waves, which cover an angle γ_n^r, begin at an angle φ_n^r and have an amplitude a_n^r. The single waves are connected such that a continuous wave is generated as is shown in Fig. 4.19, b). The maximum penetration depth of each wave is counted from the outer rim (which has a constant radius r_a) and has a magnitude of a_n^r. Since the number of single waves N^r is constant during the optimization, the parameter $\gamma = f(\varphi_n^r, N^r)$ is a function of the angle φ_n^r and the number of single waves N^r, a relationship that can be used to reduce the number of variables in the optimization.

The upper and lower bounds of the optimization variables are given by

$$\begin{aligned}
&b^l_{\min} \leq b^l_n \leq b^l_{\max},\\
&0 \leq \varphi^l_n \leq 2\pi,\\
&r^h_{\min} \leq r^h_n \leq r^h_{\max},\\
&b^h_{\min} \leq b^h_n \leq b^h_{\max},\\
&0 \leq \varphi^h_n \leq 2\pi,\\
&a^r_{\min} \leq a^r_n \leq a^r_{\max},\\
&0 \leq \varphi^r_n \leq 2\pi.
\end{aligned} \tag{4.17}$$

Further inequality constraints are

$$\begin{aligned}
&\varphi^l_n - \varphi^l_{n+1} \leq -\Delta\varphi^l_{\min},\\
&\varphi^l_{n+1} - \varphi^l_n \leq \Delta\varphi^l_{\max},
\end{aligned} \tag{4.18}$$

representing the minimal and maximal distance constraints for the legs, where $\Delta\varphi^l_{\min}$ is the minimal angle between two legs and $\Delta\varphi^l_{\max}$ the maximum one. Additionally, a minimal distance $d_{\min}$ between the outer rims of the holes in the friction ring is introduced in direct analogy to the introductory example (see Eqs. (4.13) and (4.14)) considering the variable hole radius in this case.

The balance constraint $c^{\mathrm{eq}}(\mathbf{p})$ has a very simple form

$$c^{\mathrm{eq}}(\mathbf{p}) = e(\mathbf{p}), \tag{4.19}$$

where $e(\mathbf{p})$ is the eccentricity of the brake disc resulting from the design elements that are varied. It is not considered as useful to derive this balance constraint explicitly as has been done in the optimization approaches presented before, due to the complex geometry of the bicycle brake discs. Instead, it is evaluated numerically with the FE package used to generate and analyze the model (see below). Again, dynamical balance is assured by this constraint as well.

While many parameters of the brake rotor are varied during the optimization, Fig. 4.20 shows the parameters kept constant. These are the outer radius

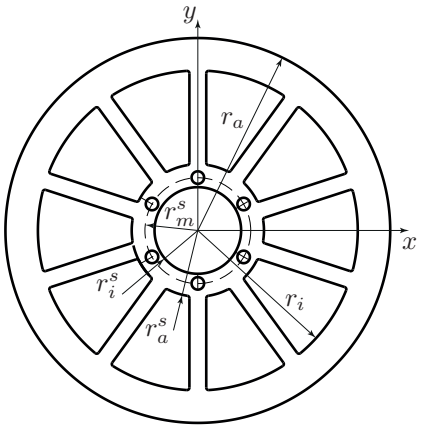

Figure 4.20: Top view on a brake disc with very simple geometry that will later be used as a reference example.

of the friction ring r_a, its inner radius r_i, the inner radius of the support r_i^s and its outer radius r_a^s. Six holes of 5.2 mm diameter are placed evenly spaced in the middle of the support ring at $r_m^s = 22\,\mathrm{mm}$ to allow for a proper fixation to the hub of the wheel. The disc has a thickness of h, which is also kept constant. There are composite brake discs commercially available, however, here the brake discs are considered to be of a single material with a

density ρ, YOUNG's modulus E and POISSON's ratio ν, as was the case for the introductory example.

4.5.2 Modeling aspects

In all cases presented before in this thesis, the EMM has been used to model the structure to be optimized offering the possibility to combine efficiency and large geometry variations. This method offers large advantages if the modifications of the basis structure are rather simple in their geometry. This was the case for the automotive brake discs with radial holes and cooling channels as well as for the bicycle disc case with modifications only of the holes in the friction ring. The EMM is not ideally suited to model the complex geometry of the bicycle brake discs considered in this section. Therefore, a more basic approach was chosen. The geometry is directly modeled in the commercial FE package ABAQUS using a PYTHON script and the parameters introduced in paragraph 4.5.1 can be varied by an external optimization algorithm accessing this script. This has the advantage that also large changes in the geometry are possible and that the optimization algorithms can be chosen freely that are combined with the FE software. The disadvantage is that the structure has to be remeshed in every iteration step of the algorithm. ABAQUS can generate FE meshes automatically, solves the eigenvalue problem necessary for the determination of the objective function efficiently and also allows for the computation of the eccentricity of the brake rotor. Therefore, it is a very good modeling tool for the purposes necessary here, despite the fact that it does not offer very capable optimization algorithms leading to a preference for external algorithms.

The FE mesh has been generated using shell elements with quadratic shape function order (S8R), where the characteristic side length determining the amount of DOF used for the mesh during the automatic mesh generation process was chosen to be $0.8h$ fulfilling convergence requirements. This leads to approximately 5000 elements and 100000 DOF in the models during the optimization. In Tab. 4.9 the parameters used in the optimization presented in the next section are shown. The boundary conditions for the disc are chosen

$E = 210000$ MPa	$h = 0.002$ m
$\nu = 0.3$	$r_p = 0.0735$ m
$\rho = 7850$ kg/m^3	$\mu = 0.4$
$r_i = 0.0665$ m	$k = 1.2 \cdot 10^5$ N/m
$r_a = 0.08$ m	$m_G^{\min} = 0.035$ kg
$r_a^s = 0.0275$ m	$\alpha_M = 0.092$ s
$r_i^s = 0.018$ m	$\alpha_S = 1 \cdot 10^{-10}$ 1/s

Table 4.9: Parameters of the bicycle brake discs with complex geometry.

as following: The outer rim of the disc is assumed to be free, while the rims of the six holes on the support are assumed to be clamped, which is defined as setting the displacement DOF and rotational DOF to zero in the nodes at the rim. It will be shown in section 4.5.4 that this allows for a very good match between simulations and experiments.

4.5.3 Solution of the optimization problem

The optimization problem was solved using a tripartite approach based on the knowledge gained from the optimization of the automotive brake discs with cooling channels. This approach has been introduced shortly in Fig. 4.1. The main optimization is a continuous one varying the parameters introduced in section 4.5.1. For the solution a GA implementation provided by the MATLAB Global Optimization Toolbox was used. The initial configurations are generated randomly and then pre-optimized by a simplified discrete optimization explained in the following. After the genetic algorithm is finished, a SQP approach follows with the intention to further enhance the found solution if possible. The settings for the upper and lower bounds of the optimization parameters and the constraints can be found in Tab. 4.10. The number of legs N^l, holes N^h and single waves at the outer radius N^r are kept constant for one optimization approach, however, three approaches will be conducted with variations in these numbers. Additionally, the angle γ_n^r of one single wave at the outer rim can vary up to 20% from the average value $\gamma_{\text{av}}^r = 360°/N^r$.

$b^l_{\min} = 0.005$ m	$a^r_{\min} = 0$ m
$b^l_{\max} = 0.008$ m	$a^r_{\max} = 0.003$ m
$\Delta\varphi^l_{\min} = 4^{\circ}$	$d_{\min} = 0.002$ m
$\Delta\varphi^l_{\max} = 60^{\circ}$	$e_{\text{vio}} = 0.0005$ m
$r^h_{\min} = 0.0705$ m	$N^l = 8 - 14$
$r^h_{\max} = 0.073$ m	$N^h = 25 - 60$
$b^h_{\min} = 0.003$ m	$N^r = 0 - 21$
$b^h_{\max} = 0.005$ m	

Table 4.10: Settings for the optimization of the realistic bicycle brake discs.

The optimization goal is to introduce a split of 43 Hz between the eigenfrequencies of the brake disc up to 6 kHz. It is know from the estimation presented in section 2.2.3 using the parameters of Tab. 4.9 that the discs can squeal up to a higher frequency. However, it will be shown in the next section that the modal analysis tests to check the validity of the optimization results could only be conducted up to 6 kHz leading to the limiting of the optimization frequency to 6 kHz, which corresponds to 34 eigenfrequencies to be considered. For the main optimization and the following SQP approach, the constraint tolerance was set to 0.0001 rad for angle and 0.1 mm for length measures, except for the tolerance in the balance constraints, which was set to 0.5 mm. The continuous optimizations were stopped if the change in the objective function between two consecutive optimization iterations were below 10^{-5}, the absolute value of the step size below 10^{-8} and the constraints were satisfied to the limits given above. Additionally, the GA was stopped in the continuous case if in three consecutive generations no enhancement of the objective function could be reached and in the discrete case after five. In order to guarantee a steady increase in the objective function also for the genetic algorithms, one elite member of each generation is chosen that is directly transferred to the next generation. For the starting population, 150 initial configurations were generated using a discrete genetic algorithm.

While in the continuous case, design elements of the brake discs and their

position are varied continuously, in the discrete case, the basic geometry of the rotor is fixed and legs and holes in the friction ring are enabled or disabled. This is demonstrated in Fig. 4.21. The outer rim of the friction ring is not

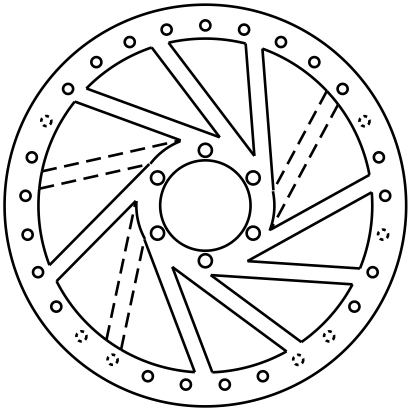

Figure 4.21: Top view on a brake disc with fixed geometry and disabled (dashed line) or enabled (solid line) design elements.

varied here and also the width of the legs is fixed to $b_n^l = 6.5$ mm and the diameter of the holes to $b_n^h = 4$ mm. The maximum number of legs and holes is given by 14 and 60, respectively, fulfilling the minimal distance constraints presented in section 4.5.1. The maximal distance constrains are converted to constraints that determine the maximum number of consecutively disabled legs and holes. The reduction of the continuous optimization problem to a discrete one additionally requires a relaxation of the balance constraint tolerance, which has been set to $e_{\text{vio}} = 10$ mm.

Making use of the discrete GA, three brake disc configurations with an increasing level of flexibility in the design were generated, additionally two reference samples. They differ in the following aspects, summarized in Tab. 4.11: The legs were fixed or variable, there were holes in the friction ring or not and the outer rim was changed to accomplish a wave form or not. The models I and II have fixed design aspects, are not optimized and will be used as reference examples. The other three models were optimized with the ap-

Model	Legs		Holes		Outer rim	
	fixed	variable	none	variable	fixed	variable
I	X		X		X	
II	X		X		X	
III		X	X		X	
IV		X		X	X	
V		X		X		X

Table 4.11: Model variations of the bicycle brake rotor forming the basis for three optimization approaches with increasing flexibility in the geometry and two reference configurations (I and II).

proach presented before. The complete runtime of the algorithms from the generation of starting configurations to the enhancement of the found local optimum with a SQP approach took approximately 2 weeks each, dominated by the successive solution of the eigenvalue problem to determine the objective function and its derivatives (the latter only in the SQP case). Figure 4.22 shows top views on the three optimized discs and the two reference configurations. Additionally, the MAGURA Storm SL rotor is shown highlighting the similarities and differences between the optimized rotors and the commercially available one. While models I and II exhibit a cyclic symmetry leading to many double eigenfrequencies, the three optimized discs are geometrical and modal asymmetric. This will be discussed in detail in the next section together with modal and squeal test results.

4.5.4 Results

The five brake discs presented in Tab. 4.11 were manufactured by water jet cutting from X20Cr13 steel, which is a stainless steel equivalent to the material of which the MAGURA Storm SL is made of. These prototypes were then tested on a bicycle test rig shown in Fig. 4.23. The test rig consists of a commercially available bicycle front fork rigidly connected to a heavy support. The wheel and the brake are attached to the fork as is usual for a conventional bicycle.

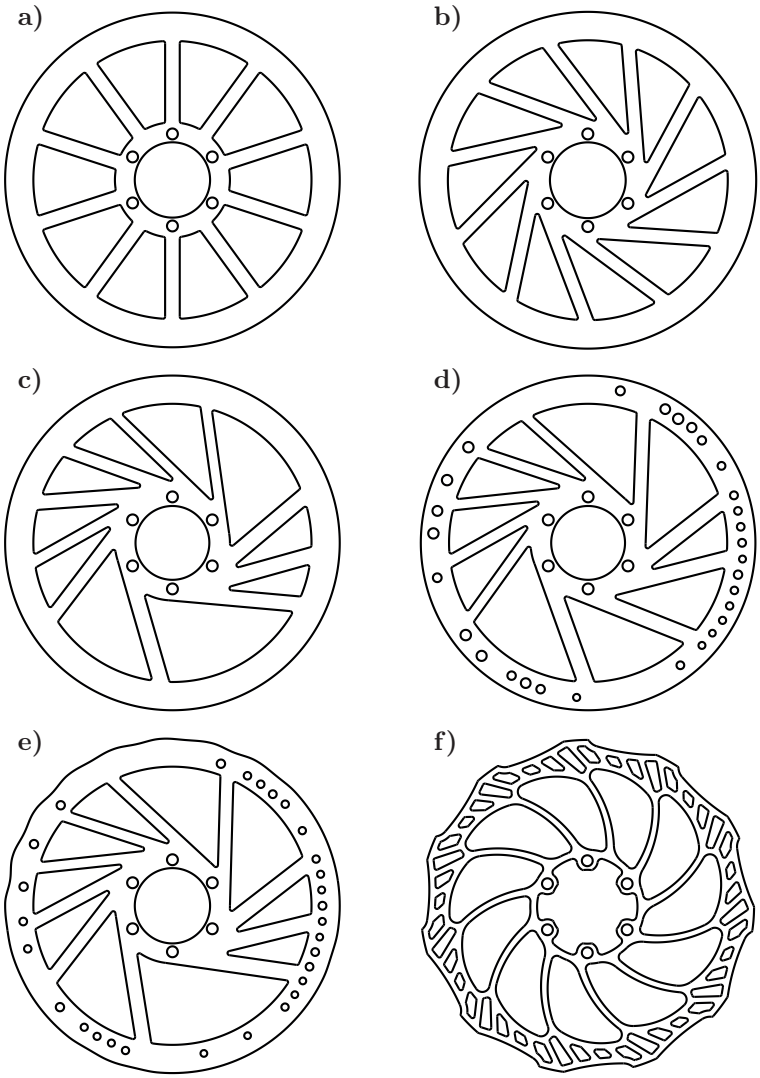

Figure 4.22: Top views on: a) model I, b) model II, c) model III, d) model IV, e) model V and f) the Magura Storm SL.

Figure 4.23: The bicycle brake test rig.

The brake system used for the tests is a MAGURA MT4 model suitable for brake rotors of 160 mm diameter. The wheel can be driven by a controlled electrical motor, which enables measurements at different combinations of brake pressure and rotational frequencies of the disc. This is essential for squeal tests.

A modal analysis with the non-rotating disc was conducted first, using the same techniques and the same POLYTEC scanning laser vibrometer as for the tests of the automotive disc with radial holes. A sampling frequency of 16.38 kHz was used and the spectrum was evaluated up to 6.4 kHz with a resolution of 1 Hz. A grid with about 80 measurement points was used and an averaging process over ten measurements per point helps to increase the reliability of the modal analysis. The results of this analysis are compared to the calculation results to assess the validity of the brake disc model used for the optimization and the grade of modal asymmetry achieved by it. Afterwards, squeal tests were performed with rotating wheel to evaluate the squeal affinity of the tested brake discs, also in direct analogy to the test performed with the automotive disc with radial holes. For the squeal test measurements the sampling frequency was selected to be 32 kHz, however, the generated spectra were only evaluated up to 12.5 kHz using a low-pass-filter. After each squeal

test at a given pressure and rotational frequency, the surface temperature of the discs was measured, in order to avoid heating above 100° Celsius. Higher temperatures would strongly alter the properties of the brake pad and therefore the squeal affinity of the brake assembly. Additionally to the measurement of the surface velocity of the brake disc with a laser vibrometer, the average SPL was measured using a TROTEC BS15 sound-level-meter at a distance of 0.5 m from the brake disc. However, since no suitable room was available for the measurements and the sound-level-meter's precision is ± 3.5 dB(A), this can only give a very rough estimate of the generated noise level and therefore is not suitable for the assessment of a reduction in squeal affinity according to scientific standards. The measurements with the laser vibrometer will thus be used to decide about the performance of the optimized prototypes with respect to squeal and about the efficacy of the conducted optimization. Still, the SPL will be given to illustrate these findings more clearly.

First, the results for the Storm SL rotor will be presented in total in the next paragraph, before the modal analysis results of the prototypes are shown. Then follows a comparison of the squeal test results of the prototypes, before the squeal reduction performance will finally be assessed by a comparison of the best optimized prototype and the commercially available MAGURA rotor.

Introductory Example: The MAGURA Storm SL

As has been addressed in the last paragraph, the Storm SL, shown in Fig. 4.18, exhibits a cyclic symmetry, leading to an expectation of many double eigenfrequencies or eigenfrequencies which are hardly separated. This is shown by a plot of the distances between the eigenfrequencies of this rotor, given in Fig. 4.24, a), which have been calculated using ABAQUS with the settings presented in section 4.5.2. The first 70 eigenfrequencies, shown in Fig. 4.24, b), were considered in the calculations reaching up to about 12 kHz. This limit lies far above the highest frequency measurable in the modal analysis. This is due to the fact that the modal hammer used to test the very light brake disc could not excite modes up to this high level even with a steel tip. The normalized spectrum of the hammer is introduced in

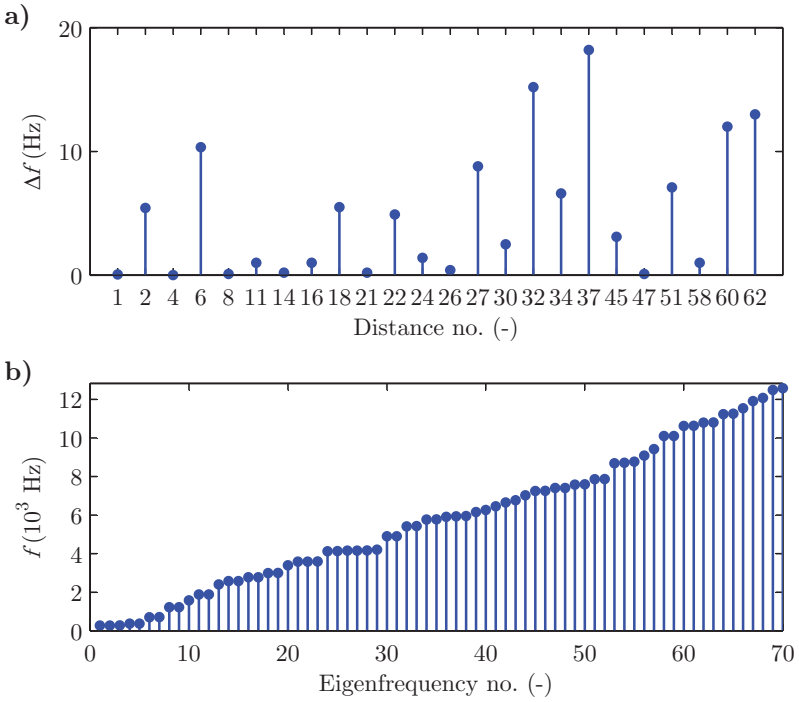

Figure 4.24: a) Distances Δf between the eigenfrequencies of the MAGURA Storm SL brake disc. Only the distances below 20 Hz are shown, the corresponding number of the eigenfrequency pair is given on the x-axis. b) Calculated eigenfrequency distribution of this rotor.

Fig. 4.25, a) and it can be seen that the excitation level rapidly decreases with increasing frequency. The -10 dB limit lies even below 2 kHz. Despite this fact, the spectrum of the velocity signal of the laser vibrometer could be evaluated reliably up to 6 kHz, since the coherence at the eigenfrequencies is close to 1 up to this limit, as can be seen in Fig. 4.25, b). The eigenfrequencies of the brake rotor could be determined analyzing the spectrum of the laser vibrometer's velocity signal shown in Fig. 4.25, c) in conjunction with the possibility to visualize the operating deflection shapes at defined frequencies. The measured eigenfrequencies that could be clearly identified are compared

to the calculated ones in Tab. 4.12. It can be seen that the agreement bet-

Eigenmode	f_i (C)	Δf_i (C)	f_i (M)	Δf_i (M)
1/0	269	0	267	0
	269		267	
2/0	371	0	375	0
	371		375	
3/0	696	10	702	12
	706		714	
4/0	1219	0	1232	0
	1219		1232	
5/0	1878	1	1897	0
	1879		1897	
6/0	2775	1	2793	6
	2776		2799	
7/0	3585	0	3603	11
	3585		3614	
8/0	4897	3	4958	7
	4900		4965	

Table 4.12: Eigenfrequencies f_i and corresponding distances between the eigenfrequencies Δf_i of the MAGURA Storm SL rotor. Calculations (C) and measurements (M).

ween measurements and simulation is very good. This also demonstrates that the choice of boundary conditions, which are a free outer rim of the disc and clamped rims of the six holes in the support, is correct. The distances between the measured eigenfrequencies is always at the same level or higher than between the calculated ones, which shows that not only the eigenfrequencies can be predicted accurately and usefully by the simulations but also the distances. Therefore, for the following modal analysis results, only the calculated distances between the eigenfrequencies will be given for the five prototypes. The measurement results are available but lead to the same conclusions than

in the case of the Storm SL rotor shown here and will thus not be given explicitly. Before, the squeal test results of the MAGURA disc are presented to complete the discussion on this brake disc type.

For squeal tests of the Storm SL rotor, the MAGURA brake pads type 7.3 were used. The rotational frequency was varied in discrete steps from 0.5 1/s to 2.25 1/s and the applied brake pressure from 1 bar to 10 bar. At each operational point in this test matrix, the surface velocity of the disc at a defined point was measured using the laser vibrometer. As an example, the spectrum of this signal for the operation point with a pressure of 3 bar and the rotational frequency 1.5 1/s is shown in Fig. 4.26. The most characteristic peak lies at 1025 Hz, there are some smaller ones at lower frequencies but not at higher ones. Concluding, the Storm SL squeals nearly monofrequently at 1025 Hz at this operation point, there are no higher harmonics of this frequency present. An analysis of the spectra of all other operation points shows the same behavior, where only the squealing frequency slighly varies from 1010 Hz to 1050 Hz due to varying temperatures of disc and pad. The maximum amplitude of the spectrum at each operation point is evaluated leading to the squeal map presented in Fig. 4.27, where the maximum amplitude of the spectrum of the velocity signal is shown as a color scale according to the operation point defined by the brake pressures given at the x-axis and the rotational frequencies at the y-axis. There are some operating points shown without color. At these points no reliable measurements where possible, either because the brake temperature increased too fast to achieve constant parameters or because the electrical motor could not maintain a constant rotational speed due to the high brake pressures applied. The maximum vibration amplitudes during squeal can reach 0.02 m/s leading to very high sound pressure levels of at least 82 dB(A), which is without doubt highly uncomfortable. Concluding, the measurements clearly demonstrate that the commercially available brake disc is not optimized to avoid squeal and is therefore highly prone to squeal. In the following, the modal analysis of the three optimized prototype discs and the two reference ones is shown before their squeal affinity is analyzed.

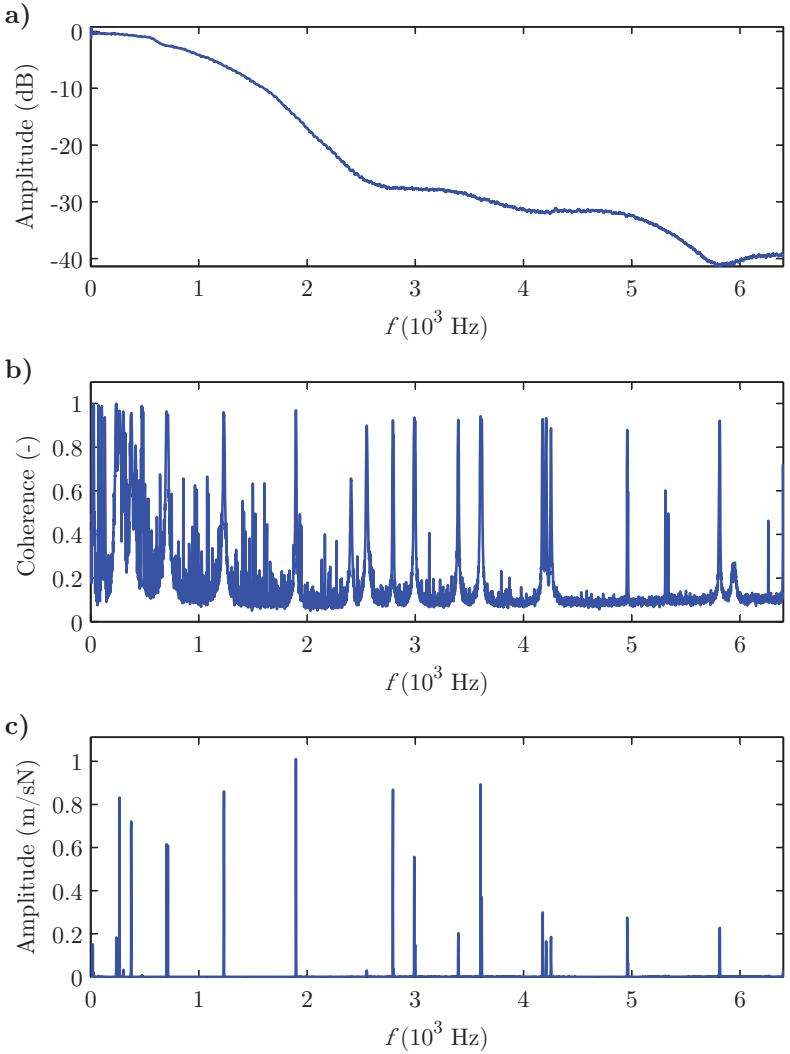

Figure 4.25: Magura Storm SL: a) Normalized spectrum of the force signal of the modal hammer. b) Coherence between the laser vibrometer's velocity signal and the force transducer's signal of the modal hammer. c) Transfer function between the velocity signal of the laser vibrometer and the force transducer signal of the modal hammer.

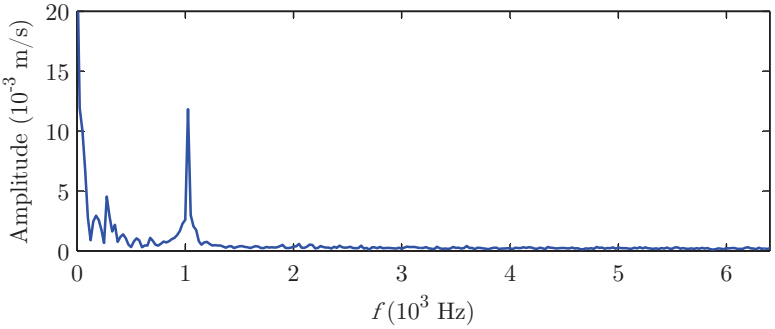

Figure 4.26: Spectrum of the surface velocity signal during squeal of the Storm SL rotor at a brake pressure of 3 bar and a rotational speed of 1.5 1/s.

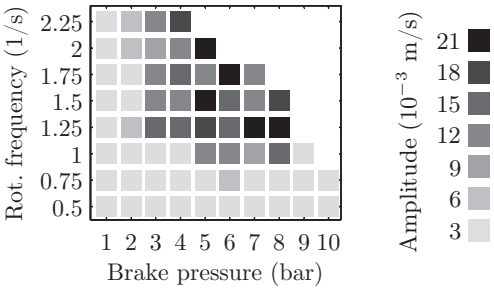

Figure 4.27: Squeal map of the Storm SL rotor. The corresponding squeal frequencies vary from 1010 Hz to 1050 Hz.

Modal analysis

Two prototype brake discs exhibiting a cyclic symmetry were manufactured with the intention to serve as reference examples for the tests with the other three prototypes. The first one, model I, shown in Fig. 4.22, a), has straight legs rectangularly connecting support and friction ring, while the second, more realistic one, model II, has legs fixed tangentially to the support, as is shown in Fig. 4.22, b). Due to their cyclic symmetry, both discs are expected to have a very low grade of modal asymmetry, which is verified from the computed distances between their eigenfrequencies presented in Fig. 4.28. As can be

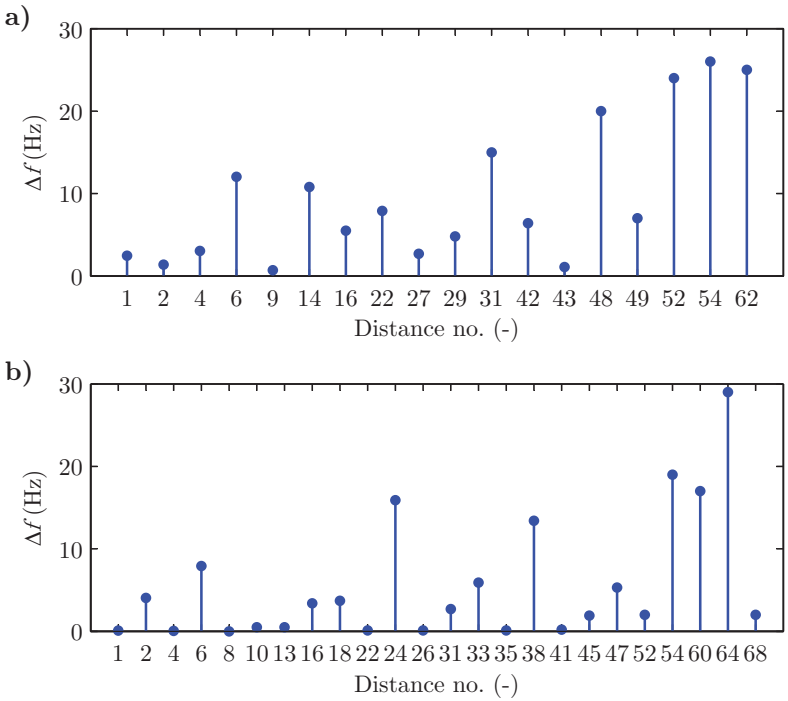

Figure 4.28: Distances Δf between the eigenfrequencies of disc model I (a)) and model II (b)). Only the distances below 30 Hz are shown, the corresponding number of the eigenfrequency pair is given on the x-axis.

seen, both discs have more than ten distances between the eigenfrequencies below 30 Hz in the range up to 12 kHz and some which have such a small distance between each other that they can be considered as double eigenfrequencies. Thus these discs are supposed to show a high squeal affinity, which will be demonstrated in the next section.

The distances between the eigenfrequencies of the three optimized brake discs are shown in Fig. 4.29. The discs have only been optimized up to 6 kHz and therefore a distinction is made in the plots between the optimized frequency range and the higher frequency range from 6 kHz to 12 kHz. The distances in the optimized frequency range are printed as solid, blue line with circular markers, while the distances in the higher frequency range are printed as dashed, red line with circular markers. Only the legs were varied to achieve model III, nevertheless, this model exhibits with 27 Hz the largest minimal difference between the eigenfrequencies in the optimized frequency range. Both more elaborate models IV and V have a smaller grade of modal asymmetry in this frequency range. This hints at the fact that the increase in the amount of optimization variables leads to a more complex optimization problem which makes the finding of better local solutions more difficult. Increasing the number of starting configurations in the initial population of the continuous GA could improve the possibility of finding a proper optimum, however, high calculation times put a limit on this approach. Still, model III exhibits one eigenfrequency pair with only a very small distance of 3 Hz in the higher, not optimized frequency range. As will be shown in the next paragraph, this leads to a higher squeal affinity at high frequencies. In this respect, model IV performs better than prototype V with a split of 18 Hz in the range between 6 kHz and 12 kHz compared to the split of 11 Hz. The higher grades of modal asymmetry of models IV and V result from the introduction of holes in the friction ring and waves at the outer rim of this ring which strongly affect high eigenfrequencies but have only a very limited effect on lower ones (see section 4.4). A comparison of the achieved distances between the eigenfrequencies of all six tested brake discs separately reported for the optimized frequency range and the higher frequencies is given in Tab. 4.13. This table sums up the results of the modal analysis presented in this section and emphasizes that

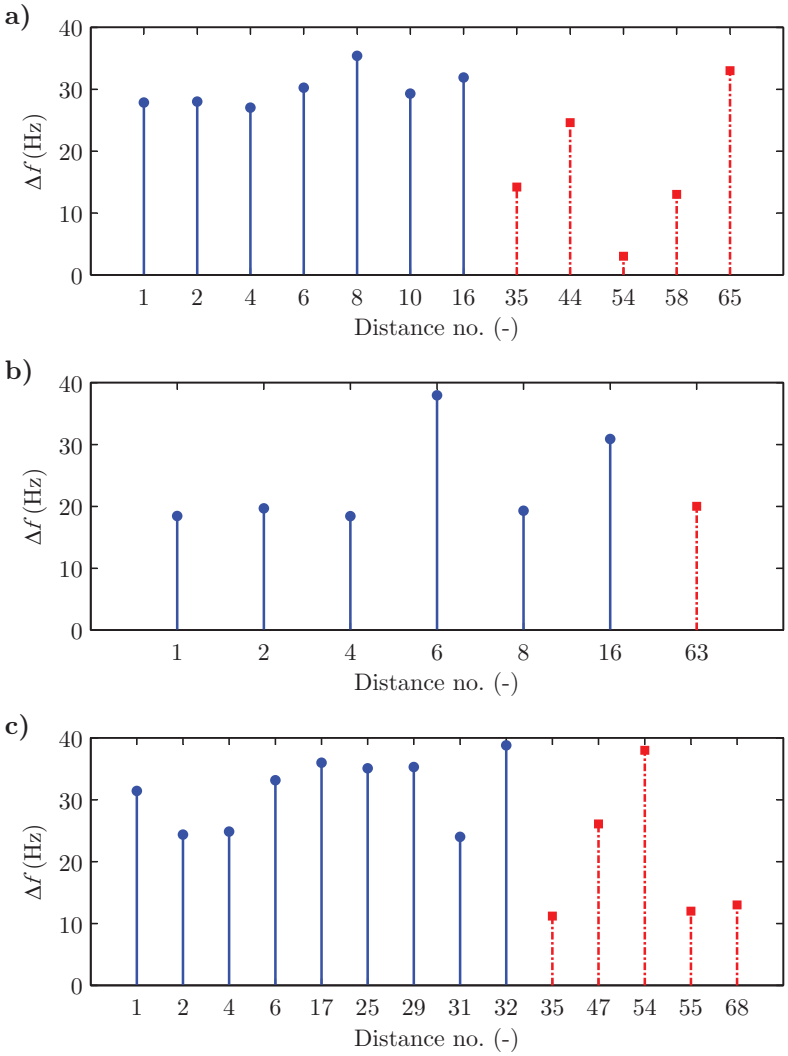

Figure 4.29: Distances Δf between the eigenfrequencies of disc model III (a)), model IV (b)) and model V (c)). Only the distances below 40 Hz are shown, the corresponding number of the eigenfrequency pair is given on the x-axis.

Model	Δf (Hz) (O)	f (Hz) (O)	Δf (Hz) (H)	f (Hz) (H)
Storm SL	0	371	0	7399
I	1	1327	1	9026
II	0	1311	0	6360
III	27	228	3	10475
IV	18	368	20	11871
V	24	5620	11	6372

Table 4.13: Maximal minimal distance Δf between the eigenfrequencies of the six tested brake discs with the corresponding lower eigenfrequency. Optimized frequency range (O) and higher frequency range between 6 kHz and 12 kHz (H).

the three not optimized discs have far lower grades of modal asymmetry than the optimized ones. This highlights the positive impact of the optimization, however, it should be noted that neither disc exhibits a distance between all eigenfrequencies in the critical frequency range that is needed to completely avoid squeal according to the estimations given in chapter 2.2.3. Still, it is shown in the squeal test section presented next that even an optimization, which could not introduce the necessary split between the eigenfrequencies to avoid squeal completely, leads to large benefits concerning squeal affinity.

Squeal tests

Applying the same procedure as with the Storm SL rotor, the five prototype discs were tested with respect to their squeal affinity. MAGURA brake pads type 7.1 were used in this case. The squeal frequencies of the prototypes lie in three frequency ranges and are present simultaneously, however, with strongly varying amplitudes. These frequency ranges are 260 Hz to 320 Hz, 350 Hz to 400 Hz and the much higher range 9000 Hz to 11000 Hz. The broad range of 9000 Hz to 11000 Hz indicates that the participating modes are not identical for the different brake discs, but they are similar with respect to the fact that the participating eigenmodes are of very high order with many nodal lines and therefore ensure comparability. The squeal maps of the low,

middle and high frequency range can be found in Figs. 4.30, 4.31 and 4.32.

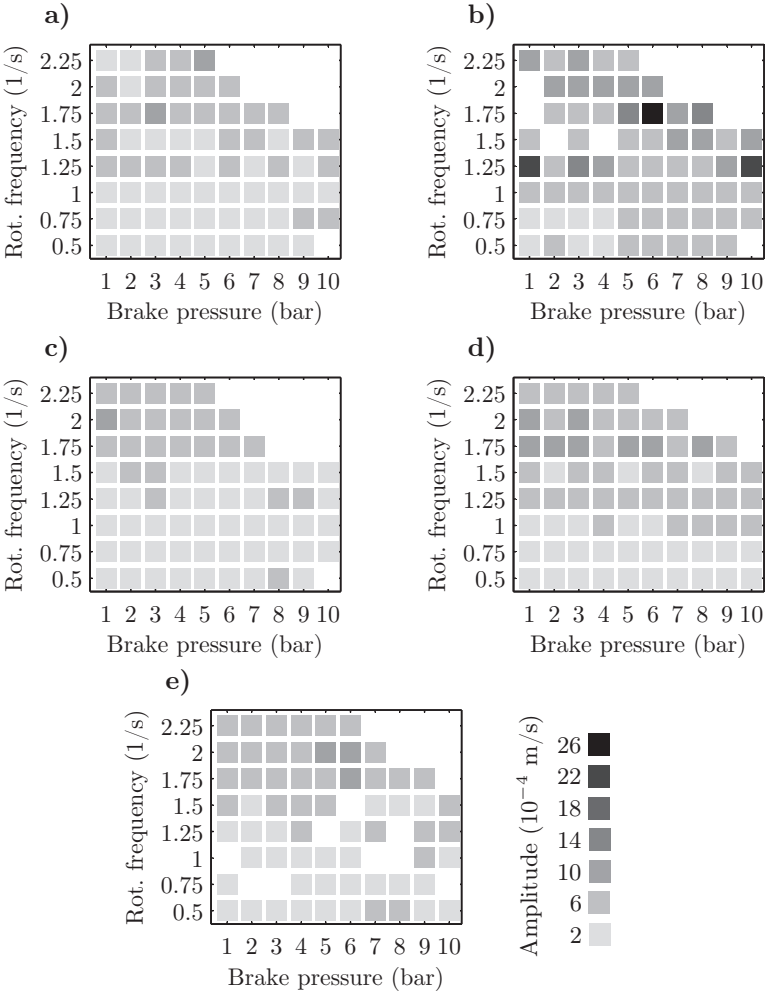

Figure 4.30: Squeal maps of the prototype rotors. The corresponding squeal frequencies vary from 260 Hz to 320 Hz. a) Model I, b) model II, c) model III, d) model IV and e) model V.

The squeal maps for the lowest frequency range given in Fig. 4.30 show that

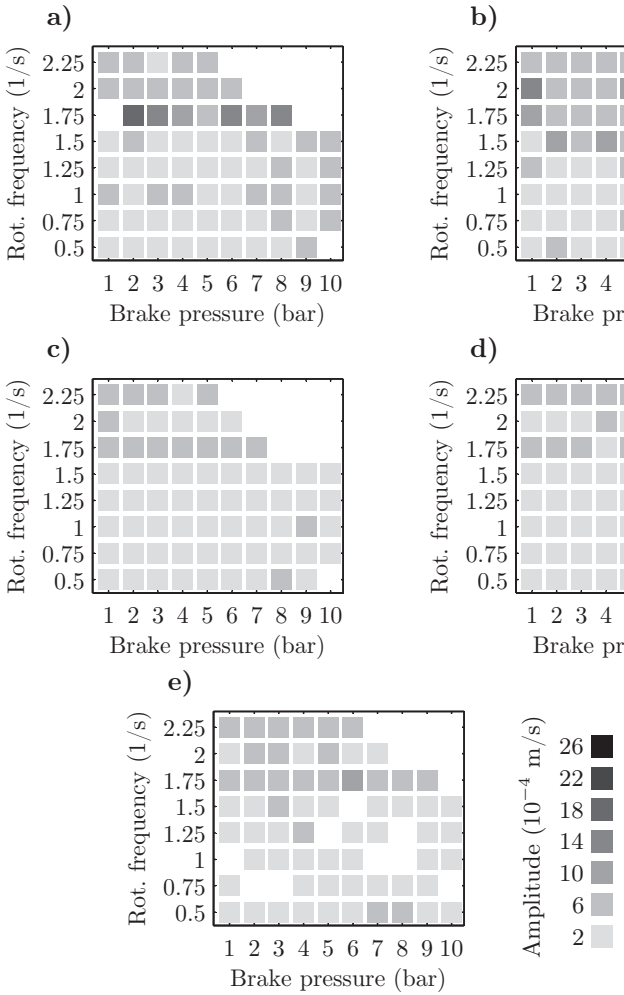

Figure 4.31: Squeal maps of the prototype rotors. The corresponding squeal frequencies vary from 350 Hz to 400 Hz. a) Model I, b) model II, c) model III, d) model IV and e) model V.

only model II exhibits high vibration amplitudes in this range despite the fact that also model I has eigenfrequencies with a very low distance. This

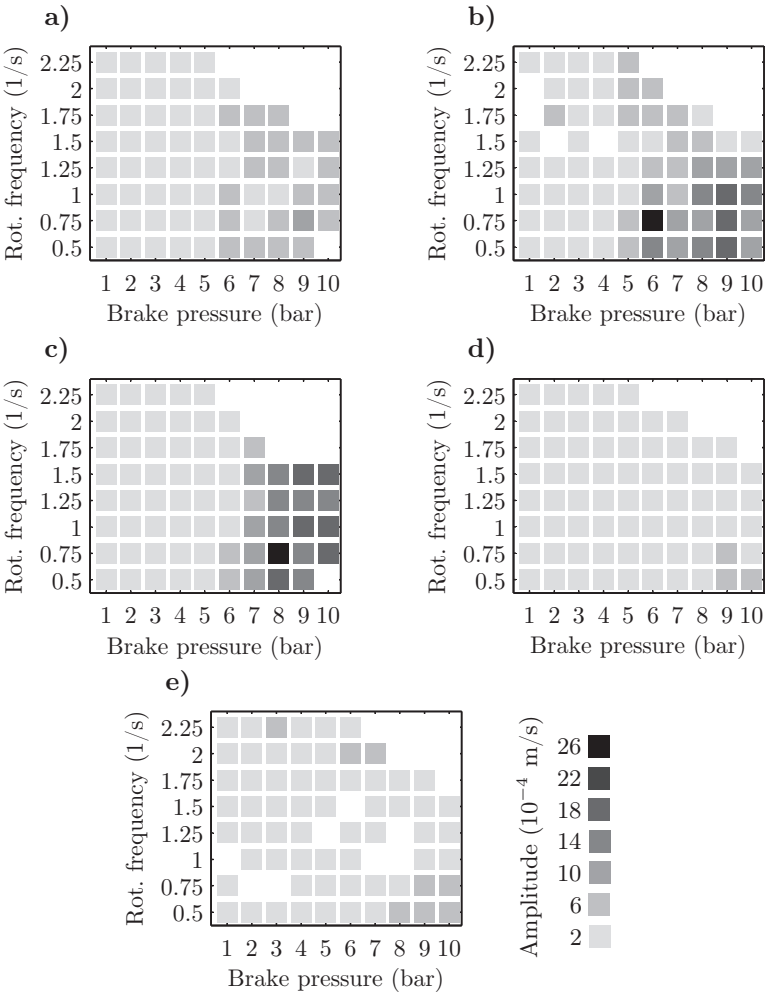

Figure 4.32: Squeal maps of the prototype rotors. The corresponding squeal frequencies vary from 9 kHz to 11 kHz. a) Model I, b) model II, c) model III, d) model IV and e) model V.

supports the statement made in chapter 2.2.3 that if the distances between the eigenfrequencies are below the estimated stability boundary, squeal is

possible but the disc does not necessarily squeal. It is likely that model I would squeal at this frequency with a different brake pad for example, but here it did not. However, it does have higher amplitudes in the frequency range between 350 Hz and 400 Hz presented in Fig. 4.31 and therefore squeals audibly at this frequency. Also, model II and V squeal in this range. Both discussed frequency ranges are very low and therefore the sound is not as unpleasant as it is in the high frequency range. The squeal maps for this frequency range are shown in Fig. 4.32 and demonstrate that disc II and III squeal with large vibration amplitudes at this frequency range. A high squeal level is expected from model II since it is not optimized and also from model III. Tab. 4.13 shows that this disc has a very small distance of only 3 Hz between the eigenfrequencies at around 10500 Hz. The application of the brake pad with high pressures increases the eigenfrequency to the level of the squealing frequency and therefore this small split can be considered as origin of the squeal of model III. Disc IV, however, shows the best performance with respect to squeal avoidance in all frequency ranges due to the fact that all of its eigenfrequencies are split by at least 18 Hz up to 12 kHz. Only disc V delivers comparable results, nevertheless with slightly higher maximal amplitudes as is shown in Tab. 4.14. This table gives the worst case amplitudes of the

Frequency range	Model I	Model II	Model III	Model IV	Model V
260 Hz - 320 Hz	0.95	2.22	0.61	0.85	0.72
350 Hz - 400 Hz	3.68	1.05	0.58	0.58	0.81
9 kHz - 11 kHz	0.70	2.25	2.12	0.28	0.38

Table 4.14: Comparison between the maximum amplitudes during squeal of the five prototype brake discs. Three different frequency ranges are considered. The amplitudes are given in 10^{-3} m/s.

five measured discs in the three frequency ranges and clearly demonstrates that the optimized discs IV and V have largely reduced vibration amplitudes compared to the others. The optimization was successful in these cases, still, it could be improved in the future by considering the whole frequency range

up to which squeal is possible and by using much more initial configurations in the GA (which is limited by computing power).

The maximum SPL for each disc is presented in Tab. 4.15, still, due to the inaccuracies in the measurements already mentioned in the beginning of this section, these sound pressure levels can only represent tendencies in squeal affinity. Still, the tendency that the disc models IV and V perform best is

	Model I	Model II	Model III	Model IV	Model V
SPL (dB(A))	88	99	95	84	78

Table 4.15: Comparison between the maximum sound pressure levels during squeal of the five prototype brake rotors.

clearly visible. For a final assessment of the reduction of squeal affinity by the optimization to increase the modal asymmetry, the best prototype disc is compared to the MAGURA Storm SL in the next section. Despite the fact that the SPL of model V is lower than model IV, the latter model is chosen for this purpose since it has the lowest vibration amplitudes, which represent the scientific criterion for squeal used in this thesis.

Squeal reduction assessment

In order to achieve comparable results, the squeal affinity of brake disc model IV was tested again with the MAGURA brake pads type 7.3. Compared to the type 7.1 brake pads, these pads alter the vibration amplitudes and SPL during squeal, but they do not change the squeal frequencies. The resulting squeal maps for prototype IV are shown in Figs. 4.33, a) to c) together with the squeal map of the Storm SL rotor presented in Fig. 4.33, d). Originally the latter mentioned squeal map was shown in Fig. 4.27. Here, a non-equidistant color scale has been chosen to enable a direct comparison with the squeal maps of the prototype disc. While this disc has three squealing frequencies, where the highest one dominates the audible sound, the MAGURA rotor squeals nearly monofrequently. The amplitudes of the vibrations of the optimized disc are approximately one magnitude smaller than that of the

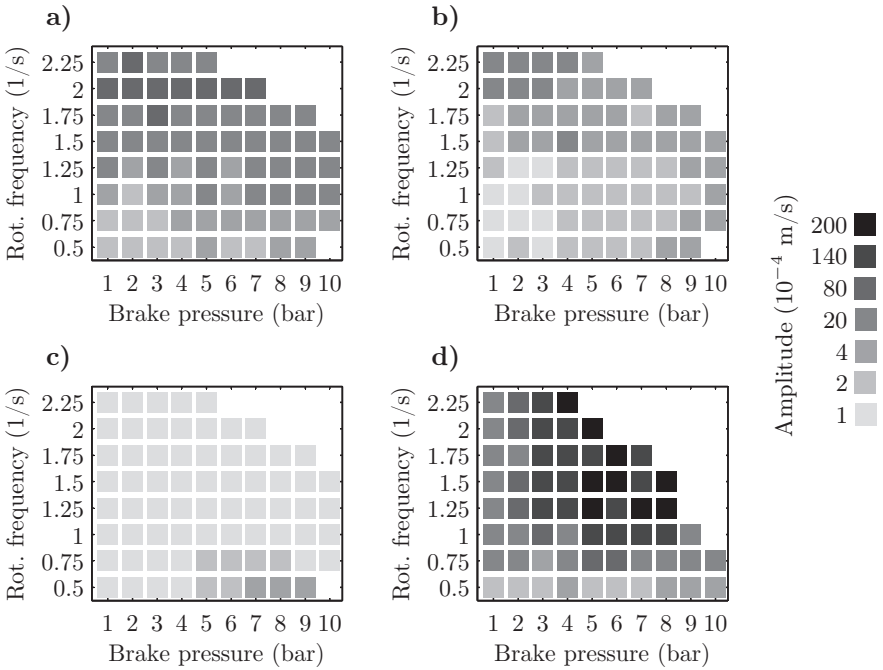

Figure 4.33: Squeal maps of prototype disc model IV and the MAGURA Storm SL. a) Model IV, frequency range 260 Hz to 320 Hz, b) model IV, frequency range 370 Hz to 420 Hz, c) model IV, frequency range 10 kHz to 11 kHz and d) Storm SL, frequency range 1010 Hz to 1050 Hz.

commercially available one. These large differences in vibration amplitudes become even more pronounced if the amplitudes of all squeal events averaged over all applied brake pressures and rotational frequencies are considered for both discs and the corresponding squeal frequencies. A comparison between the Storm SL disc and the optimized one is shown in Fig. 4.34. It is obvious that the MAGURA rotor exhibits by far the largest average vibration amplitude. The average amplitudes of the optimized disc are smaller and decrease further with increasing frequency. Also, the measured SPL of the commercially available disc is always at least 10 dB(A) higher than the SPL of the optimized rotor with a maximum of 72 dB(A). In average, the difference is

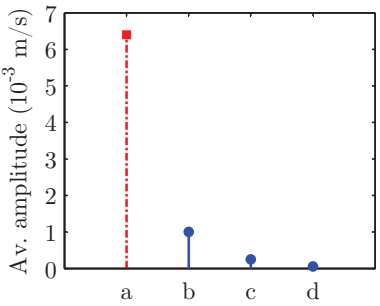

Figure 4.34: Average vibration amplitudes of the MAGURA disc (dashed, red line, square markers) and the best optimized prototype disc (solid, blue line, circular marker). Storm SL (a), prototype IV at 260 Hz to 320 Hz (b), prototype IV at 370 Hz to 420 Hz (c), prototype IV at 10 kHz to 11 kHz (d).

much higher and reaches 15 dB(A), which is without doubt highly significant. While a customer would be annoyed by the squeal of the MAGURA Storm SL if he used the disc at a mountainbike tour, the noise generated by the optimized one would be drowned in surrounding noise generated e.g. by traffic or by the wheel-ground contact.

Concluding, the optimization of bicycle brake discs was highly successful despite the fact that a grade of modal asymmetry could not be reached to avoid squeal completely. Also, the conducted tests proof that the idea of splitting all eigenfrequencies of a rotor in frictional contacts helps to avoid squeal reliably and therefore can be considered as an effective, passive and cost-efficient method to inhibit self-excited vibrations.

5 Conclusions

In this thesis a structural optimization of asymmetric brake rotors is discussed aiming for a split of the eigenfrequencies of the rotors by a certain value in a defined frequency band to avoid brake squeal. The origin of brake squeal are self-excited vibrations generated by the frictional contact between brake pads and brake disc. It is a characteristic of the squeal noise that it is usually dominated by one frequency only, which is identical or closely related to an eigenfrequency of the brake rotor. This frequency lies, at least for automotive disc brakes, in the frequency range of 1 kHz to 16 kHz. Despite being annoying for customers leading to high warranty costs, brake squeal is mainly a comfort problem for the automotive industry. Nevertheless, it can also be highly safety relevant if squealing brake discs are connected to lightweight motorcycle or bicycle rims, where the self-excited vibrations can lead to fatigue and failure of spokes.

Squeal has been studied for at least seven decades and therefore many countermeasures were proposed, reaching from purely passive measures like an increase of damping by a proper choice of disc material to active suppression of squeal. While active methods are not widely used in practice due to elaborate tuning and high costs, many passive ones like the application of damping shims cannot avoid squeal reliably under a change of temperatures, ambience conditions or the influence of wear despite the fact that they are very common. It is known from experiments that the introduction of asymmetry helps to avoid squeal. The mathematical background, however, has just been given lately. With this gained knowledge it is possible to derive goals for the design of squeal-free asymmetric brakes, which are a valuable basis for a structural optimization of the brake rotors. Examples discussed in this thesis are automotive brake discs with radial holes and cooling channels or bicycle rotors with a simplified or realistic geometry.

After a short introduction to the topic of brake squeal, its excitation mechanism and countermeasures, chapter 2 deals with the mathematical modeling and analysis of squealing brake systems. The onset of squeal is determined by an instability of the steady-sliding-state solution of the equations of motions of the system. For a full, symmetric brake disc, the stability can be determined by the real parts of eigenvalues of the linearized equations of motion, however, this is not the case for asymmetric discs. Before an analysis of asymmetric brake systems is presented, a definition of asymmetry is given, which is useful in the context of squeal avoidance. The modeling of asymmetric brake discs in frictional contact to brake pads that only cover a small sector of the disc leads necessarily to equations of motion with periodic coefficients. Therefore, stability can only be assessed with FLOQUET theory in this case. Since the terms resulting from the frictional contact are "small" compared to the elastic restoring terms, they can be treated as perturbations. This allows an analytical approximation of the stability boundary, which proves that a split of the eigenfrequencies by an amount that can be estimated in advance in a defined frequency band ensures stability and therefore helps to avoid brake squeal. This gives the basis for a structural optimization of brake discs to achieve this goal.

Since this optimization requires the usage of an efficient modeling technique and the introduction of large changes in the geometry of the disc, in chapter 3 a modeling method is presented, which can be used very effectively in this context. The basic idea of this method is that a basis structure, e.g. the brake disc, and modifications implemented to it, e.g. holes, are separately discretized using global or local shape functions with positive or negative material parameters. These discretized structures are then combined in the energy expressions and after expressing the coordinates of the modifications in the retained coordinates of the basis structure, the mass and stiffness matrices of the assembled system are obtained. These matrices determine the eigenfrequencies of the system, which are needed in the structural optimization to calculate the objective function. The proposed method is applied to two basic examples, an inhomogeneous rod and a rectangular plate with a rectangular or circular hole, where the latter is used for a detailed convergence study. The

method can readily be transferred to the modeling of brake discs, as is shown at the end of the third chapter.

Chapter 4 discusses the structural optimization of automotive brake discs and bicycle brake discs. The objective is splitting of the eigenfrequencies of the brake rotor in a certain frequency band as far as possible. The first example given is an automotive brake disc with radial holes, which was manufactured in a machine shop and tested on a brake test rig for squeal affinity. Since the optimization was successful and squeal could be prevented completely, the optimization was extended to a more realistic brake disc with cooling channels. Two types of optimization algorithms were compared with respect to their fulfillment of the objectives and their effectiveness, a mathematical programming approach and a heuristic one. Both deliver very satisfying results. Then, after a first introductory example of the optimization of a simplified bicycle brake disc, a realistic bicycle brake rotor with complex geometry was optimized. The resulting discs were manufactured followed by a modal analysis and the assessment of their squeal affinity. A comparison between the best optimized brake disc and a commercially available one proves the efficacy of the optimization and the theory behind it presented in the second chapter. The method of splitting the eigenfrequencies of the rotor is highly effective for squeal avoidance purposes and can therefore be counted as a passive, low-cost and efficient measure against brake squeal.

The manufactured bicycle rotors could directly be manufactured for a series application, however, many design aspects important for series brake discs have not been considered in the optimization. These include securing the basic stopping function of the disc even under high temperatures, wear resistance, costs, a lightweight construction and optical design aspects. Despite the fact that it was not the goal of this thesis to develop brake discs ready for series application, the findings of this thesis can directly be applied to improve the design process of series brake discs. This statement can also directly be translated to an automotive context or to brake discs used in the transport or aircraft industry. The basic physics underlying the squeal problem is the same for all types of friction-driven brake systems and therefore the remedy for squeal proposed in this thesis can be transferred directly as well.

Bibliography

[1] AbuBakar, A.R.; Ouyang, H.: Complex eigenvalue analysis and dynamic transient analysis in predicting disc brake squeal, *International Journal of Vehicle Noise and Vibration*, 2(2):143–155, 2006.

[2] Akay, A.: Acoustics of friction, *Journal of the Acoustical Society of America*, 111(4):1525–1548, 2002.

[3] Akay, A.; Giannini, O.; Massi, F.; Sestieri, A.: Disc brake squeal characterization through simplified test rigs, *Mechanical Systems and Signal Processing*, 23:2590–2607, 2009.

[4] Ali, N.; Behdinan, K.; Fawaz, Z.: Applicability and viability of a GA based finite element analysis architecture for structural design optimization, *Computers and Structures*, 81:2259–2271, 2003.

[5] Allen, M.S.; Mayes, R.L.; Bergman, E.J.: Experimental modal substructuring to couple and uncouple substructures with flexible fixtures and multi-point connections, *Journal of Sound and Vibration*, 329:4891–4906, 2010.

[6] Allgaier, R.; Gaul, L.; Keiper, W.; Willner, K.; Hoffmann, N.: A study on brake squeal using a beam-on-disc model, *Proceedings of the IMAC-XX: Conference & Exposition on Structural Dynamics - Smart Structures and Transducers*, Los Angeles, 4th - 7th February 2002.

[7] Alt, W.: *Nichtlineare Optimierung. Eine Einführung in Theorie, Verfahren und Anwendungen. (Nonlinear Optimization. An Introduction to Theory, Methods and Applications.)*, Vieweg+Teubner, Springer Fachmedien, Wiesbaden, 2011.

[8] Bae, J.C.; Wickert, J.A.: Free vibration of coupled disk-hat structures, *Journal of Sound and Vibration*, 235(1):117–132, 2000.

[9] Bajer, A.; Belsky, V.; Kung, S.W.: The influence of friction-induced damping and nonlinear effects on brake squeal analysis, *SAE Technical Paper 2004-01-2794*, 2004.

[10] Barthold, F.J.; Stander, N.; Stein, E.: Performance comparison of SAM and SQP methods for structural shape optimization, *Structural Optimization*, 11(2):102–112, 1996.

[11] Becher, M.: *Strukturoptimierung einer Fahrradbremsscheibe zur Vermeidung von Bremsenquietschen (Structural Optimization of a Bicycle Brake Disc for the Avoidance of Brake Squeal)*, Master thesis, TU Darmstadt, 2013.

[12] Becker, W.; Gross, D.: *Mechanik elastischer Körper und Strukturen (Mechanics of Elastic Bodies and Structures)*, Springer, Berlin, Heidelberg, New York, 2002.

[13] Bletzinger, K.U.; Firl, M.; Daoud, F.: Approximation of derivatives in semi-analytical structural optimization, *Computers and Structures*, 86:1404–1416, 2008.

[14] Bulman, S.; Sienz, J.; Hinton, E.: Comparisons between algorithms for structural topology optimization using a series of benchmark studies, *Computers and Structures*, 79:1203–1218, 2001.

[15] Chen, F.; Chin, A.T.; Quaglia, R.L.: *Disc Brake Squeal. Mechanism, Analysis, Evaluation and Reduction/Prevention*, SAE International, Warrendale, 2006.

[16] Chen, T.Y.; Su, J.J.: Efficiency improvement of simulated annealing in optimal structural designs, *Advances in Engineering Software*, 33:675–680, 2002.

[17] Cheng, L.; Li, Y.Y.; Yam, L.H.: Vibration analysis of annular-like plates, *Journal of Sound and Vibration*, 262(5):1153–1170, 2003.

[18] Coudeyras, N.; Sinou, J.J.; Nacivet, S.: A new treatment for predicting the self-excited vibrations of nonlinear systems with frictional interfaces: The constrained harmonic balance method, with application to disc brake squeal, *Journal of Sound and Vibration*, 319:1175–1199, 2009.

[19] Cuilliere, J.C.; Bournival, S.; Francois, V.: A mesh-geometry-based solution to mixed-dimensional coupling, *Computer-Aided Design*, 42(6):509–522, 2010.

[20] Cunefare, K.A.; Graf, A.J.: Experimental active control of automotive disc brake rotor squeal using dither, *Journal of Sound and Vibration*, 250(4):579–590, 2002.

[21] Dai, Y.; Lim, T.C.: Suppression of brake squeal noise applying finite element brake and pad enhanced by spectral-based assurance criteria, *Journal of Applied Acoustics*, 69:196–214, 2008.

[22] Day, J.: Disc brake rotor, US Patent No. 3298476, 1967.

[23] de Boer, A.; van Zuijlen, A.H.; Bijl, H.: Review of coupling methods for non-matching meshes, *Computer Methods in Applied Mechanics and Engineering*, 196(8):1515–1525, 2007.

[24] Dessouki, O.; Drake, G.; Lowe, B.; Chang, W.K.: Disc Brake Squeal: Diagnosis and Prevention, *SAE Technical Paper 2003-01-1618*, 2003.

[25] Dessouki, O.; Lowe, B.D.; Riefe, M.T.; Doescher, M.T.; Sachdev, A.K.; Verbrugge, M.W.; Schroth, J.G.; Hanna, M.D.: Coulomb friction damped disc brake rotors, US Patent No. 7975750, 2011.

[26] Dunlap, K.B.; Riehle, M.A.; Longhouse, R.E.: An investigative overview of automotive disc brake noise, *SAE Technical Paper 1999-01-0142*, 1999.

[27] Fieldhouse, J.D.: Professional overview on squealing phenomena and models, *Eurobrake 2012*, Dresden, Germany, 16th - 18th April 2012.

[28] Fieldhouse, J.D.; Steel, W.P.; Talbot, J.C.; Siddiqui, M.A.: Rotor asymmetry used to reduce disc brake noise, *SAE Technical Paper 2004-01-2797*, 2004.

[29] Fourie, P.C.; Groenwold, A.A.: The particle swarm optimization algorithm in size and shape optimization, *Structural and Multidisciplinary Optimization*, 23(4):259–267, 2002.

[30] Fritz, G.; Sinou, J.J.; Duffal, J.M.; Jezequel, L.: Effects of damping on brake squeal coalescence patterns - application on a finite element model, *Mechanics Research Communications*, 34(2):181–190, 2007.

[31] Gandomi, A.H.; Yang, X.S.; Alavi, A.H.: Mixed variable structural optimization using firefly algorithm, *Computers and Structures*, 89:2325–2336, 2011.

[32] Graf, M.; Ostermeyer, G.P.: Instabilities in the sliding of continua with surface inertias: An initiation mechanism for brake noise, *Journal of Sound and Vibration*, 330:5269–5279, 2011.

[33] Grandhi, R.: Structural optimization with frequency constraints - a review, *AIAA Journal*, 31(12):2296–2303, 1993.

[34] Hagedorn, P.: *Non-linear Oscillations*, Oxford University Press, Oxford, 1988.

[35] Hagedorn, P.; DasGupta, A.: *Vibrations and Waves in Continuous Mechanical Systems*, John Wiley & Sons, Chichester, Hoboken, San Francisco, Weinheim, Milton, Singapore, Mississauga, 2007.

[36] Hagedorn, P.; Hochlenert, D.: *Technische Schwingungslehre. Schwingungen linearer diskreter mechanischer Systeme. (Technical vibrations analysis. Vibrations of linear discrete mechanical systems)*, Wissenschaftlicher Verlag Harri Deutsch, Frankfurt am Main, 2012.

[37] Harzheim, L.: *Strukturoptimierung. Grundlagen und Anwendungen (Sructural Optimization. Basics and Applications)*, Wissenschaftlicher Verlag Harri Deutsch, Frankfurt am Main, 2008.

[38] Hassan, M.Z.; Brooks, P.C.; Barton, D.C.: The evaluation of disc brake squeal propensity through a fully coupled transient thermomechanical model, *Proceedings of the Institution of Mechanical Engineers, Part D: Journal of Automobile Engineering*, 227(3):361–375, 2013.

[39] Herrmann, G.: *Dynamics and Stability of Mechanical Systems with Follower Forces*, National Aeronautics and Space Administration, Washington D.C., 1971.

[40] Hochlenert, D.: *Berichte aus dem Maschinenbau, Selbsterregte Schwingungen in Scheibenbremsen: Mathematische Modellbildung und aktive Unterdrückung von Bremsenquietschen (Reports from Mechanical Engineering, Self-excited Vibrations in Disc Brakes: Mathematical Modelling and Active Suppression of Brake Squeal)*, Shaker, Aachen, 2006.

[41] Hochlenert, D.: Nonlinear stability analysis of a disk brake model, *Nonlinear Dynamics*, 58(1-2):63–73, 2009.

[42] Hochlenert, D.; Hagedorn, P.: Control of disc brake squeal - modelling and experiments, *Structural Control and Health Monitoring*, 13:260–276, 2006.

[43] Hochlenert, D.; Spelsberg-Korspeter, G.; Hagedorn, P.: Friction induced vibrations in moving continua and their application to brake squeal, *Transactions of the ASME, Journal of Applied Mechanics*, 75:542–549, 2007.

[44] Hochlenert, D.; Spelsberg-Korspeter, G.; Hagedorn, P.: A note on safety-relevant vibrations induced by brake squeal, *Journal of Sound and Vibration*, 329:3867–3872, 2010.

[45] Hochlenert, D.; von Wagner, U.: Passive and active techniques to handle brake squeal with piezoelectric actuators, *Proceedings of Braking 2009*, Institution of Mechanical Engineers, York, 2009.

[46] Hou, J.; Sun, G.; Guo, X.; Zhang, J.: Suppression of brake squeal noise applying viscoelastic damping insulator, *International Joint Conference on Computational Sciences and Optimization*, Sanya, Hainan, China, April 24-26, 2009.

[47] Hsu, Y.L.: A review of structural shape optimization, *Computers in Industry*, 26:3–13, 1994.

[48] Ibrahim, R.: Friction-induced vibration, chatter, squeal, and chaos, Part II: Dynamics and modeling, *Applied Mechanics Reviews*, 47(7):227–253, 1994.

[49] Ibrahim, R.: Friction-induced vibration, chatter, squeal, and chaos, Part I: Mechanics of contact and friction, *Applied Mechanics Reviews*, 47(7):209–226, 1994.

[50] Ilanko, S.: Existence of natural frequencies of systems with artificial restraints and their convergence in asymptotic modelling, *Journal of Sound and Vibration*, 255(5):883–898, 2002.

[51] Ilanko, S.: The use of asymptotic modelling in vibration and stability analysis of structures, *Journal of Sound and Vibration*, 263(5):1047–1054, 2003.

[52] Ilanko, S.: Introducing the use of positive and negative inertial functions in asymptotic modelling, *Proceedings of the Royal Society A*, 461(2060):2545–2562, 2005.

[53] Ilanko, S.: Wittrick-Williams algorithm proof of bracketing and convergence theorems for eigenvalues of constrained structures with positive

and negative penalty parameters, *International Journal for Numerical Methods in Engineering*, 75(1):83–102, 2008.

[54] Ilanko, S.; Dickinson, S.M.: Asymptotic modelling of rigid boundaries and connections in the Rayleigh-Ritz method, *Journal of Sound and Vibration*, 219(2):370–378, 1999.

[55] Irretier, H.: *Grundlagen der Schwingungstechnik 2. Systeme mit mehreren Freiheitgraden, Kontinuierliche Systeme. (Basic Principles of the Analysis of Vibrations. Systems with many Degrees of Freedom, Continuous Systems.)*, Vieweg, Braunschweig, Wiesbaden, 2001.

[56] Jansen, P.W.; Perez, R.E.: Constrained structural design optimization via a parallel augmented Lagrangian particle swarm optimization approach, *Computers and Structures*, 89:1352–1366, 2011.

[57] Jüngst, M.: *Experimentelle Modalanalyse eines Bremsenprüfstands und Parameteridentifikation des zugehörigen FE Modells (Experimental Modal Analysis of a Brake Test Rig and Parameter Identification of the Corresponding FE Model)*, Bachelor thesis, TU Darmstadt, 2011.

[58] Kang, J.: Squeal analysis of gyroscopic disc brake system based on finite element method, *International Journal of Mechanical Sciences*, 51:284–294, 2009.

[59] Kessler, P.; O'Reilly, O.M.; Raphael, A.L.; Zworski, M.: On dissipation-induced destabilization and brake squeal: A perspective using structured pseudospectra, *Journal of Sound and Vibration*, 308:1–11, 2007.

[60] Kinkaid, N.M.; O'Reilly, O.M.; Papadopoulos, P.: Automotive disc brake squeal, *Journal of Sound and Vibration*, 267:105–166, 2003.

[61] Kubota, Y.; Okubo, K.; Fujii, T.: Reduction of squeal on laminated brake disc fastened with distributed contact pressure, *Proceedings of the 5th WSEAS International Conference on Engineering Mechanics, Structures, Engineering Geology*, Cambridge, UK, February 25-27, 2012.

[62] Kwak, B.M.: A review on shape optimal design and sensitivity analysis, *JSCE Journal Structure Engineering/Earthquake Engineering*, 10(4):159–174, 1994.

[63] Kwak, M.K.; Han, S.: Free vibration analysis of rectangular plate with a hole by means of independent coordinate coupling method, *Journal of Sound and Vibration*, 306(1-2):12–30, 2007.

[64] Kwon, Y.D.; Kwon, S.B.; Jin, S.B.; Kim, J.Y.: Convergence enhanced genetic algorithm with successive zooming method for solving continuous optimization problems, *Computers and Structures*, 81:1715–1725, 2003.

[65] Lee, K.S.; Geem, Z.W.: A new structural optimization method based on the harmony search algorithm, *Computers and Structures*, 82:781–798, 2004.

[66] Lee, W.M.; Chen, J.T.; Lee, Y.T.: Free vibration analysis of circular plates with multiple circular holes using indirect BIEMs, *Journal of Sound and Vibration*, 304(3-5):811–830, 2007.

[67] Lin, S.C.; Guan, C.C.; AbuBakar, A.R.; Jamaluddin, M.R.; Harujan, W.M.M.W.; Ghani, B.A.: Disc brake squeal suppression through chamfered and slotted pad, *International Journal of Vehicle Structures & Systems*, 3(1):28–35, 2011.

[68] Link, M.: *Finite Elemente in der Statik und Dynamik (Finite Elements in Statics and Dynamics)*, B. G. Teubner, Stuttgart, Leipzig, Wiesbaden, 2002.

[69] Liu, F.L.; Liew, K.M.: Differential quadrature element method: a new approach for free vibration analysis of polar Mindlin plates having discontinuities, *Computer Methods in Applied Mechanics and Engineering*, 179(3-4):407–423, 1999.

[70] Lorang, X.; Foy-Margiocchi, F.; Nguyen, Q.S.; Gautier, P.E.: TGV disc brake squeal, *Journal of Sound and Vibration*, 293:735–746, 2006.

[71] Luo, Z.; Tong, L.; Kang, Z.: A level set method for structural shape and topology optimization using radial basis functions, *Computers and Structures*, 87:425–434, 2009.

[72] Martini, K.P.E.: Harmony search method for multimodal size, shape, and topology optimization of structural frameworks, *Journal of Structural Engineering*, 137(11):1332–1339, 2011.

[73] Massi, F.; Baillet, L.; Giannini, O.; Sestieri, A.: Brake squeal: Linear and nonlinear numerical approaches, *Mechanical Systems and Signal Processing*, 21:2374–2393, 2007.

[74] Massi, F.; Giannini, O.; Baillet, L.: Brake squeal as dynamic instability: An experimental investigation, *Journal of the Acoustical Society of America*, 120(3):1388–1398, 2006.

[75] Mayes, R.L.; Ross, M.R.: Advancements in hybrid dynamic models combining experimental and finite element substructures, *Mechanical Systems and Signal Processing*, 31:56–66, 2012.

[76] Miguel, L.F.F.; Miguel, L.F.F.: Shape and size optimization of truss structures considering dynamic constraints through modern metaheuristic algorithms, *Expert Systems with Applications*, 39(10):9458–9467, 2012.

[77] Mortazavi, V.; Wang, C.; Nosonovsky, M.: Stability of frictional sliding with the coefficient of friction dependend on the temperature, *Journal of Tribology*, 134:041601–1 – 041601–7, 2012.

[78] Murray, S.L.: Brake rotor with vibration harmonic suppression, and method of manufacture, US Patent No. 4523666, 1985.

[79] Nakae, T.; Ryu, T.; Sueoka, A.; Nakano, Y.; Inoue, T.: Squeal and chatter phenomena generated in a mountain bike disc brake, *Journal of Sound and Vibration*, 330(10):2138–2149, 2011.

[80] Neubauer, M.; Han, X.; Wallaschek, J.: On the maximum damping performance of piezoeletric switching techniques, *Journal of Intelligent Material Systems and Structures*, 24(6):717–728, 2013.

[81] Neubauer, M.; Oleskiewicz: Brake squeal control with shunted piezoceramics - efficient modelling and experiments, *Proceedings of the Institution of Mechanical Engineers, Part D: Journal of Automobile Engineering*, 222:1141–1151, 2008.

[82] Neubauer, M.; Wallaschek, J.: Vibration damping with shunted piezoceramics: fundamentals and technical applications, *Mechanical Systems and Signal Processing*, doi:10.1016/j.ymssp.2011.05.011, 2011.

[83] Nishiwaki, M.: Generalized theory of brake noise, *Proceedings of the Institution of Mechanical Engineers, Part D: Journal of Automobile Engineering*, 207:195–202, 1993.

[84] Nishiwaki, M.; Harada, H.; Okamura, H.; Ikeuchi, T.: Study on disc brake squeal, *SAE Technical Paper 890864*, 1989.

[85] Oberst, S.; Lai, J.C.S.; Marburg, S.: Guidelines for numerical vibration and acoustic analysis of disc brake squeal using simple models of brake systems, *Journal of Sound and Vibration*, 332(9):2284–2299, 2013.

[86] Okamura, H.; Yamada, M.: Rotary disc for disc brake assembly, US Patent No. 4867284, 1989.

[87] Ouyang, H.: Prediction and assignment of latent roots of damped asymmetric systems by structural modifications, *Mechanical Systems and Signal Processing*, 23:1920–1930, 2009.

[88] Ouyang, H.; Cao, Q.; Mottershead, J.E.; Treyde, T.: Vibration and squeal of a disc brake: Modelling and experimental results, *Proceedings of the Institution of Mechanical Engineers, Part D: Journal of Automobile Engineering*, 217:867–875, 2003.

[89] Ouyang, H.; Mottershead, J.E.: Dynamic instability of an elastic disk under the action of a rotating friction couple, *Transactions of the ASME, Journal of Applied Mechanics*, 71:753–758, 2004.

[90] Ouyang, H.; Mottershead, J.E.; Cartmell, M.P.; Brookfield, D.J.: Friction-induced vibration of an elastic slider on a vibrating disc, *International Journal of Mechanical Sciences*, 41:325–336, 1999.

[91] Ouyang, H.; Mottershead, J.E.; Cartmell, M.P.; Friswell, M.I.: Friction-induced parametric resonances in discs: effect of a negative friction-velocity relationship, *Journal of Sound and Vibration*, 209(2):251–264, 1998.

[92] Ouyang, H.; Nack, W.; Yuan, Y.; Chen, F.: Numerical analysis of automotive disc brake squeal: a review, *International Journal of Vehicle Noise and Vibration*, 1(3-4):207–231, 2005.

[93] Papadrakakis, M.; Tsompanakis, Y.; Lagaros, N.D.: Structural shape optimization using evolution strategies, *Engineering Optimization*, 31(4):515–540, 1999.

[94] Papinniemi, A.; Lai, J.C.S.; Zhao, J.; Loader, L.: Brake squeal: a literature review, *Journal of Applied Acoustics*, 63:391–400, 2002.

[95] Saitou, K.; Izui, K.; Nishiwaki, S.; Papalambros, P.: A survey of structural optimization in mechanical product development, *Transactions of the ASME, Journal of Computing and Information Science in Engineering*, 5:214–226, 2005.

[96] Schumacher, A.: *Optimierung mechanischer Strukturen. Grundlagen und industrielle Anwendungen. (Optimization of Mechanical Structures. Basics and Industrial Applications.)*, Springer, Berlin, Heidelberg, New York, 2005.

[97] Sedaghati, R.: Benchmark case studies in structural design optimization using the force method, *International Journal of Solids and Structures*, 42:5848–5871, 2005.

[98] Serre, J.: *Linear Representations of Finite Groups*, volume 72, Springer, 1977.

[99] Seyranian, A.P.; Mailybaev, A.A.: *Multiparameter Stability Theory with Mechanical Applications*, World Scientific Publishing, New Jersey, London, Singapore, Shanghai, Hong Kong, Taipei, Bangalore, 2003.

[100] Shin, K.; Brennan, M.J.; Oh, J.E.; Harris, C.J.: Analysis of disc brake noise using a two-degree-of-freedom model, *Journal of Sound and Vibration*, 254(5):837–848, 2002.

[101] Silva, C.A.C.; Bittencourt, M.L.: Velocity fields using NURBS with distortion control for structural shape optimization, *Structural and Multidisciplinary Optimization*, 33(2):147–159, 2007.

[102] Sinou, J.J.: Transient non-linear dynamic analysis of automotive disc brake squeal - On the need to consider both stability and non-linear analysis, *Mechanics Research Communications*, 37:96–105, 2010.

[103] Sinou, J.J.; Dereure, O.; Mazet, G.B.; Thouverez, F.; Jezequel, L.: Friction-induced vibration for an aircraft brake system - part 1: Experimental approach and stability analysis, *International Journal of Mechanical Sciences*, 48:536–554, 2006.

[104] Snyman, J.A.; Stander, N.: New successive approximation method for optimum structural design, *AIAA Journal*, 32(6):1310–1315, 1994.

[105] Soh, H.J.; Yoo, J.H.: Optimal shape design of a brake calliper for squeal noise reduction considering system instability, *Proceedings of the Institution of Mechanical Engineers, Part D: Journal of Automobile Engineering*, 224:909–925, 2010.

[106] Spelsberg-Korspeter, G.: Breaking of symmetries for stabilization of rotating continua in frictional contact, *Journal of Sound and Vibration*, 322:798–807, 2009.

[107] Spelsberg-Korspeter, G.: Structural optimization for the avoidance of self-excited vibrations based on analytical models, *Journal of Sound and Vibration*, 329(23):4829–4840, 2010.

[108] Spelsberg-Korspeter, G.: Eigenvalue optimization against brake squeal: Symmetry, mathematical background and experiments, *Journal of Sound and Vibration*, 331(19):4259–4268, 2012.

[109] Spelsberg-Korspeter, G.: *Robust Structural Design against Self-excited Vibrations*, SpringerBriefs in applied sciences and technology, Springer, Heidelberg, New York, Dordrecht, London, 2013.

[110] Spelsberg-Korspeter, G.; Hagedorn, P.: Complex eigenvalue analysis and brake squeal: Traps, shortcomings and their removal, *SAE Technical Paper 2012-01-1814*, 2012.

[111] Spelsberg-Korspeter, G.; Hagedorn, P.; Hochlenert, D.: Non-linear investigation of an asymmetric disk brake model, *Proceedings of the Institution of Mechanical Engineers, Part C: Journal of Mechanical Engineering Science*, 225(10):2325–2332, 2011.

[112] Spelsberg-Korspeter, G.; Hochlenert, D.; Kirillov, O.; Hagedorn, P.: In- and out-of-plane vibrations of a rotating plate with frictional contact: Investigations on squeal phenomena, *Transactions of the ASME, Journal of Applied Mechanics*, 76:041006–1 – 041006–15, 2009.

[113] Spelsberg-Korspeter, G.; Schönecker, M.; Hagedorn, P.: On the relation between rotor asymmetry and brake squeal, *SAE Technical Paper 2010-01-1692*, 2010.

[114] Spelsberg-Korspeter, G.; Wagner, A.: Discretization of structures using a negative stiffness approach in the context of structural optimization, *Proceedings of the 8th International Symposium on Vibrations of Continuous Systems*, Whistler, Kanada, 17th - 23rd July 2011.

[115] Stiefel, E.; Fassler, A.: *Gruppentheoretische Methoden und ihre Anwendung (Group-Theoretical Methods and their Application)*, BG Teubner, 1979.

[116] Suga, T.; Katagiri, M.: Disk brake rotor exhibiting different modes of vibration on opposite sides during braking, US Patent No. 5735366, 1998.

[117] Takahashi, S.: Vibration of rectangular plates with circular holes, *Bulletin of JSME*, 1(4):380–385, 1958.

[118] Thanedar, P.B.; Vanderplaats, G.N.: Survey of discrete variable optimization for structural design, *Journal of Structural Engineering*, 121:301–306, 1995.

[119] Tuchinda, A.; Hoffmann, N.P.; Ewins, D.J.; Keiper, W.: Mode lock-in characteristics and instability study of the pin-on-disc system, *Proceedings of the IMAC XIX - 19th International Modal Analysis Conference - Future Directions in Structural Dynamics*, 2001.

[120] van Keulen, F.; Haftka, R.T.; Kim, N.H.: Review of options for structural design sensitivity analysis. Part 1: Linear systems, *Computer Methods in Applied Mechanics and Engineering*, 194:3213–3243, 2005.

[121] Vomstein, T.: *Berichte aus dem Maschinenbau, Strukturmodifikation moderner Bremsscheiben: Mathematische Modellierung und passive Unterdrückung von Bremsenquietschen (Structural Modification of modern Brake Discs: Mathematical Modeling and passive Suppression of Brake Squeal)*, Shaker, Aachen, 2008.

[122] von Wagner, U.; Hochlenert, D.; Hagedorn, P.: Minimal models for disk brake squeal, *Journal of Sound and Vibration*, 302:527–539, 2007.

[123] von Wagner, U.; Hochlenert, D.; Jearsiripongkul, T.; Hagedorn, P.: Active control of brake squeal via 'smart pads', *SAE Technical Paper 2004-01-2773*, 2004.

[124] von Wagner, U.; Spelsberg-Korspeter, G.: Minimal models for squealing of railway block brakes, *Archive of Applied Mechanics*, 81:503–511, 2010.

[125] Wagner, A.; Schönecker, M.; Spelsberg-Korspeter, G.; Hagedorn, P.: On criteria for the robust design of squeal free brakes, *SAE Technical Paper 2012-01-1816*, 2012.

[126] Wagner, A.; Spelsberg-Korspeter, G.: An efficient approach for the assembly of mass and stiffness matrices of structures with modifications, *Journal of Sound and Vibration*, 332(18):4296–4307, 2013.

[127] Wang, X.; Wang, M.Y.; Guo, D.: Structural shape and topology optimization in a level-set-based framework of region representation, *Structural and Multidisciplinary Optimization*, 27(1-2):1–19, 2004.

[128] Wei, P.; Wang, M.Y.; Xing, X.: A study on X-FEM in continuum structural optimization using a level set model, *Computer-Aided Design*, 42:708–719, 2010.

[129] Xia, Q.; Shi, T.; Wang, M.Y.: A level set based shape and topology optimization method for maximizing the simple or repeated first eigenvalue of structure vibration, *Structural and Multidisciplinary Optimization*, 43(4):473–485, 2011.

[130] Xie, Y.M.; Steven, G.P.: Evolutionary structural optimization for dynamic problems, *Computers & Structures*, 58(6):1067–1073, 1996.

[131] Yamasaki, S.; Nishiwaki, S.; Izui, K.; Yoshimura, M.: Structural optimization of mechanical structures targeting vibration characteristics based on the level set method, *Journal of Environment and Engineering*, 5(1):60–71, 2010.

[132] Yildiz, A.R.: A new hybrid particle swarm optimization approach for structural design optimization in the automotive industry, *Proceedings of the Institution of Mechanical Engineers, Part D: Journal of Automobile Engineering*, 226(10):1340–1351, 2012.

[133] Yu, R.C.; Mote, C.D.: Vibration and parametric excitation in asymmetric circular plates under moving loads, *Journal of Sound and Vibration*, 119(3):409–427, 1987.

[134] Zainudin, M.A.; AbuBakar, A.R.: Preventing disc brake squeal using a thin plate shim, *International Journal of Vehicle Structures & Systems*, 4(1):23–27, 2012.

[135] Zhang, S.; Belegundu, A.D.: Mesh distortion control in shape optimization, *AIAA Journal*, 31(7):1360–1362, 1993.

[136] Zhao, C.B.; Steven, G.P.; Xie, Y.M.: Evolutionary optimization of maximizing the difference between two natural frequencies, *Structural Optimization*, 13:148–154, 1997.

[137] Zhou, Z.H.; Wong, K.W.; Xu, X.S.; Leung, A.Y.T.: Natural vibration of circular and annular thin plates by Hamiltonian approach, *Journal of Sound and Vibration*, 330(5):1005–1017, 2011.

Bisher sind in dieser Reihe erschienen

Band 1
Zur mikrorissinduzierten Schädigung spröder Materialien
B. Lauterbach, Dissertation 2001, ISBN 3-935868-01-4

Band 2
3D-Simulation der Mikrostrukturentwicklung in Zwei-Phasen-Materialien
R. Müller, Dissertation 2001, ISBN 3-935868-02-2

Band 3
Zur numerischen Simulation von Morphologieänderungen in mikroheterogenen Materialien
S. Kolling, Dissertation 2001, ISBN 3-935868-03-0

Band 4
Theoretische und numerische Untersuchung von Versagensmechanismen in Metall-Keramik-Verbundwerkstoffen
T. Emmel, Dissertation 2002, ISBN 3-935868-04-9

Band 5
On microcrack dominated problems in dynamics and statics of brittle fracture: a numerical study by boundary element techniques
S. Rafiee, Dissertation 2002, ISBN 3-935868-05-7

Band 6
Kontinuumsmechanik anisotroper Festkörper und Fluide
H. Ehrentraut, Habilitationsschrift 2002, ISBN 3-935868-06-5

Band 7
Plane unsteady inviscid incompressible hydrodynamics of a thin elastic profile
N. Blinkova, Dissertation 2002, ISBN 3-935868-07-3

Band 8
Anmerkungen zur Simulation von entfestigendem Materialverhalten
H. Baaser, Habilitationsschrift 2004, ISBN 3-935868-08-1

Band 9
Orts- und zeitadaptive DAE-Methoden zur Beschreibung elastisch-plastischen Materialverhaltens innerhalb der FEM
S. Eckert, Dissertation 2005, ISBN 3-935868-09-X

Band 10
Simulations of the Flow of the Ross Ice Shelf, Antarctica: Parameter Sensitivity Tests and Temperature-Dependent Rate Factor
A. Humbert, Dissertation 2005, ISBN 3-935868-10-3

Band 11
A Thermo-mechanical Continuum Theory with Internal Length of Cohesionless Granular Materials
Chung Fang, Dissertation 2006, ISBN 3-935868-11-1

Band 12
Modeling Dry Granular Avalanches past Different Obstructions: Numerical Simulation and Laboratory Analyses
Chiou Min-Ching, Dissertation 2006, ISBN 3-935868-12-X

Band 13
Configurational forces in defect mechanics and in computational methods
R. Müller, Habilitationsschrift 2005, ISBN 3-935868-13-8

Band 14
Hyperelastic dynamics in physical and material space
S. Kolling, Habilitationsschrift 2007, ISBN 978-3-935868-14-3

Band 15
Phenomenological modeling of ferroelectric material behavior
V. Mehling, Dissertation 2007, ISBN 978-3-935868-15-0

Band 16
Ein mischungsbasiertes Materialmodell zum Knochenumbau
R.-R. Kühn, Dissertation 2006, ISBN 978-3-935868-16-7

Band 17
Einige Erweiterungen der Rand-Finite-Elemente-Methode und deren Anwendung auf Randeffekte in ebenen Laminaten
J. Artel, Dissertation 2007, ISBN 978-3-935868-17-4

Band 18
Spannungskonzentrations-Effekte an Verstärkungspflaster-Ecken
H. Wigger, Dissertation 2008, ISBN 978-3-935868-18-1

Band 19
Rotationseffekte in der Kristallplastizität
C. Bröse, Dissertation 2007, ISBN 978-3-935868-19-8

Band 20
Finite-Element-Modelle zur Simulation von Delaminationen dünner Filme auf Substraten
V. D. Pham, Dissertation 2010, ISBN 978-3-935868-20-4

Band 21
Asymptotische Nahfeldanalysen ebener Multi-Materialverbindungsstellen mit der Methode komplexer Potentiale
C. Sator, Dissertation 2010, ISBN 978-3-935868-21-1

Band 22
Modellierung spröder Rissbildung an Spannungskonzentrationen mit der Bruchmechanik finiter Risse
J. Hebel, Dissertation 2010, ISBN 978-3-935868-22-8

Band 23
Some Contributions to the Homogenization of Macroscopically Isotropic Composites
V. Salit, Dissertation 2011, ISBN 978-3-935868-23-5

Band 24
Asymptotic Analysis of the Load Transfer on Double-Lap Bolted Joints
J. Kratochvíl, Dissertation 2012, ISBN 978-3-935868-24-2

Band 25
Spannungssingularitätsordnungen in linear-elastischen und piezoelektrischen Multimaterialkonfigurationen mit der Rand-Finite-Elemente-Methode
W. Mayland, Dissertation 2012, ISBN 978-3-935868-25-9

Band 26
Plastizität und Skaleneffekte sowie Deformations- und Versagensmodellierung dünner metallischer Schichten bei Nanoindentation
A. Trondl, Dissertation 2012, ISBN 978-3-935868-26-6

Band 27
Theoretical modeling and parallel programming of a nonlinear composite finite shell element based on a mixed global-local variational principle
M. Schürg, Dissertation 2012, ISBN 978-3-935868-27-3

Band 28
Strukturmechanische Modellierung und Analyse des Tragverhaltens von dünnwandigen hochbelasteten Composite-Biege- und Querkraftträgern
A. M. Kroker, Dissertation 2012, ISBN 978-3-935868-28-0

Band 29
Über die Entstehung von Raum und Zeit
P. Altstadt, Forschungsbereicht 2013, ISBN 978-3-935868-29-7

Band 30
Der Laminatrandeffekt und seine Analyse, insbesondere mit der Rand-Finite-Elemente-Methode
J. Lindemann, Dissertation 2013, ISBN 978-3-935868-30-3

Brake squeal is a high-pitched noise originating from self-excited vibrations caused by the frictional contact between brake pads and brake disc. It is known from experiments and has also been proved mathematically that splitting the eigenfrequencies of the brake rotor has a stabilizing effect and avoids brake squeal. In this work, this knowledge is used to derive design goals for asymmetric, squeal-free discs. It is necessary to split all eigenfrequencies of the brake disc in a pre-definable frequency band to guarantee stability, inhibit the onset of self-excited vibrations and thus avoid squeal completely. In order to achieve this goal, a structural optimization of automotive as well as bicycle brake discs is conducted. Optimized automotive and bicycle brake discs have been manufactured and tested to assess their squeal affinity, and it is shown that the optimized discs have a greatly improved squeal behavior. This demonstrates that splitting eigenfrequencies of the brake rotor is a passive, low-cost and effective squeal countermeasure applicable to a variety of brake systems.

ISBN 978-3-935868-31-0